

A11102 487363

NAT'L INST OF STANDARDS & TECH R.I.C.



A11102487363

/Research for electric energy systems :
QC100 .U56 NO.86-3316 V1986 C.2 NBS-PUB-

Research for Electric Energy Systems - An Annual Report

NBS

PUBLICATIONS

R. E. Hebner, Editor

U.S. DEPARTMENT OF COMMERCE
National Bureau of Standards
Center for Electronics and Electrical Engineering
Gaithersburg, MD 20899

December 1985

Issued March 1986

Prepared for:

Department of Energy

QC **of Electric Energy Systems**
100 **pendence Avenue, SW**
.U56 **on, DC 20585**

86-3316

1986

C. 2

02
100
456
86-3316
1986
22

NBSIR 86-3316

**RESEARCH FOR ELECTRIC ENERGY
SYSTEMS - AN ANNUAL REPORT**

R. E. Hebner, Editor

U.S. DEPARTMENT OF COMMERCE
National Bureau of Standards
Center for Electronics and Electrical Engineering
Gaithersburg, MD 20899

December 1985

Issued March 1986

Prepared for:
Department of Energy
Division of Electric Energy Systems
1000 Independence Avenue, SW
Washington, DC 20585



U.S. DEPARTMENT OF COMMERCE, Malcolm Baldrige, *Secretary*
NATIONAL BUREAU OF STANDARDS, Ernest Ambler, *Director*

Foreword

This report summarizes the progress of five technical investigations during FY 85. Although reasonable efforts have been made to ensure the reliability of the data presented, it must be emphasized that this is an interim progress report so that further experimentation and analysis may be performed before the conclusions from any of these investigations are formally published. It is therefore possible that some of the observations presented in this report will be modified, expanded, or clarified by our subsequent research.

LIST OF FIGURES

	Page
Figure 1. AMFM-1 frequency response as function of signal amplitude. Frequencies at which clipping occurs (see text) for the various scales are indicated.	4
Figure 2. Oscilloscope display of current waveform superimposed on waveform of output signal from AMFM-1. Amplitudes of two waveforms have been made equal for purposes of comparison.	6
Figure 3. Spectrum analyzer display indicating frequency components of the waveforms shown in figure 2. The traces for the two waveforms are superimposed.	6
Figure 4. Schematic view of NBS parallel plate apparatus. The arrangement shown is appropriate for generating an electric field with positive space charge. The top and bottom plates of the parallel plate system are located in the planes $z = 0$ and $z = d$. The corona wires are oriented parallel to one another and are perpendicular to the plane of the figure.	8
Figure 5. Normalized ion density profiles for two current densities, $1 \times 10^{-6} \text{ A/m}^2$ and $0.1 \times 10^{-6} \text{ A/m}^2$. The calculated results assume that $V_t = 2650 \text{ V}$, $K = 1.3 \times 10^{-4} \text{ m}^2/\text{Vs}$, and $d = 0.17 \text{ m}$	10
Figure 6. Schematic view showing perturbations of electric field and charge density due to an aperture in the ground plane and air motion do not extend across the parallel plate spacing.	10
Figure 7. Measurements of space potential perturbation due to 5 cm x 5 cm aperture in ground plane as a function of height above ground plane.	13
Figure 8. Ion trajectories for air speed of 1 m/s in plane of aperture. The solid curves show influence of 15 kV/m electric field. Dashed curves are for no electric field. The time-of-flight for all trajectories is 50 ms. The volume occupied by the ions that enter aperture when $E \neq 0, V'$, exceeds volume of air, V , which enters in the same time. Inset shows effect of mobility value on trajectory near aperture.	18
Figure 9. Ion trajectories for air speed in plane of aperture of 6 m/s. The solid curves show influence of 15 kV/m electric field. Dashed	

5.6	Liquid Breakdown Phenomena.	49
5.7	Partial Discharge Measurements and Their Photography.	52
5.8	Summary	53
6.	NANOSECOND BREAKDOWN IN POWER SYSTEM DIELECTRICS	
	Subtask No. 05.	53
6.1	Introduction.	53
6.2	Test Facilities	54
6.3	Mathematical Methods.	55
6.4	Electro-Optic Methods	60
6.5	Streamer Growth in Dielectric Fluids under Fast Risetime Pulses .	62
6.6	Summary	66
7.	REFERENCES.	71

TABLE OF CONTENTS

	Page
Foreword.	iii
LIST OF FIGURES	vi
LIST OF TABLES.	x
Abstract.	1
1. INTRODUCTION.	2
2. AC ELECTRIC AND MAGNETIC FIELDS	
Subtask No. 01.	2
2.1 Introduction.	2
2.2 Ambient Magnetic Field Meter.	2
2.3 Summary	5
3. DC FIELDS AND ION MEASUREMENTS	
Subtask No. 02.	5
3.1 Introduction.	5
3.2 NBS Parallel Plate Apparatus and Approach	7
3.3 Space Potential Perturbation Measurements	12
3.4 Discussion.	14
3.5 Ion Trajectories and Losses	15
3.6 Summary	19
4. GASEOUS DIELECTRICS RESEARCH	
Subtask No. 03.	20
4.1 Introduction.	20
4.2 Influence of Trace Amounts of Water Vapor on Electron Avalanche Growth in SF ₆	20
4.3 Common Parameterizations of Swarm and Breakdown Data for Binary Gas Mixtures.	23
4.4 Corona-Induced Decomposition Rates of SF ₆ in SF ₆ /N ₂ , SF ₆ /Ne, and SF ₆ /O ₂ Mixtures.	30
4.5 Models for Decomposition of Gases in Corona Discharges.	35
4.6 Summary	40
5. INTERFACIAL PHENOMENA IN LIQUIDS	
Subtask No. 04.	40
5.1 Introduction.	40
5.2 High Precision Field Measurements: Room Temperature AC & DC	42
5.3 Space Charge in Transformer Oil at Room Temperature -- AC & DC.	43
5.4 Space Charge in Transformer Oil at 125°C -- AC & DC	45
5.5 Electrode Material Effects on the Generation of Space Charge.	45

curves are for no electric field. The time-of-flight for all trajectories is 50 ms. The volume occupied by the ions that enter aperture when $E \neq 0, V'$, exceeds volume of air, V , which enters in the same time. 18

Figure 10a. Measured pulse height distributions for electron avalanches formed near a positive point electrode in SF_6 at a pressure of 200 kPa for the indicated different water vapor concentrations and applied voltages. 22

Figure 10b. Measured electron avalanche repetition rates versus applied voltage at the indicated water vapor concentrations for avalanches larger than 0.08 pC. 22

Figure 11. Calculated differential electron detachment probabilities versus location between the point electrode surface d and the point x_c at which the ionization and attachment coefficients for the gas are equal for two different applied voltages. The different lines designate different assumed energy dependences of the cross sections for collisional detachment of negative ions with different indicated detachment thresholds ϵ_t 24

Figure 12. Fits (solid lines) to normalized critical field-to-gas density ratios for the mixtures SF_6/N_2 and CCl_2F_2/N_2 27

Figure 13. Examples of data on measured oxyfluoride concentrations versus net charge transported in the corona discharge for different indicated SF_6/Ne and SF_6/N_2 mixtures from which production rates were determined. 31

Figure 14. Examples of data on measured oxyfluoride concentrations versus net charge transported in the corona discharge for different indicated SF_6/Ne and SF_6/O_2 mixtures from which production rates were determined. 32

Figure 15. The complete set of electron collision cross sections for SF_6 used to calculate electron-induced dissociation rates of SF_6 in the mixtures SF_6/N_2 , SF_6/O_2 , SF_6/H_2O , and SF_6/Ne from numerical solutions of the electron

transport equation. The attachment, ionization, momentum transfer, vibrational excitation, and electronic excitation cross sections are respectively denoted by Q_a , Q_o^i , Q_m^{eff} , Q_{VIB} , and Q_x 34

Figure 16. Measured charge rates-of-production for the oxyfluorides and SO_2 normalized to the SF_6 concentration versus percent concentration of N_2 , O_2 , and Ne in the mixtures SF_6/N_2 , SF_6/O_2 , and SF_6/Ne . Also shown are total oxyfluoride plus SO_2 rates (r_t) in comparison with the predicted upper limits for the total rates for SF_6 decomposition. 39

Figure 17. Electro-optical, Kerr-effect, dc field measurements in transformer oil at room temperature. Solid lines show the negative polarity, dashed lines, positive polarity. The numbers in parentheses are the average applied field. In b) the normalized field is shown to emphasize the enhancement. In c) the normalized fields are shown for the 63 kV profiles to illustrate the temporal behavior of the enhancement after changing polarity. The dotted line is the field found just after the polarity is changed from positive to negative. After a few minutes the enhancement for the negative applied voltage gradually becomes that shown by the solid line 44

Figure 18. Normalized electric fields for 60 Hz ac at room temperature. NP and PP refer to negative peak and positive peak respectively. The sudden drop in the positive peak profile near the HV electrode is an artifact of the detector and not some unusual decrease in the field near the plate. The average peak field is 232 kV/cm. 46

Figure 19. Electric fields for dc at 125°C. At lower fields there is less space charge near the cathode. 47

Figure 20. Electric fields for 60 Hz ac at 125°C. NP and PP refer to the negative and positive peaks of the 60 Hz waveform respectively. The average peak field is 224 kV/cm. The space charge, which is proportional to the derivative of the field, is shown for the negative peak profile. 48

Figure 21. Multi-metal electrode configuration to reveal dramatic difference between electrode metals in production of space charge while employing

the same liquid. The gap is 0.635 cm, plate width is 1.27 cm and the length of the plates is 15 cm (into the page) 50

Figure 22. Intensity profiles for different electrode materials under the application of 50 kV dc, both polarities, room temperature. No attempt has been made to compensate these data for nonuniform incident light intensity. Since large diameter windows having a residual birefringence were used the intensity profiles on the average have a slight slope. The important feature is that the same space-charge behavior is noted independent of electrode material 51

Figure 23. Waveforms used in studies measured directly from pulse generator. The test waveform does not replicate beyond 40 ns as indicated. 56

Figure 24. Output signals from a capacitive sensor for test line input signals shown in figure 1. 56

Figure 25. Comparison of deconvolved and input signals for the capacitive sensor. Signals have been offset for comparison. 57

Figure 26. Comparison of the output signal from a resistor divider with the input signal. 57

Figure 27. Deconvolved and directly measured input signals as obtained using the resistor divider. Signals have been offset for comparison. 59

Figure 28. Schematic of system to measure electrical quantities using electro-optic sensors 61

Figure 29. Trapezoidal waveform used in Pockels effect response calculation. For the calculations shown in figure 30, only the maximum electric field is changed 63

Figure 30. Normalized intensity of light for Pockels effect measurement described in text and for waveshape shown in figure 29. Raggedness in waveshape is due to coarseness of time grid used for calculations. a. $E_m = 0.5$ Mv/m.
 b. $E_m = 1$ Mv/m. c. $E_m = 2$ Mv/m. 64

Figure 31. Configuration used to determine the response of the water resistor used to measure the voltage waveform applied to the gap. Response is shown schematically on the figure 65

Figure 32.	Cross sectional view of system used to study liquid dielectric breakdown processes under nanosecond pulse conditions. Construction details, such as types of materials, have been omitted for clarity. The flow of oil through the sharpening gap and the test region is indicated, as is the water capacitor used for pulse shaping.	67
Figure 33.	Representative images obtained from high speed photography of the breakdown process. The voltage waveform changes from zero to the maximum value between frames 2 and 4. The initiation of the supersonic streamer growth is observed in frame 4, and the breakdown process is complete in frame 6. There is no slow bush-like growth like that observed in studies using slower waveforms	68
Figure 34.	Comparisons of framing camera pictures of streamer growth in N-Hexane showing two different streamer speeds. a. Breakdown voltage of 120 kV, with time between exposures of 500 ns. Order of exposure is that shown in (fig. 33). b. Breakdown voltage of 240 kV, with 50 ns time between exposures. 7.05, 6.28 (± 0.4)	69

LIST OF TABLES

Table 1.	Space Potential Perturbations.	12
Table 2.	Possible negative ion formation and destruction processes in binary, molecular gas mixture	29

RESEARCH FOR ELECTRIC ENERGY SYSTEMS -- AN ANNUAL REPORT

Robert E. Hebner, Editor

Abstract

This report documents the technical progress in the five investigations which make up the project "Support of Research Projects for Electrical Energy Systems," Department of Energy Task Order Number 137, funded by the U.S. Department of Energy's Office of Energy Systems Research and performed in the Electrosystems Division of the U.S. National Bureau of Standards. To support the measurement of ac electric and magnetic fields, a magnetic field meter was designed, constructed, and calibrated. The meter has bandwidth and sensitivity sufficient to measure ambient magnetic fields. The measurement support for dc fields and ions focussed on techniques to calibrate ion counters. A standard ion source was characterized and the effects of air flow were modeled. Within the project to develop measurement techniques and obtain basic data for gaseous dielectrics, the influence of trace amounts of water on avalanche initiation in SF₆ has been measured and the results have been explained in terms of electron detachment of negative ions. In addition, a method for fitting the variation of the breakdown strength of binary gas mixtures with changes in concentration was developed and evaluated using published data. The decomposition rates induced by corona in mixtures of SF₆ with nitrogen, with oxygen, and with neon were measured. The results are explained using a theoretical model for chemical decomposition of gases in high-pressure corona. Progress in the measurement of the electrical behavior at the interfaces in liquid-solid composite insulation included improvement of the instrumentation used to measure the electrical field and the space charge in transformer oil so that the inaccuracy is less than 1% and the imprecision is less than 0.2%. Using this system, it has been shown for the oils and field strengths used in this study that the space charge density is relatively unaffected by a change of electrode material from steel to copper to aluminum to brass. Using high speed photography, it was shown that hydrostatic pressure has a significant effect on the prebreakdown streamers. Finally optical and electrical measurements were combined to obtain insight into the nature of partial discharges in insulating fluids. Techniques to evaluate sensors used to measure nanosecond voltage and current pulses have been explored in the project dealing with nanosecond breakdown in power system dielectrics. Deconvolution methods to evaluate sensor behavior have been developed and used. Initial measurements suggest that the propagation of prebreakdown streamers in power system dielectrics may be different under nanosecond pulses than under microsecond pulses in oil.

1. INTRODUCTION

Under an Interagency Agreement between the U.S. Department of Energy and the National Bureau of Standards, the Electrosystems Division, NBS, has been providing technical support for DOE's research on electrical energy systems. This document summarizes the technical accomplishments of this program during fiscal year 1985. The Interagency Agreement specifies five tasks which are to be performed and a description of the technical progress in each task constitutes a section of this report. Section 2 describes the work in ac electric and magnetic fields and section 3 describes the investigation of dc field and ion measurements. Section 4 summarizes the development of the measurement techniques and the accumulation of fundamental data needed for gaseous dielectrics research. Section 5 describes the development of techniques to measure interfacial phenomena in liquids. The final technical project, which deals with the measurement of nanosecond breakdown in power system dielectrics, is summarized in section 6.

2. AC ELECTRIC AND MAGNETIC FIELDS

Task 01

Martin Misakian and P. Michael Fulcomer
Electrosystems Division
National Bureau of Standards

2.1 Introduction

The objective of this investigation is to provide electrical measurement support for efforts to determine the effects of power frequency electric and magnetic fields on biological systems. To accomplish this objective, NBS establishes and maintains facilities to evaluate the performance of probes used by researchers in biological investigations as well as fieldmeters used in the vicinity of transmission lines.

Recent speculation on the possible bioeffects of weak power frequency magnetic fields has focused attention on the characterization of such fields. NBS has developed an ac magnetic fieldmeter-spectrum analyzer combination for measuring ambient magnetic fields with frequencies from about 10 Hz to 3 kHz. A description of the fieldmeter's characteristics is given below.

2.2 Ambient Magnetic Field Meter

A portable, battery powered, magnetic field meter has recently been developed to provide improved accuracy in the measurement and analyses of low level ambient magnetic fields produced, both indoors and outdoors, by 60-Hz power lines and equipment. It is designated "AMFM-1" for Ambient Magnetic Fieldmeter-Version #1. The fieldmeter consists of two parts: (1) a magnetic-field probe consisting of 2000 turns of electrically shielded wire wound on a donut-shaped non-inductive core, approximately 10-cm in diameter, which is connected by standard 50- Ω coaxial cable to (2) a chassis box approximately 7-cm x 20-cm x 25-cm deep, which contains a detector consisting of amplifiers, an integrator, buffers, and battery-power supply. Also included on the chassis box is a small analog display for ease in determining the maximum field at a given location and for checking battery voltage. The rms value of the output signal is read with a portable multimeter (provision has been made

for later incorporating a digital display on the chassis box). A portable, low-frequency (5 Hz to 50 kHz), spectrum analyzer is also included as part of the measurement system. Connection of the spectrum analyzer to the AMFM-1 permits the determination of the harmonic components in the magnetic field. The percentages of the harmonics can be measured with an uncertainty of less than $\pm 5\%$.

Five ranges from 0.2×10^{-7} tesla (0.2 milligauss) to 2×10^{-4} tesla (2 gauss) full scale are provided by the AMFM-1. Measurements down to 20×10^{-10} tesla (20 microgauss) are possible on the most sensitive range with an uncertainty of less than $\pm 2\%$. The frequency response is, at present, limited mainly by the probe (pickup coil) and varies less than -1dB from approximately 10 Hz to 3 kHz, thus allowing complex fields consisting of a 60 Hz fundamental and various percentages of harmonics and subharmonics to be characterized. Between 30 Hz and 600 Hz, the frequency response is flat to within $\pm 1\%$. The frequency response of the detector (not including the probe) varies less than ± 1 dB from 10 Hz to more than 20 kHz.

Current drain from each of two 9-volt alkaline batteries is approximately 6 mA thus allowing at least 24 hours of continuous operation of the AMFM-1 (and somewhat longer total hours of operation when used intermittently) on one set of batteries.

The signal from the probe is proportional to the derivative of the magnetic field. Consequently, the percentage of each harmonic present in the magnetic field is weighted by its harmonic number. Thus, in addition to amplifying the signal from the probe, the detector integrates the signal to eliminate the undue weighting. However, the integrator must follow some stages of amplification to avoid signal-to-noise problems in the integrator. One potential difficulty resulting from this approach is that signals due to higher order harmonics, with their undue weighting and amplification, can overload the last amplifier stage i.e., "clipping" occurs. A reduced overall output would solve this problem but at the expense of good low noise performance on the most sensitive scale. Other solutions would be to reduce the dynamic range of the instrument or to place the integrator in the middle of the amplifier stages and use a more complicated range switching arrangement. None of these alternatives were used in the present instrument because each has an offsetting disadvantage and because even at full scale output (where the clipping would first occur), the AMFM-1 responds to signals up to 600 Hz without clipping on all but the 2×10^{-4} tesla range. This means that in most practical situations (where ambient fields are less than $\sim 0.2 \times 10^{-4}$ tesla) the 10th harmonic of 60 Hz could be equal to 100% of the fundamental and still be measured correctly by the AMFM-1. For output signals which are a lower percentage relative to the fundamental, the harmonic frequency that can be measured (i.e., no clipping occurs) increases as shown in figure 1. As an example, the harmonics of a signal whose fundamental amplitude is at the low end (15% or less) of full scale can be measured to beyond 3 kHz, even if the harmonics are equal in amplitude to the fundamental. The same approximate 3 kHz limit applies to harmonics which are less than approximately 15% of a full scale fundamental. This performance will enable accurate measurement for nearly all practical situations and further complication of the design was not warranted.

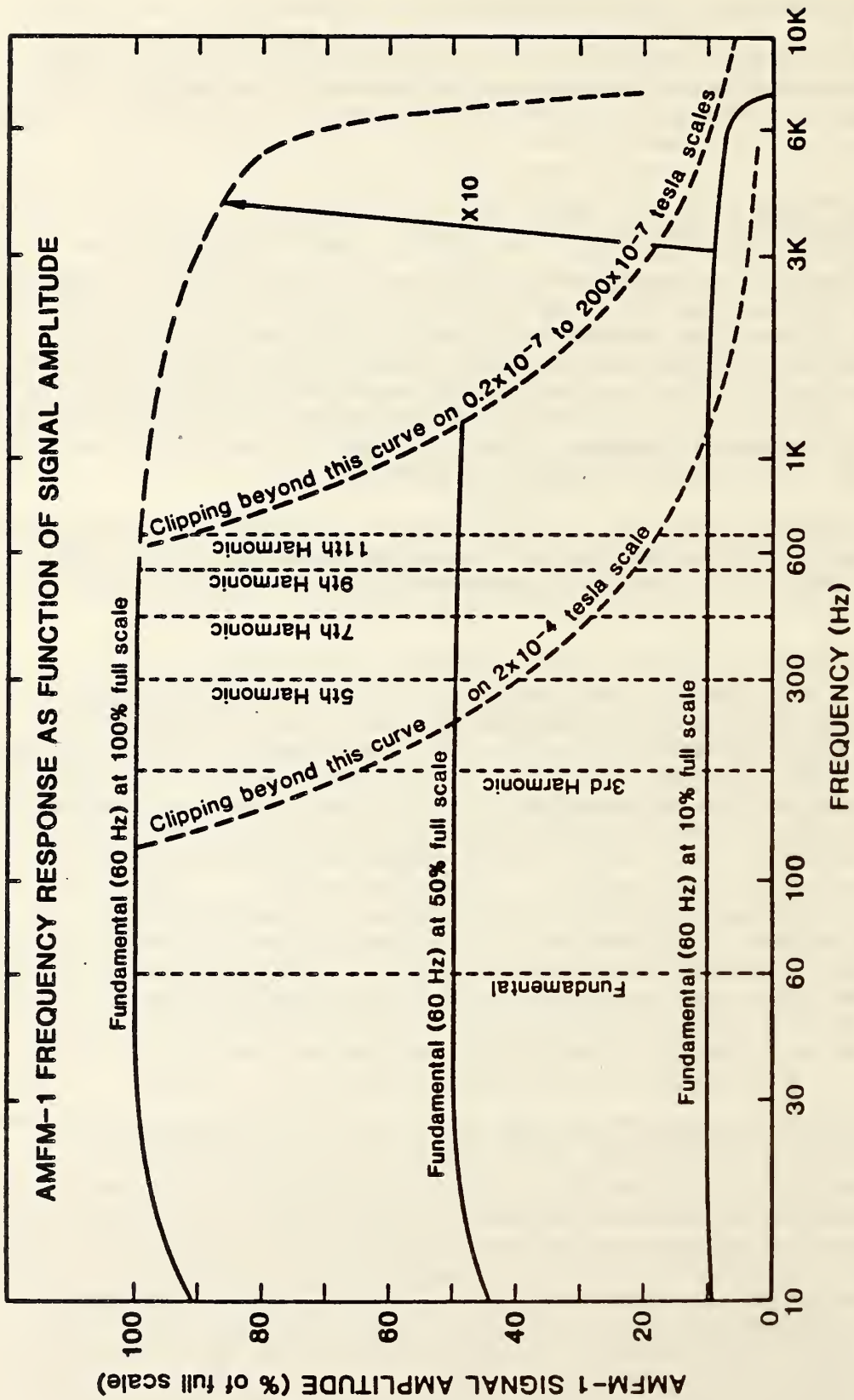


Figure 1. AMFM-1 frequency response as function of signal amplitude. Frequencies at which clipping occurs (see text) for the various scales are indicated.

On the least sensitive range (2×10^{-4} tesla), clipping of harmonics which are 100% of the fundamental will occur at full scale output for frequencies above 120 Hz. The clipping point increases to 240 Hz for 50% harmonics and to 1.2 kHz for 10% harmonics. Figure 1 gives a summary of the above results.

A check to determine if clipping is occurring can be made by switching the detector to the next higher (less sensitive) range. The signal reaching the integrator will now be a smaller percentage of full scale and less, or no clipping will occur. The readings for the two ranges will remain essentially unchanged if no clipping is occurring.

Calibration of the AMFM-1 on all but the two most sensitive ranges was performed using a magnetic field produced with a Helmholtz coil. Because of the perturbations of ambient magnetic fields, a voltage injection technique is used to check the calibration of the two most sensitive ranges.

Figure 2 shows an oscilloscope display of the current waveform to the Helmholtz coils (which coincides with that of the magnetic field) superimposed on the waveform of the output signal from the AMFM-1. The current to the Helmholtz coil is produced with a programmable waveform generator-power amplifier combination and contains a 3rd harmonic with a magnitude of about 40% of the fundamental, a 5th harmonic which is 19% of the fundamental, a 7th harmonic which is 8.5% of the fundamental, and a 9th harmonic which is 4% of the fundamental. The phases of the 3rd and 5th harmonics have been shifted $+90^\circ$ relative to the 60 Hz fundamental and the 7th and 9th harmonics are in phase with the fundamental. The amplitudes of the two waveforms in figure 2 have been made the same for purposes of comparisons. Figure 3 is the spectrum analyzer display for the two waveforms shown in figure 2. No differences between the two superimposed oscilloscope traces in figures 2 and 3 are discernable, indicating that for the frequencies shown the AMFM-1 adequately characterizes the spectral composition. A fuller account of the design, calibration procedure, and measurement uncertainties for the AMFM-1 is being prepared.

2.3 Summary

To aid in the characterization of ambient ac magnetic fields, a portable magnetic fieldmeter-spectrum analyzer system has been developed to measure fields as low as 20×10^{-10} tesla for frequencies from about 10 Hz to 3 kHz.

3. DC FIELDS AND ION MEASUREMENTS

Task 02

Martin Misakian and Ronald H. McKnight
Electrosystems Division
National Bureau of Standards

3.1 Introduction

The objective of this project is to develop methods to evaluate and calibrate instruments which are used, or are being developed, to measure the electric field, the space charge density, the current density, and related

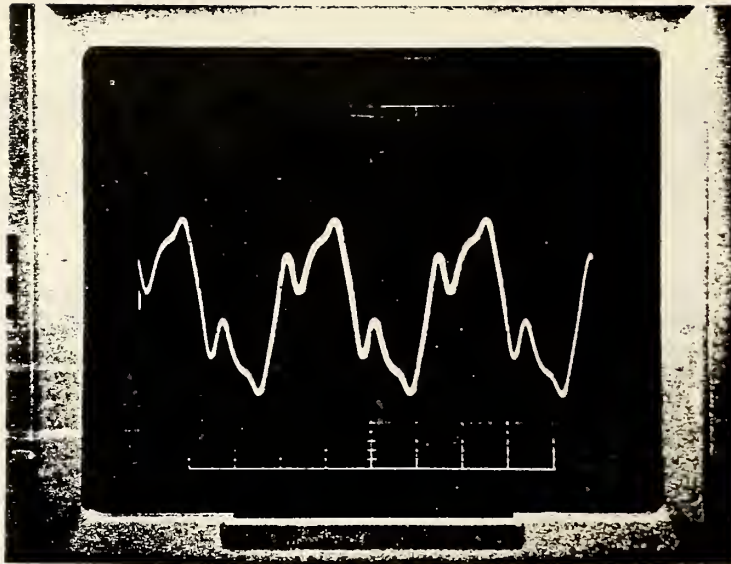


Figure 2. Oscilloscope display of current waveform superimposed on waveform of output signal from AMFM-1. Amplitudes of two waveforms have been made equal for purposes of comparison.

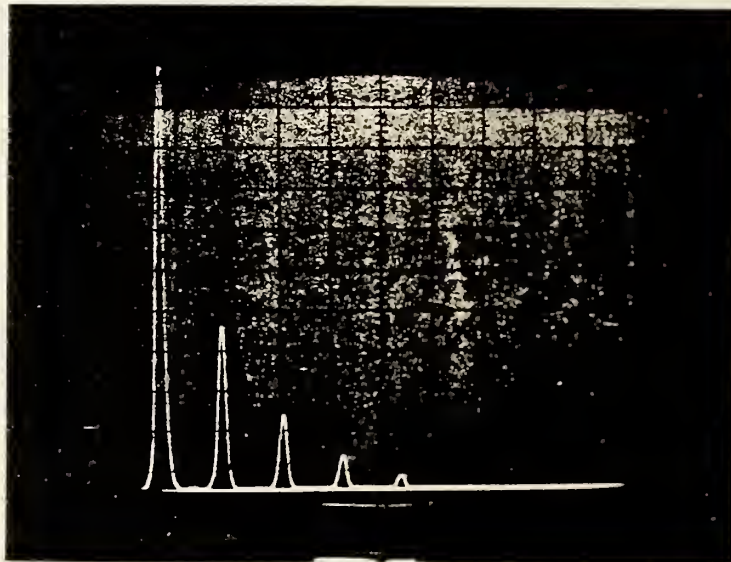


Figure 3. Spectrum analyzer display indicating frequency components of the waveforms shown in figure 2. The traces for the two waveforms are superimposed.

electrical parameters in the vicinity of high-voltage dc transmission lines and in apparatus designed to simulate the transmission line environment.

To carry out this objective, it is necessary to evaluate and/or to develop instrumentation required to characterize the electrical environment in exposure facilities and near transmission lines. The specific investigations required include the determination of the effect of ion current on electric field measurement, the characterization of the effects of electric fields on the collection efficiency of aspiration-type ion measurement instruments, and the identification of the size and type of ion which makes up space charge. The primary focus during this reporting period was the evaluation of the performance of ion measurement instruments.

A method for experimentally calibrating an aspirator-type ion counter presently does not exist because of the lack of a standard ion source. In earlier reports [1-3], the NBS parallel plate system [4] was theoretically examined to determine if it could be used to produce a known ion density for calibration purposes. Originally designed for establishing a known dc electric field with space charge (for calibration of dc electric field strength meters), the ion density profile between the parallel plates is readily calculated. We present here the results of recent measurements which establish, under certain conditions, the suitability of the parallel plate apparatus as a means for producing a known unipolar ion density. In addition, the effects of an electric field and air motion on ion transport into an aspirator-type ion counter operating in the ground plane are examined by calculation of ion trajectories into the ion counter.

3.2 NBS Parallel Plate Apparatus and Approach

The design and operation of the NBS parallel plate apparatus has previously been described in detail [4] and is discussed here only briefly. A schematic view of the apparatus is shown figure 4. Ions generated by stainless steel corona wires are directed both upward (to the cap) and downward to the first screen. Ions not collected on the first screen continue downward to the second screen which is the top "plate" of a parallel plate system. The ions which pass through the top plate travel a distance d to the bottom plate and form the current density J . Electrically isolated current sensing patches mounted on the bottom plate are used to measure J . The side dimensions of the parallel plates are 1.7 m x 1.7 m and the spacing is near 0.17 m for most of the present studies.

The solution of Poisson's equation in one dimension yields expressions for the electric field strength, $E(z)$, and electric space potential, $\Phi(z)$, between the parallel plates [4];

$$E(z) = [E_0^2 + 2Jz/K\epsilon_0]^{1/2}, \text{ and} \quad (1)$$

$$\Phi(z) = V_c - (K\epsilon_0/3J)[(E_0^2 + 2Jz/K\epsilon_0)^{3/2} - E_0^3], \quad (2)$$

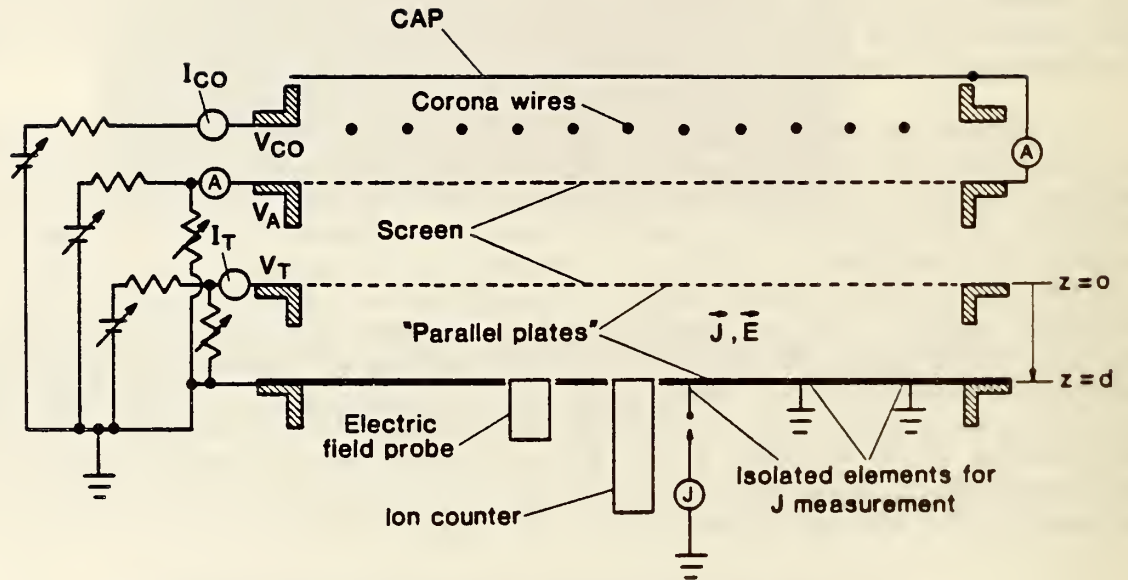


Figure 4. Schematic view of NBS parallel plate apparatus. The arrangement shown is appropriate for generating an electric field with positive space charge. The top and bottom plates of the parallel plate system are located in the planes $z = 0$ and $z = d$. The corona wires are oriented parallel to one another and are perpendicular to the plane of the figure.

where V_t is the potential of the top plate ($z=0$), E_0 is the electric field at the top plate, K is the average ion mobility, and ϵ_0 is the permittivity of free space.

Following procedures described in [4], the values of K and E_0 can be determined experimentally, thus permitting the calculation of E from eq (1) for a given current density. The constitutive relation for conduction current density,

$$J = \rho KE \quad (3)$$

can then be used to determine the charge density, ρ , as a function of z . It should be noted that J is approximately constant between the parallel plates because there are no sinks or sources of ions in this region. The ion density decreases and the electric field increases as a function of distance, z , from the top plate.

Figure 5 shows the results of model calculations of normalized positive ion density for $J = 1.0 \times 10^{-6} \text{ A/m}^2$, $K = 1.3 \times 10^{-4} \text{ m}^2/\text{Vs}$, $V_t = 2650 \text{ V}$, and $d = 0.17 \text{ m}$. A decrease of 49% in ion density occurs between the top and bottom plates. Decreasing J by a factor of ten while keeping K , V_t , and d fixed results in a decrease of only 6.0%. The relatively small change in ρ for the second case suggests that the parallel plate apparatus might be used for generating a "known" or calculable ion density (i.e., in this example, known within about $\pm 3\%$) for an aspirator-type ion counter operating in the ground plane. However, in order to use eqs (1) and (3) to calculate the unperturbed charge density profile, it must be shown that (1) the air motion due to the operation of the ion counter perturbs the ion density only in a volume near the aperture of the ion counter and does not extend significantly to the upper regions of the parallel plate system, and (2) it must also be demonstrated that the perturbation of the ion density due to the aperture of the ion counter is restricted mainly to the volume near the aperture. Figure 6 shows schematically the conditions described above.

An estimate of the electric field perturbation due to an aperture in the ground plane can be made by numerically calculating the electric field for the geometry shown in figure 6, in the absence of space charge. Such a calculation has been performed at NBS [1], but the uncertainties in the field values and the associated space potentials are not well characterized. Analytic expressions for the electric field and potential for a circular aperture in the ground plane of a large parallel plate system have been derived by Fry [5]. The electric potential, Φ' , and field, E' , along the symmetry axis (z -axis) are given by

$$\Phi' = E_u [z/2 + R/\pi + (z/\pi) \tan^{-1}(z/R)], \quad (4)$$

and

$$E' = E_u [(1/2) + zR/\pi(R^2+z^2) + (1/\pi) \tan^{-1}(z/R)], \quad (5)$$

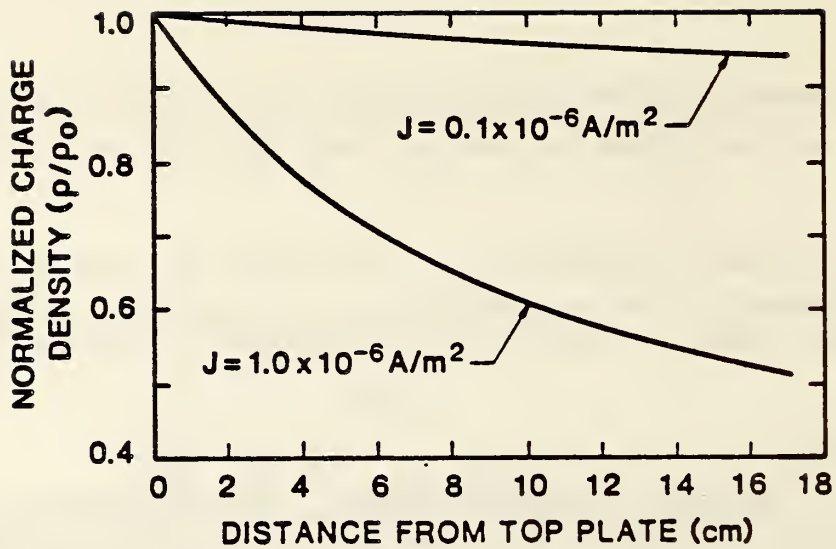


Figure 5. Normalized ion density profiles for two current densities, $1 \times 10^{-6} \text{ A/m}^2$ and $0.1 \times 10^{-6} \text{ A/m}^2$. The calculated results assume that $V_t = 2650 \text{ V}$, $K = 1.3 \times 10^{-4} \text{ m}^2/\text{Vs}$, and $d = 0.17 \text{ m}$.

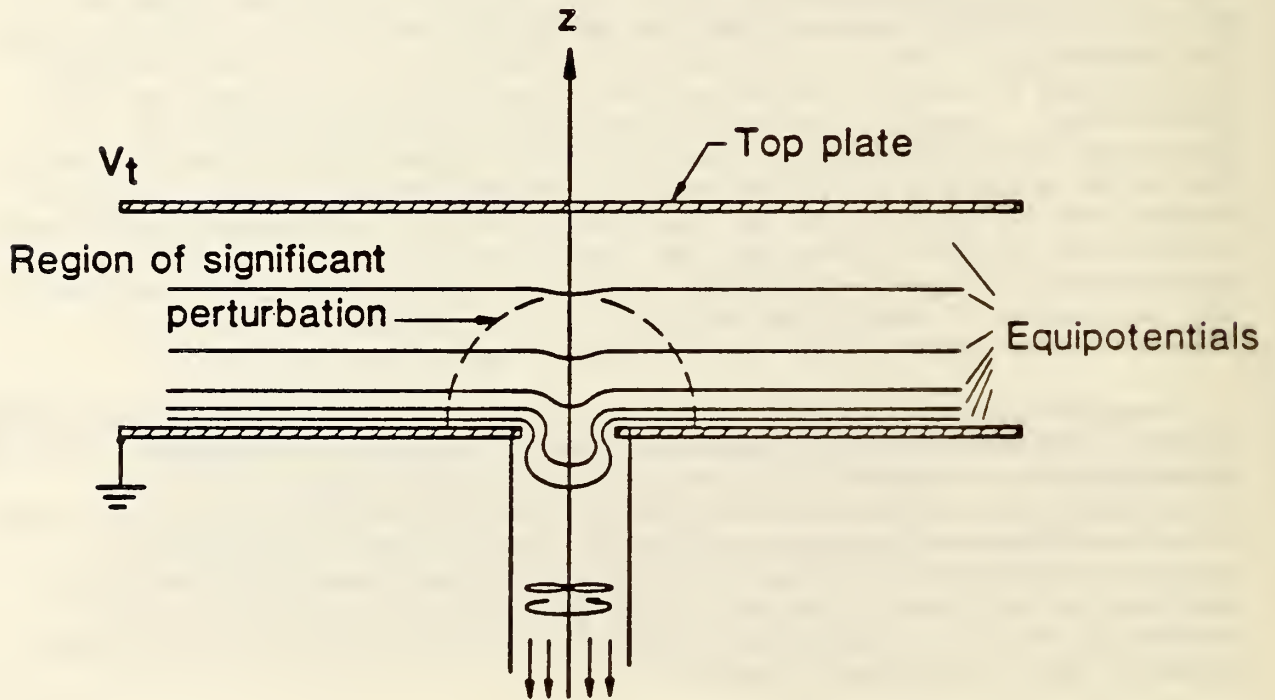


Figure 6. Schematic view showing perturbations of electric field and charge density due to an aperture in the ground plane and air motion do not extend across the parallel plate spacing.

where E_u is the unperturbed uniform electric field (prior to introduction of aperture) and R is the radius of the aperture. Unlike eqs (1) and (2), z is taken to be zero in the ground plane in eqs (4) and (5). Expressing eqs (4) and (5) as normalized by the unperturbed potential ($E_u z$) and unperturbed electric field (E_u), respectively, we have

$$(\Phi'/E_u z) = [1/2 + R/\pi z + (1/\pi)\tan^{-1}(z/R)], \quad (6)$$

and

$$(E'/E_u) = [1/2 + zR/\pi(R^2+z^2) + (1/\pi)\tan^{-1}(z/R)] \quad . \quad (7)$$

As z increases, the departure of Φ' and E' from the corresponding uniform field values decreases and the magnitude of the electric field perturbation approaches twice the value of the space potential perturbation [6], i.e.,

$$\lim_{z \rightarrow \infty} |(E' - E_u)/E_u| = 2|(\Phi' - E_u z)/E_u| \quad . \quad (8)$$

At a height of two diameters above the aperture (along z -axis), the perturbation of Φ' is + 0.16% and the perturbation of E' is -0.31%. At a given height, the perturbations decrease as a function of distance from the z -axis [5].

The perturbation of the electric field and charge density due to the air motion has not been calculated, but knowledge of the air speed as a function of distance from the aperture provides some insight into the problem. The air motion above the aperture has been modelled theoretically and calculated air speed values along the z -axis compare favorably with experimentally determined values [3]. The air speed along the z -axis is given by [3]

$$u = u_0 [1 - z/(R^2+z^2)^{1/2}], \quad (9)$$

where u_0 is the air speed in the plane of the aperture and R is the radius of the aperture. The "effective radius" of the square hole used for the experimental measurements was found by setting πR^2 equal to the area of the hole. At a point which is four radii above the aperture, the calculated air speed is 3% of u_0 . To put this result into perspective, it should be noted that the air speed at the entrance of a commercial ion counter can be as high as 1 m/s. This compares with a drift velocity of about 1.4 m/s for a positive ion in a 10 kV/m electric field. Thus, close to the aperture, the air speed can be comparable to the ion drift velocity and significant perturbation of the ion density (in addition to perturbation due to aperture) may occur. However, it appears that the influence of the air motion caused by the fan in the ion counter at a point which is four radii above the aperture, ~3 cm/s in the above example, will be small.

The above discussion suggests that a parallel plate apparatus with a spacing greater than four times the ion counter aperture and with an ion density profile that changes by less than about 6% may be suitable as a standard ion source. It is recalled, however, that the discussion regarding perturbation of the electric field due to an aperture in the ground plane did not consider the presence of space charge. Because the introduction of an aperture affects the surface charge density on the parallel plates as well as the volume charge density between the plates, field perturbations due to the aperture are expected to be greater than for the space-charge free case considered above. Measurements of the electric space potential have been made in the NBS parallel-plate system as a function of distance above an aperture in the bottom plate and compared with space potential values without an aperture. The effect of air flow through the aperture on the space potential has also been examined. An estimate of the electric field perturbation is then made using eq (8).

3.3 Space Potential Perturbation Measurements

Measurements of the electric space potential between the parallel plates, in the presence of space charge, were made with a space potential probe very similar in design to one reported by Penney and Matick [7] and Matick [8]. With $V_t=2650$ V, $d=0.17$ m and $J=0.25 \times 10^{-6}$ A/m², measurements of the space potential were made as a function of height above the bottom plate, with and without a 5 cm x 5 cm aperture. The space potential probe was located over the aperture and could be made to move vertically with a screw-driven vertical displacement apparatus located outside the parallel plate system. The "no-aperture" condition was established by sliding a sheet of stretched aluminum foil over the aperture. Figure 7 shows examples of graphs of probe potential, V_p , versus guard potential, V_g , near the intersections with the line $V_p = V_g$ at various heights above the bottom plate, with and without the aperture. The perturbation of the space potential due to the aperture are expressed in volts and percentages at each height. For purposes of comparison with perturbations predicted by eq (6), which is valid only for space-charge free conditions, the "radius" of the square aperture is made to satisfy the relation $\pi R^2 = 25$ cm², i.e., $R=2.82$ cm. Table 1 shows the results of perturbation measurements made over a period of several days. Uncertainties in the perturbation measurements are shown in parentheses in table 1 and are due mainly to uncertainties in reading the electrostatic voltmeters used to measure the probe potential and to small drifts in the electrostatic voltmeter reading. As expected, the measured perturbations of the space potential exceed the values predicted by a theory that ignores space charge.

Table 1. Space Potential Perturbations

<u>Height Above Bottom Plate</u>	<u>% Perturbation of Φ' [eq(6)]</u>	<u>% Perturbation Measured ($\rho \neq 0$)</u>
4R	0.16	0.37, 0.31, 0.48, 0.37 (± 0.10)
3R	0.37	0.70, 0.68 (± 0.15)
2R	1.16	1.86, 1.60, 1.83, 1.80 (± 0.20)
1.1R	5.96	7.05, 6.28 (± 0.40)

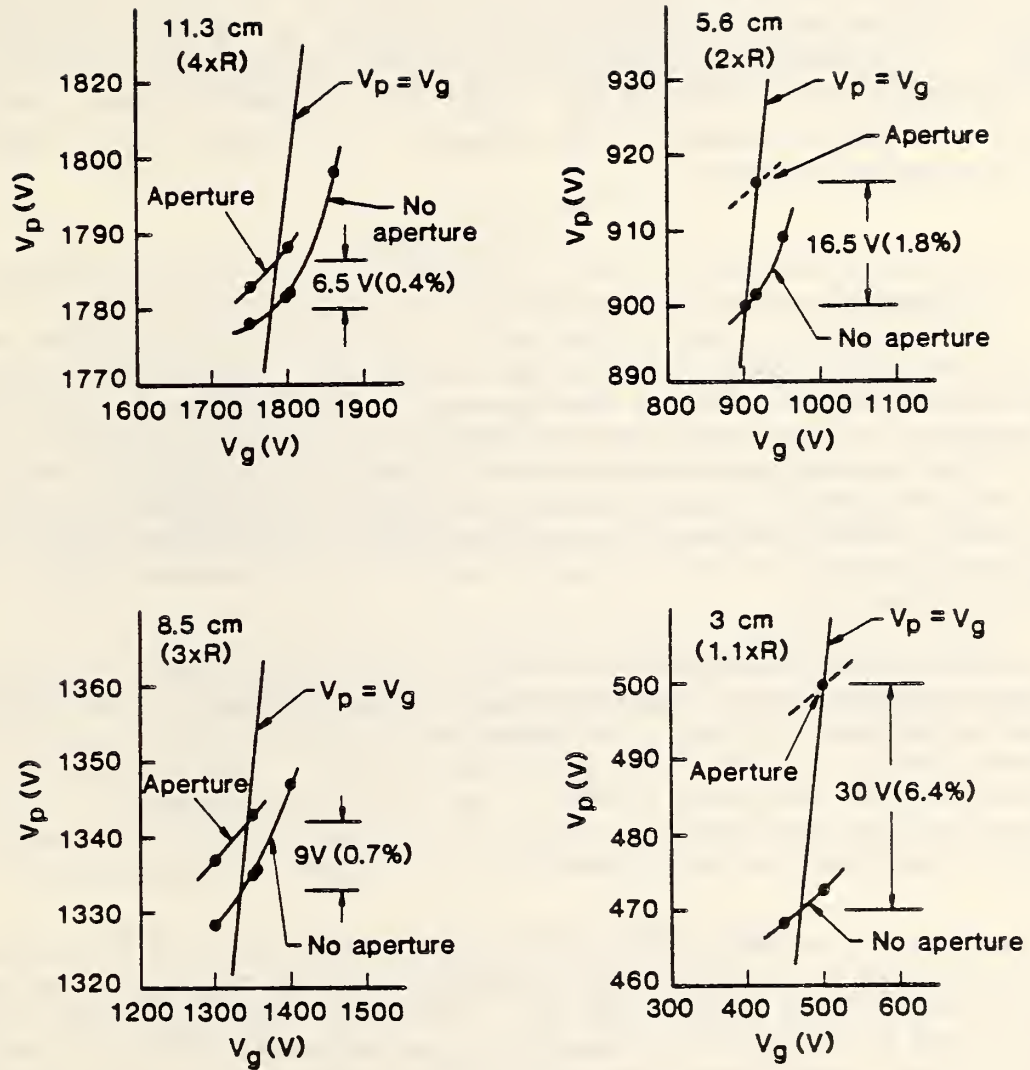


Figure 7. Measurements of space potential perturbation due to 5 cm x 5 cm aperture in ground plane as a function of height above ground plane.

The additional perturbation due to air motion was examined by drawing air through the aperture. The air flow was measured with a turbine-type flowmeter and the air speed in the plane of the aperture was calculated by assuming a uniform velocity across the opening. No measureable (i.e. >0.1%) change in space potential could be observed at a height of 11.3 cm (4R) above the aperture for average air speeds between 1.6 m/s to 6.6 m/s in the plane of the aperture. The apparently negligible influence of the air motion at 11.3 cm is an interesting result because the calculated air speed, when u_0 is 6.6 m/s, is about 10% of the calculated drift velocity at the same height. This result will be examined further.

3.4 Discussion

The measurements of the preceding section (for $V_t=2650$ V, $K=1.3 \times 10^{-4} \text{ m}^2/\text{Vs}$, $d=0.17$ m, $J=0.25 \times 10^{-6} \text{ A/m}^2$) suggest that the space potential perturbation due to the aperture at a distance of four radii above the aperture is about 0.4% and the effects of air motion due to the fan in the ion counter are negligible when the air speed is as large as 6.6 m/s in the plane of the aperture. Measurements at significantly greater distances above the aperture were prevented by possible contact between the space potential probe and a portion of the top plate which extends downward along the perimeter (fig. 4).

If the electric field perturbation at four radii above the aperture is estimated using eq (8), a perturbation of less than about -1% is expected. The perturbations of E and ρ are expected to be much smaller than 1% at the top plate which is 0.17 m (6R) above the aperture. For points off the z -axis, the perturbation decreases further. Thus, the requirement that significant perturbations of the field not extend to the top plate of the parallel-plate system is realized for the values of J , V_t , K and d indicated above.

Calculation of the unperturbed charge density profile indicates that ρ increases by 16.5% from the bottom plate to the top plate; the increase to a height of four radii is only 10% [9]. The small perturbation of ρ due to the aperture and the absence of a measurable perturbation due to air motion at a height of four radii above the bottom plate suggests that the sampling region of the ion counter is below this height. Thus, the range of unperturbed ion densities sampled by the ion counter varies less than about +10% from the value at the bottom plate. Taking the median unperturbed value of ρ to be the "known" ion density, the uncertainty in ρ becomes $\pm 5\%$ in the absence of other uncertainties.

To determine the total uncertainty in ρ , the steps in its calculation must be considered. It is recalled that ρ is given by, from eq (3),

$$\rho(z) = J/KE(z), \quad (10)$$

where

$$E(z) = [E_0^2 + 2Jz/KE_0]^{1/2} \quad (11)$$

Using techniques described in Reference 4, K can be measured with an uncertainty of less than $\pm 6\%$, J is measured with an uncertainty of less than $\pm 6\%$, and E(z) can be calculated using the values of J and K with an uncertainty of less than $\pm 1\%$. The parameters J and K are independent but E(z) is correlated with J and K. Adding the uncertainty in E(z) to that of K, the rms uncertainty in the median value of ρ is less than $\pm 10\%$. Finally, adding $\pm 5\%$ uncertainty to take account of the range of (unperturbed) charge densities being sampled by the ion counter, the total uncertainty in ρ becomes less than $\pm 15\%$.

3.5 Ion Trajectories and Losses

The transport of ions into an aspirator-type ion counter under the influence of an electric field and air motion is examined in a semi-quantitative manner in this section. In the model that is considered, a circular aperture of radius R is used to approximate a square aperture of an ion counter of side dimension 2R. It is assumed that the ions travel along trajectories determined by the addition of the ion drift velocity (product of ion mobility and electric field strength) and air velocity, and do not contribute to the magnitude or direction of the electric field which is essentially space-charge free. The trajectories are taken to be in the vertical y-z plane.

The electric field is found by taking the negative gradient of the electric potential derived by Fry for a uniform space-charge-free electric field perturbed by a circular aperture of radius R in the ground plane [5],

$$\vec{E}' = -\nabla\phi', \quad (12)$$

where

$$\phi' = A\{\sinh\lambda + (2/\pi)[1 + \sinh\lambda \cdot \tan^{-1}(\sinh\lambda)]\sin\mu, \quad (13)$$

λ and μ are oblate spheroidal coordinates and are related to Cartesian coordinates by the equations

$$y = R \cosh\lambda \cos\mu, \quad (14)$$

$$z = R \sinh\lambda \sin\mu, \quad (15)$$

and A is $E_u R/2$.

The horizontal and vertical drift velocities, v_y and v_z , are given by

$$v_y = KE'_y, \text{ and} \quad (16)$$

$$v_z = KE'_z, \quad (17)$$

where

$$E'_y = - (AS \sin\mu \cos\mu \sinh\lambda/B) - (AT \sin\mu \cos\mu \cosh\lambda/B), \quad (18)$$

$$E'_z = - (A \sin^2 \mu \cosh \lambda / B) + (AT \cos^2 \mu \sinh \lambda / B), \quad (19)$$

$$S = [\cosh \lambda + (2/\pi) \cosh \lambda \tan^{-1}(\sinh \lambda) + (2/\pi) \tanh \lambda], \quad (20)$$

$$T = [\sinh \lambda + (2/\pi) + (2/\pi) \sinh \lambda \tan^{-1}(\sinh \lambda)], \quad (21)$$

and

$$B = R (\cosh^2 \lambda - \cos^2 \mu) \quad (22)$$

An expression for air velocity for points above the aperture is [3]

$$\vec{u}(\vec{r}) = -(u_0/2\pi) \iint_{\Omega} |\vec{r}-\vec{r}'|^{-3} (\vec{r}-\vec{r}') dx' dy', \quad (23)$$

where u_0 is the air speed in the plane of the aperture, \vec{r} and \vec{r}' are position vectors above and in the plane of the aperture respectively, x' and y' are Cartesian coordinates in the plane of the aperture and Ω is the area of the aperture. Equation (23) is used to obtain the air velocity components above the aperture. Along the z-axis, eq (23) reduces to eq (9) and as noted earlier the air velocity values are well predicted by eq (9) when an "effective radius" is used for R. The off-axis values of velocity predicted by eq (23) have been compared with preliminary measurements and appear to be too high. However, the off-axis inaccuracies should not affect the semi-quantitative conclusions of this section.

For a square aperture of side dimension $2R$, eq (23) can be integrated and yields the following expressions for the air velocity components:

$$u_y = - (u_0/2\pi) \log [(R+F)(-R+G)/(-R+F)(R+G)], \text{ and} \quad (24)$$

$$u_z = - (u_0/2\pi) [\tan^{-1}(R(y+R)/zG) - \tan^{-1}(R(y-R)/zF)], \quad (25)$$

where

$$F = [R^2 + (y-R)^2 + z^2]^{1/2}, \text{ and} \quad (26)$$

$$G = [R^2 + (y+R)^2 + z^2]^{1/2} \quad (27)$$

In the y-z plane where the ion trajectories are calculated, the edges of the circular and square apertures coincide. It should be noted that the velocities along the z-axis predicted by eq (25) for a square aperture agree well with the results obtained using the simpler expression for a circular aperture, eq (9), if the radius of the circular aperture is taken to be the "effective radius."

For $z > 0$, the equations of motion for positive ions under the influence of the electric field and air motion through the aperture are

$$dy/dt = v_y + u_y, \text{ and} \quad (28)$$

$$dz/dt = v_z + u_z, \quad (29)$$

where the ion drift and air velocities are given by eqs (16)-(17) and eqs (24)-(25). Below the plane of the aperture, the air speed is approximated by a constant velocity, u_0 , parallel to the z-axis.

Equations (28) and (29) have been solved on a computer using a variable step-variable integration method with software developed at NBS [10]. Examples of trajectories for $E_u = 15 \text{ kV/m}$, $u_0 = 1 \text{ m/s}$, $R = 0.025 \text{ m}$, and

$K = 1.3 \times 10^{-4} \text{ m}^2/\text{Vs}$ are shown with solid lines in figure 8. The time-of-flight to the plane of the aperture for each trajectory is $50 \times 10^{-3} \text{ s}$. Also shown in figure 8, with dashed lines, are ion trajectories assuming no electric field; the time-of-flight is again $50 \times 10^{-3} \text{ s}$. The surfaces that bound the trajectories with and without an electric field define volumes of charge that reach the aperture during the assumed time interval. Ignoring possible loss mechanisms in and below the plane of the aperture, the significance of the different volumes can be seen by examining the expression for measured ion density,

$$\rho_m = I/M, \quad (30)$$

where I is the ion current and M is the volumetric flow rate. Expressing I as charge per unit time, Q/t , and M as air volume per unit time, V/t ,

$$\rho_m = Q/V \quad (31)$$

The charge Q can be expressed as the product of average charge density, ρ_a , and volume, V' , occupied by the charge. Then,

$$\rho_m = \rho_a V'/V \quad (32)$$

When there is no electric field, the volume of charge that enters the aperture coincides with the volume of air ($V' = V$) and the measured charge density equals the average charge density in space. With an electric field, V' is greater than V and the measured charge density will exceed the average value in space and thus be in error.

As the air speed is increased, the difference between V' and V decreases and ρ_m approaches ρ_a . Figure 9 shows ion trajectories with and without an electric field for u_0 equal to 6 m/s. While the air speed may be unrealistically high for typical ion counter operation, the smaller difference between V' and V is apparent.

Figure 8. Ion trajectories for air speed of 1 m/s in plane of aperture. The solid curves show influence of 15 kV/m electric field. Dashed curves are for no electric field. The time-of-flight for all trajectories is 50 ms. The volume occupied by the ions that enter aperture when $E = 0, V'$, exceeds volume of air, V , which enters in the same time. Inset shows effect of mobility value on trajectory near aperture.

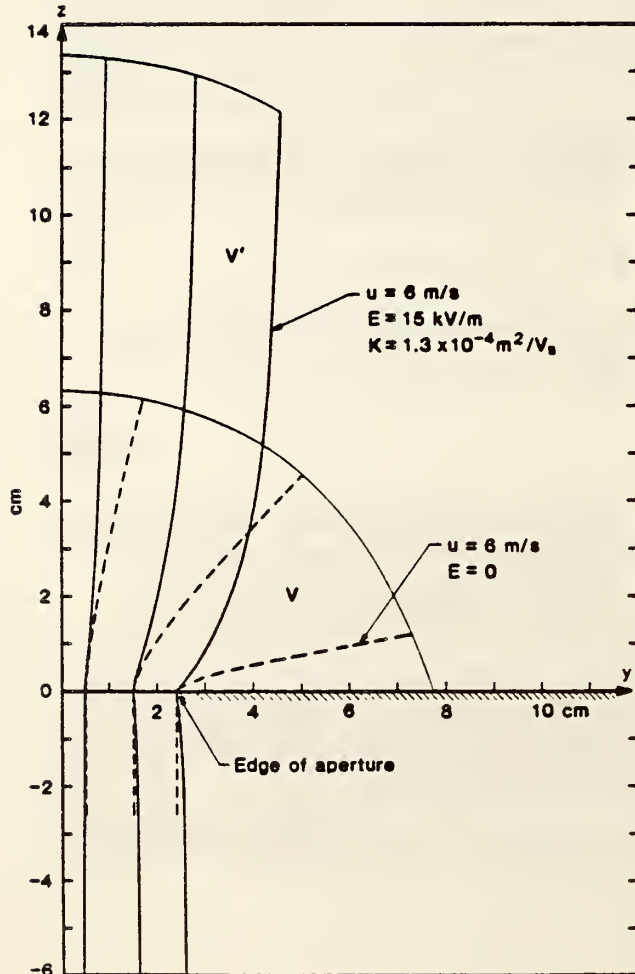
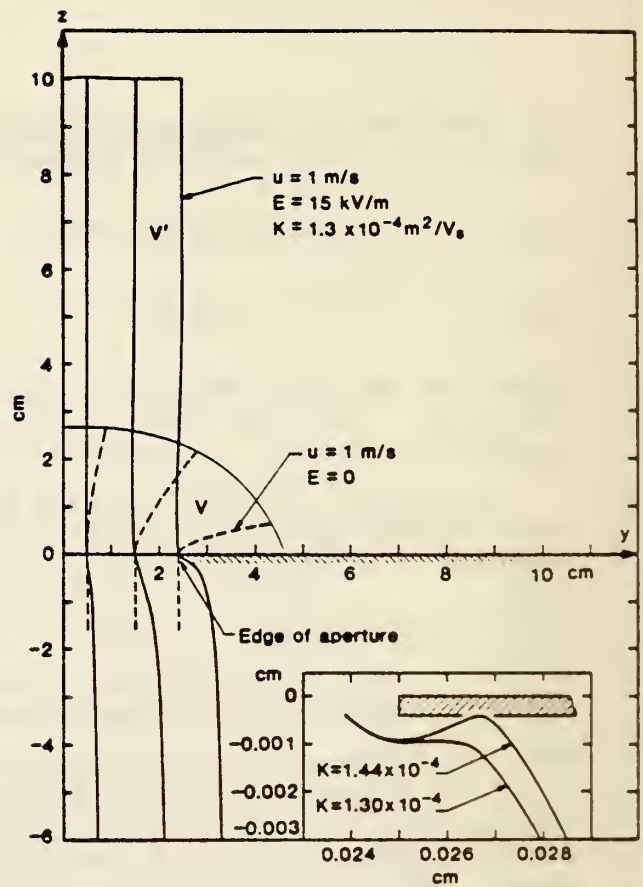


Figure 9. Ion trajectories for air speed in plane of aperture of 6 m/s. The solid curves show influence of 15 kV/m electric field. Dashed curves are for no electric field. The time-of-flight for all trajectories is 50 ms. The volume occupied by the ions that enter aperture when $E = 0, V'$, exceeds volume of air, V , which enters in the same time.

Losses in and below the plane of the aperture can occur because of ion trajectories which terminate near the edge of the aperture. For example, the inset in figure 8 suggests that some trajectories less than ≈ 1 mm from the edge of the aperture ($K = 1.3 \times 10^{-4} \text{ m}^2/\text{Vs}$) will not "clear" the aperture. This would represent approximately 8% of the ions that reach the aperture, assuming a uniform charge density across the aperture.

It should also be noted that most of the trajectory calculations in figure 8 have been performed for a single ion mobility value, $1.3 \times 10^{-4} \text{ m}^2/\text{Vs}$. A distribution of mobilities normally exists and ions with mobilities greater than $1.3 \times 10^{-4} \text{ m}^2/\text{Vs}$ could also fail to clear the aperture as shown in the inset of figure 8. Interestingly, if the product of mobility and electric field (drift velocity) is kept constant, the trajectory remains unchanged for a given air speed.

If a duct is introduced below the aperture, loss of ions will occur via collisions with the wall of the duct. Assuming for simplicity that the trajectories in figure 8 remain unaffected by the duct, calculations show that ions entering the aperture 5 mm from the edge ($y = 2$ cm) will collide with the duct about 1.3 cm below the plane of the aperture. This loss, as well as the loss of other ions passing through the aperture further from the z-axis, would amount to about 36% of the total number of ions reaching the aperture, again assuming that the ion density were uniform over the area of the aperture.

The excess ions entering an ion counter due to an external electric field which attracts ions to the ion counter and the ion losses which subsequently occur to the walls of the ion counter was noted by Swann early in this century [11]. He concluded that the ion current to the walls was just equal to the excess ion current due to the electric field, independent of air speed, and that the electric field did not influence the ion density measurement [12]. However, because Swann appears to assume that all the electric field lines terminate on the walls of the ion counter, his conclusion that all of the excess ion current goes to the walls must be qualified. Some field lines could terminate on the electrodes of the ion counter and contribute to a higher ion density measurement. For example, calculations show that field lines within a radius of 5 mm of the center of the aperture will travel at least 4.5 cm below the plane of the aperture before reaching an imaginary wall at a radius of 2.5 cm. Loss of ions due to Coulomb repulsion and other mechanisms will be treated later in a fuller account of the problems associated with operation of aspirator-type ion counters in the presence of an external electric field.

3.6 Summary

Progress has been made in characterizing an apparatus for producing a known unipolar ion density for calibration of aspirator-type ion counters operating in the ground plane in the presence of a large external electric field. The external field causes more ions to enter the opening of an ion counter than would occur in the absence of the field. Whether the extra ions cause a measurement error depends, in part, on whether any electric field lines terminate on the collecting electrodes of the ion counter. The percentage of extra ions arriving at the opening of the ion counter increases

as the air velocity decreases, for a given electric field strength. It is noted that the above results are true for ion counters operating in the ground plane and extension to cases where the ion counter is operated above the ground plane is not straightforward.

4. GASEOUS DIELECTRICS RESEARCH Task 03

Richard J. Van Brunt, Motaganahalli C. Siddagangappa, and Arthur V. Phelps
Electrosystems Division
National Bureau of Standards

4.1 Introduction

The objectives of this project are to develop measurement capabilities and to provide fundamental data as part of the Department of Energy's basic research concerned with the development and evaluation of advanced compressed-gas-insulation technology.

To reduce space requirements and improve the efficiency of high-voltage transmission systems, the electric power industry has turned toward more extensive use of compressed-gas insulation. To design meaningful tests of system performance and establish specifications for the quality of materials, more information is needed about the fundamental physical and chemical processes which lead to insulation deterioration and electrical breakdown. This research project is directed toward the evaluation of advanced measurement techniques as diagnostic tools of insulation performance; applications of gas chromatography-mass spectrometry to characterize corona byproducts; and the acquisition of fundamental data, e.g. corona inception voltages, production rates of corona byproducts, and the effects of contaminants on discharge initiation.

This report highlights four significant technical activities. The next section describes the determination of the influence of trace amounts of water vapor on electron avalanche growth. This is followed by a theoretical discussion of a technique for the common parameterization of swarm and breakdown data for binary gas mixtures. Experimental and theoretical results on corona-induced chemical decomposition are then discussed.

4.2 Influence of Trace Amounts of Water Vapor on Electron Avalanche Growth in SF₆

The work presented in this section has been described in detail in a paper [13] that has been accepted for publication in the Journal of Applied Physics, and therefore only a summary of the method, results, and conclusions is presented here. This work was also discussed in a paper presented at the 1985 38th Annual Gaseous Electronics Conference, in Monterey, California.

Measurements were made of the statistical size distributions and repetition rates of electron avalanches formed near a positive point electrode in a uv-irradiated point-plane gap containing pressurized SF₆ with varying, known, trace amounts of H₂O from about 10 to 300 parts-per-million by volume.

The method for measuring electron avalanche pulses is the same as described previously [14]. The gas chromatograph-mass spectrometer method of measuring the water vapor in SF₆ was developed as part of this project in the previous year and has been described in a recent publication [15]. The results obtained from the measurements verify the trends reported in an earlier preliminary work [16], namely that the introduction of trace amounts of H₂O into SF₆ has the effect of enhancing both the mean size and repetition rate of electron avalanches formed near a positive point electrode by an order of magnitude or more.

Examples of results obtained for the pulse height distributions and repetition rates for electron avalanches as a function of [H₂O] are displayed respectively in figure's 10a and 10b. Plotted in (fig. 10a) are the arbitrarily normalized relative numbers of avalanches that were recorded in a given time interval versus the avalanche size expressed in picocoulombs (1 pC is roughly equivalent to 6×10^6 electrons) for different indicated [H₂O] values and voltages applied across the gap. The vertical arrows in this figure mark the largest avalanches which were recorded for SF₆ at the indicated voltages for the least amount of water vapor content ([H₂O] = 14 ppm_v). The smallest avalanches observed, i.e., the low side cutoff points for each data set, were determined by the discriminator setting of the pulse detection system. Shown in (fig. 10b) are measured average avalanche count rates versus applied voltage for all avalanches in excess of 0.08 pC.

It is of interest to note in figure 10a that the avalanche size distributions exhibit a bimodal structure once a significant number of avalanches exceed the level of about 1.5 pC ($\sim 10^7$ electrons).

Theoretical calculations, the details of which will not be discussed here, were performed in an effort to understand both the basic, microscopic mechanisms by which avalanche size is increased by low concentrations of water vapor and the reasons for the development of bimodal distributions. The calculations of mean avalanche size, using computer codes previously developed as part of this project [17,18], demonstrated that it would be necessary for the ionization coefficient to increase by as much as three orders of magnitude to account for an order of magnitude increase in the mean avalanche size. With assistance from A. V. Phelps of the NBS Quantum Physics Division, calculations were made of the ionization and electron attachment coefficients for SF₆/H₂O mixtures using numerical solutions of the electron transport equation. In agreement with estimates based on the Wieland Approximation [19], the calculation showed that the introduction of 1% H₂O causes the ionization coefficient for SF₆ to drop by about 1% when the ratio of electric field-to-gas density is at the critical value where ionization growth is possible. It was therefore concluded that the avalanche enhancement effect of H₂O is not due to a change in the ionization rate of the gas.

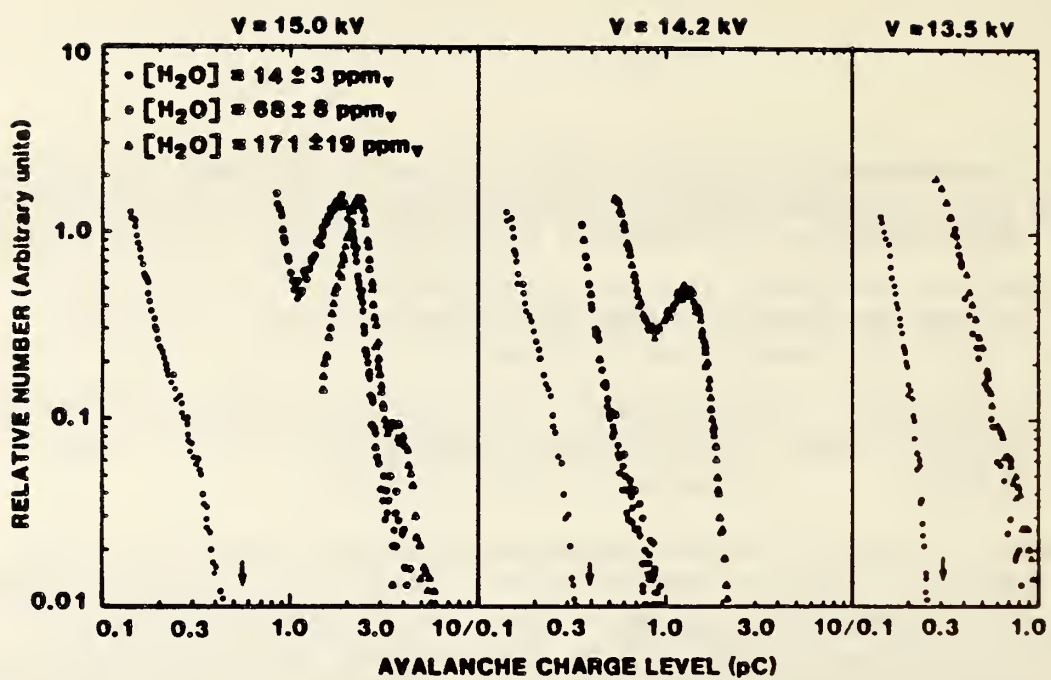


Figure 10a. Measured pulse height distributions for electron avalanches formed near a positive point electrode in SF_6 at a pressure of 200 kPa for the indicated different water vapor concentrations and applied voltages.

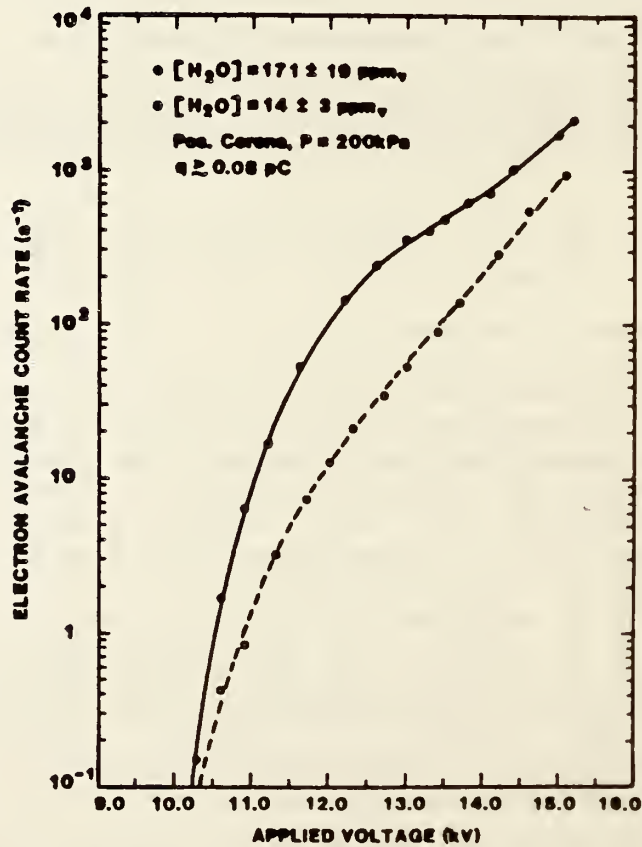


Figure 10b. Measured electron avalanche repetition rates versus applied voltage at the indicated water vapor concentrations for avalanches larger than 0.08 pC.

A more reasonable mechanism has been proposed [13] to account for the observed enhancement effect, which considers the appearance of minor negative ion charge carriers associated with water vapor such as the clusters $(H_2O)_n^-$, $OH^-(H_2O)_n$, $n = 1, 2, \dots$ that have a much lower energy threshold for collisional detachment than the expected predominant negative ions associated with SF_6 , e.g. $SF_6^-(H_2O)_n$. The more weakly bound negative ions, which are formed when enough H_2O is present, can experience electron detachment at much lower electric fields than the SF_6 -related ions and thereby can give rise to formation of larger avalanches at a higher rate.

This hypothesis is supported by theoretical calculations [13] which were performed of collisional detachment probabilities for negative ions having different detachment thresholds as a function of position in the critical initiation volume [17,18] near the point electrode surface. Examples of results from such calculations are displayed in figures 11a and 11b. Shown are computed probabilities for electron detachment per unit distance p'_d as a function of position in the critical volume for ions with different assumed detachment cross sections as indicated with different threshold energies ϵ_t .

Thresholds of 7 to 10 eV for collisional detachment of F^- and SF_6^- are consistent with other recent work [20-22]. It is seen that for lower thresholds of, for example, $\epsilon_t = 0.5$ eV, the value of p'_d increases by orders of magnitude over that for ions with $\epsilon_t = 7$ to 10 eV. This is more than sufficient to account for the observed avalanche enhancement effect.

An attempt has been made, using a computer model of electron avalanche growth statistics based on an extension of Legler's theory [23], to determine the theoretical shape of the avalanche size distributions and the conditions under which the distributions might become bimodal. It was found [13] that the modified Legler theory, which applies for nonuniform fields and which incorporates the statistics of initiating electron release through p'_d mentioned above, always predicts a monotonically decreasing probability with increasing number of electrons in the avalanche. This theory cannot, therefore, account for the development of bimodal distributions, and it is proposed that this behavior can only be predicted by a three dimensional model which properly includes the influence of ion and electron space charge.

4.3 Common Parameterizations of Swarm and Breakdown Data for Binary Gas Mixtures

The work described in this section was discussed both at the 1985 Joint Symposium on Swarm Studies and Inelastic Electron-Molecule Collisions, Tahoe City, California, and at the 1985 38th Annual Gaseous Electronics Conference, Monterey, California, and is now being prepared for archival publication. Again, only the main ideas are discussed here without detailed mathematical derivations.

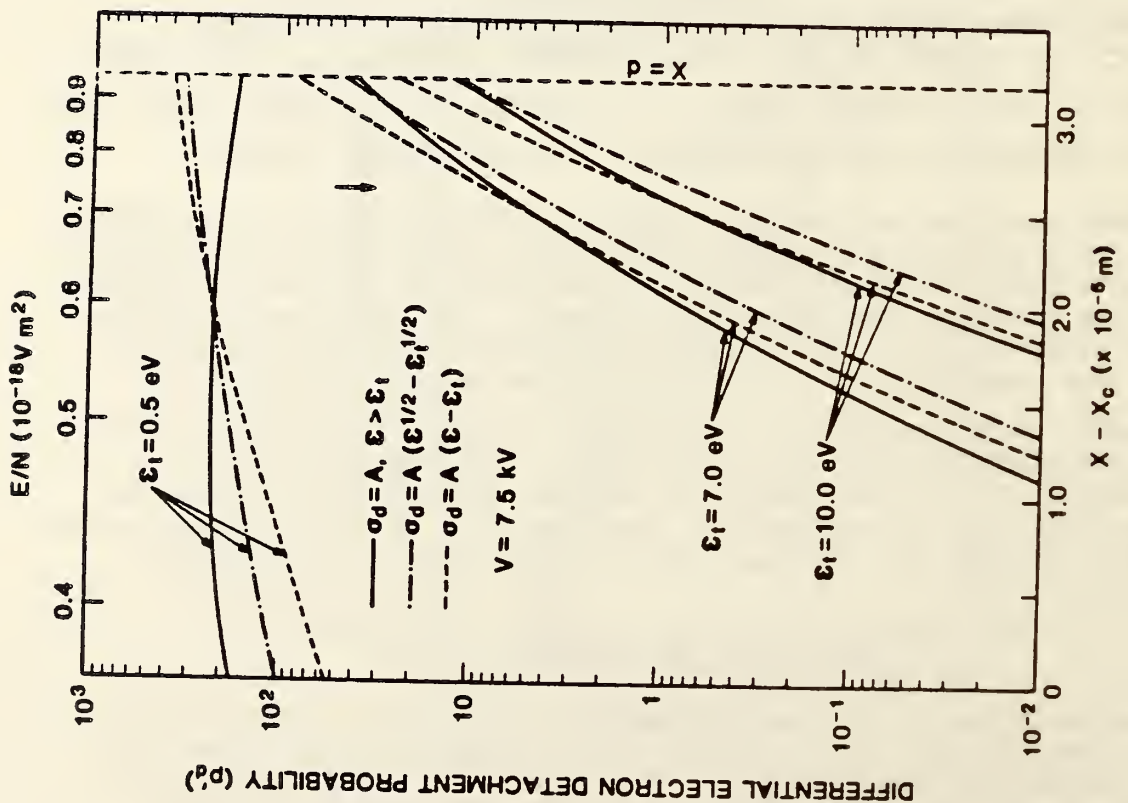
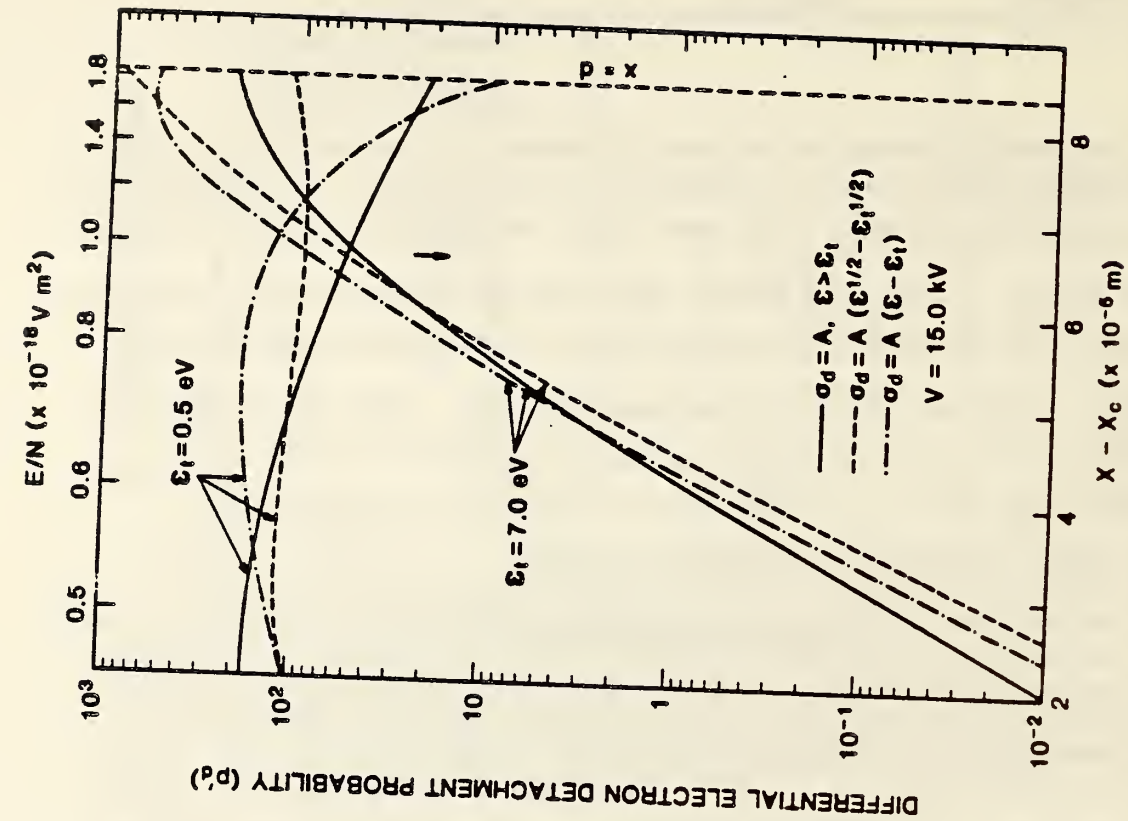


Figure 11. Calculated differential electron detachment probabilities versus location between the point electrode surface d and the point x_c at which the ionization and attachment coefficients for the gas are equal for two different applied voltages. The different lines designate different assumed energy dependences of the cross sections for collisional detachment of negative ions with different indicated detachment thresholds ϵ_t .

A theoretical model is proposed for use in fitting and analyzing data on electrical breakdown in binary, electronegative gas mixtures which makes use of available cross section and electron swarm data for the individual components of the mixture. The model affords more physical insight and allows more flexibility in fitting data than the simple Wieland Approximation [19]. It was shown that the model is useful in resolving controversies or disagreements in results and in determining whether or not data are physically reasonable. It also permits examination of the conditions under which pressure dependent (or independent) synergistic effects are possible.

Three basic assumptions are required in the model when pressure dependent effects are neglected. (Pressure dependence will be considered later.) These assumptions are: 1) the electron kinetic energy distributions in the gas are Maxwellian under all conditions, i.e.

$$F_{\gamma}(\varepsilon) = (2/\pi^{1/2})\lambda_{\gamma}^{3/2}\varepsilon^{1/2}\exp(-\lambda_{\gamma}\varepsilon), \quad (33)$$

where ε is the electron kinetic energy and $\gamma = 1, 2$, m designate the two individual gas constituents A and B and the mixture respectively; 2) the electron temperature ($T_{\gamma} = 1/k\lambda_{\gamma}$, $k =$ Boltzmann's constant) for the mixture is given by a weighted sum of the temperatures for the individual components, i.e.

$$T_m = q(F)T_1 + (1 - q(F))T_2, \quad (34)$$

where for $1 \rightarrow A$ and $2 \rightarrow B$,

$$F = [A]/([A] + [B]), \quad 1 \geq F \geq 0, \quad (35)$$

and

$$q(1) = 1, \quad q(0) = 0, \quad q(F) > 0; \quad (36)$$

3) the variables F and E/N (field-to-gas density ratio) are separable so that the ionization (α) and attachment (η) coefficients for the mixture can be represented again as weighted sums respectively given by

$$\alpha_m = h(F)\alpha_1(E/N) + (1 - h(F))\alpha_2(E/N), \quad (37)$$

and

$$\eta_m = g(F)\eta_1(E/N) + (1 - g(F))\eta_2(E/N), \quad (38)$$

where the functions $h(F)$ and $g(F)$ satisfy the same conditions as $q(F)$. It should be noted that in assumption 2 above, one could equivalently take an identical linear combination of the mean electron energies.

A computer program was written to find least squares fits to measured critical electric field-to-gas density ratios $(E/N)_{c,m}$ using the proposed model. The values of $(E/N)_{c,m}$ correspond to the condition,

$$\alpha_m = \eta_m, \quad (39)$$

at which ionization growth, and therefore electrical breakdown in the gas mixture, is possible. The adjustable parameters for fitting are the electron temperatures T_1 and T_2 for the two gas components (or equivalently λ_1 and λ_2). These temperatures are adjusted within reasonable limits and α_m and η_m are computed using the expressions

$$g(F) = \frac{-\lambda_2 H_{22} S_{m2} + \lambda_m (S_{m1} F + S_{m2} (1-F)) (H_{m1} F + H_{m2} (1-F))}{\lambda_1 S_{m1} H_{11} - \lambda_2 S_{m2} H_{22}}, \quad (40)$$

and

$$h(F) = \frac{-\lambda_2 I_{22} S_{m2} + \lambda_m (S_{m1} F + S_{m2} (1-F)) (I_{m1} F + I_{m2} (1-F))}{\lambda_1 S_{m1} I_{11} - \lambda_2 S_{m2} I_{22}}, \quad (41)$$

where

$$S_{m\beta} = \lambda^2 \int_0^\infty \epsilon \sigma_{m\beta}^{-1}(\epsilon) e^{-\lambda \beta \epsilon} d\epsilon, \quad (42)$$

$$I_{\alpha\beta} = \int_{\epsilon_i}^\infty \epsilon \sigma_{i\beta}(\epsilon) e^{-\lambda \alpha \epsilon} d\epsilon, \quad (43)$$

$$H_{\alpha\beta} = \int_0^\infty \epsilon \sigma_{a\beta}(\epsilon) e^{-\lambda \alpha \epsilon} d\epsilon, \quad (44)$$

$$\lambda_m = \lambda_m(q(F)), \text{ and} \quad (45)$$

$$\alpha, \beta = 1, 2, m. \quad (46)$$

These expressions are derived from the basic assumptions, and definitions of the ionization and attachment coefficients using the electron collision cross sections $\sigma_{m\beta}$, $\sigma_{a\beta}$, and $\sigma_{i\beta}$ for momentum transfer, electron attachment, and ionization respectively (ϵ_i = ionization potential). The $(E/N)_{c,m}$ values are computed from the requirement of eq (39) and compared with experimental data.

Examples of cases to which this fitting procedure have been applied are shown in (figs. 12a and 12b) respectively for the mixtures SF_6/N_2 and CCl_2F_2/N_2 for which there exist disagreements among the various measured and calculated $(E/N)_{c,m}$ values. Indicated in those figures are the energies ϵ_{max} corresponding to the peaks in the Maxwellian distributions for N_2 and the electron temperature ratios that gave the best fits. In figure 12a, the upper solid curve is a fit to the normalized experimental data of Siddagangappa, et al. [24] which shows a high degree of synergism, and the lower solid curve is

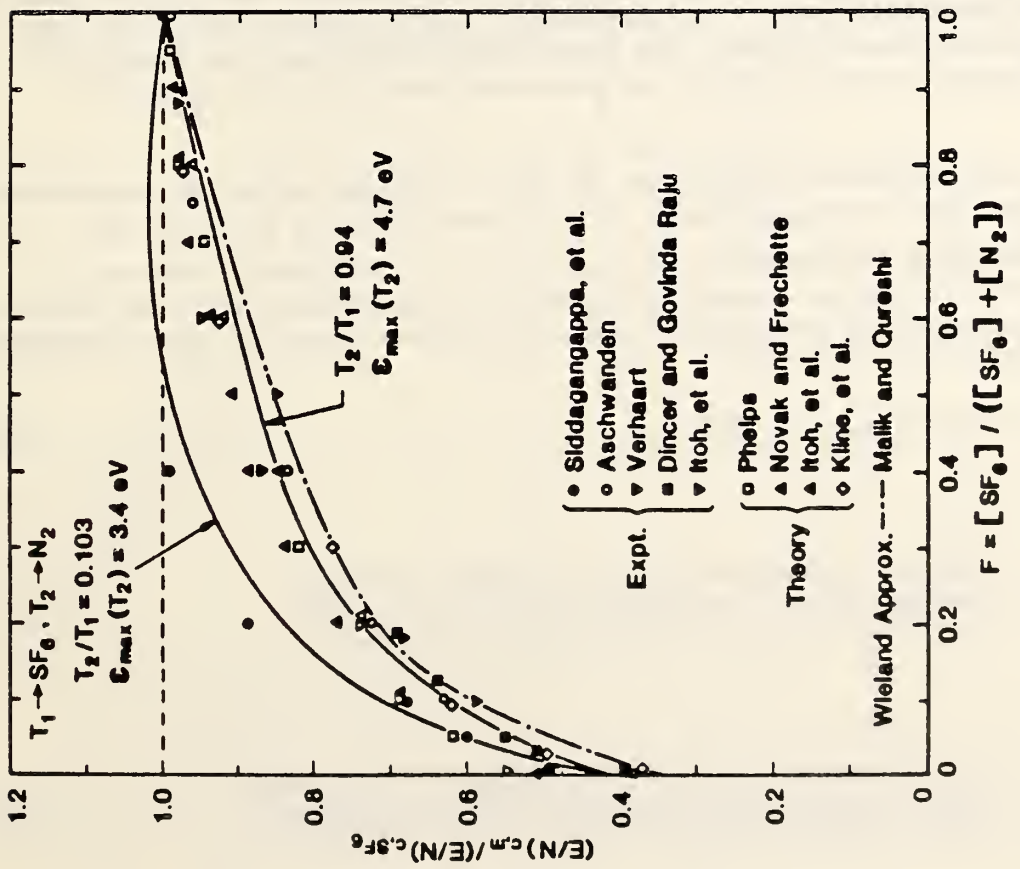
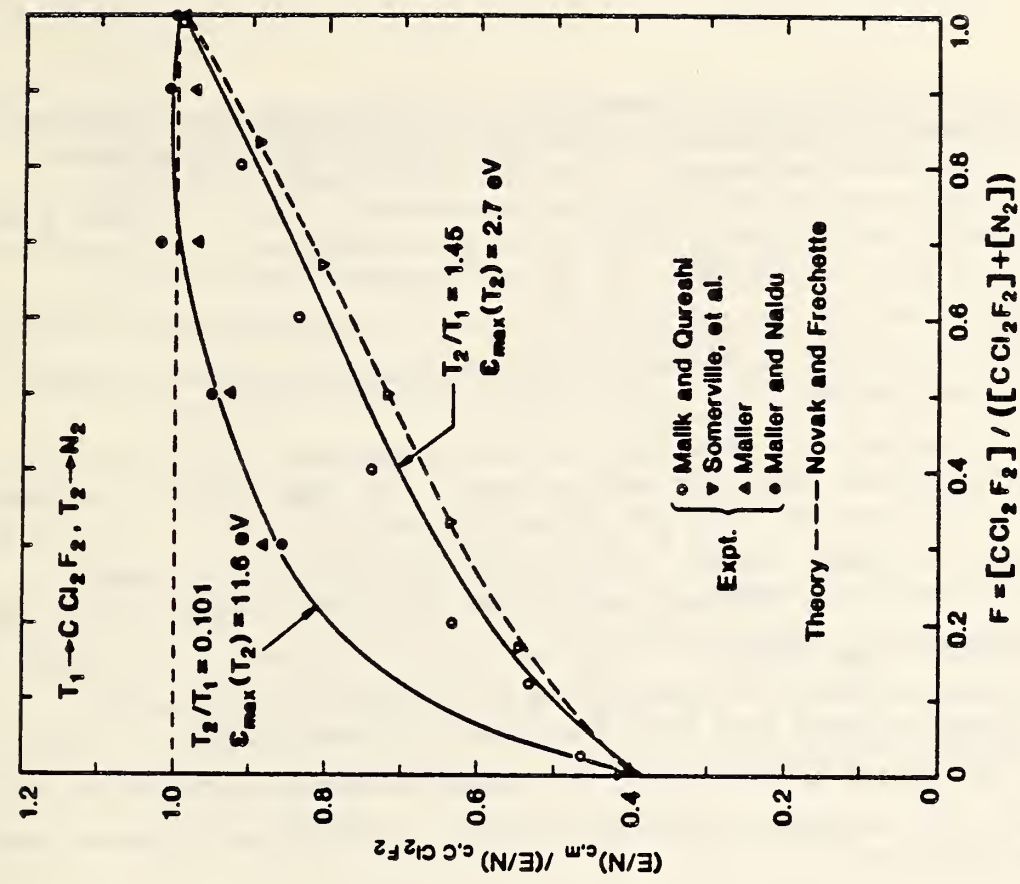


Figure 12. Fits (solid lines) to normalized critical field-to-gas density ratios for the mixtures SF_6/N_2 and CCl_2F_2/N_2 .

a fit to the normalized data of Aschwanden [25] which shows less synergistic behavior and is more in agreement with the results of other measurements [26-28], and theoretical Boltzmann [29-32] and Monte Carlo [33] type calculations. The significant point to be made here is that to obtain a high degree of synergism as implied by the data of Siddagangappa, it is necessary that T_1 and T_2 be quite different, i.e. by approximately an order of magnitude. The values for T_1 and T_2 from the fit to the Aschwanden data are nearly the same, consistent with temperatures estimated from the Boltzmann calculations. The condition $T_1 = T_2$ is sufficient for the Wieland Approximation to apply [19], and indeed this approximation [34] is seen to satisfactorily represent the lower sets of data. The same behavior is found for the fits to the data for CCl_2F_2/N_2 shown in (fig. 3b) [35]. A fit to the data exhibiting the highest degree of synergism again requires a large difference in the electron temperatures for the individual components N_2 and CCl_2F_2 ; in this case ϵ_{\max} for N_2 is also unrealistically high. In general, it can be stated that in order for there to be a high degree of pressure independent synergism, such as a positive synergism where $(E/N)_{c,m} > (E/N)_{c,1}$ and $(E/N)_{c,2}$, there must be a shift in the electron energy distribution with F so as to enhance the attachment rate in the gas. In the model proposed here, this requires that $T_1 \neq T_2$.

To account for pressure dependent synergistic behavior, one must consider three-body electron stabilization processes as pointed out in a recent work of Hunter and Christophorou [36]. In particular, for a binary, molecular gas mixture designated here by AX/BY, one must consider the various possible negative ion formation and destruction processes such as are included in table 2.

The reactions that are underlined in this table are electron detachment processes. The model discussed above for fitting $(E/N)_{c,m}$ data can be extended to include pressure dependent effects. In this case, however, a separation of the variables F and E/N is no longer possible, and one obtains the following complicated forms involving the various reaction rate constants given in table 2:

$$\eta_m = G_1(N, F)\eta_1 + G_2(N, F)\eta_2, \quad (47)$$

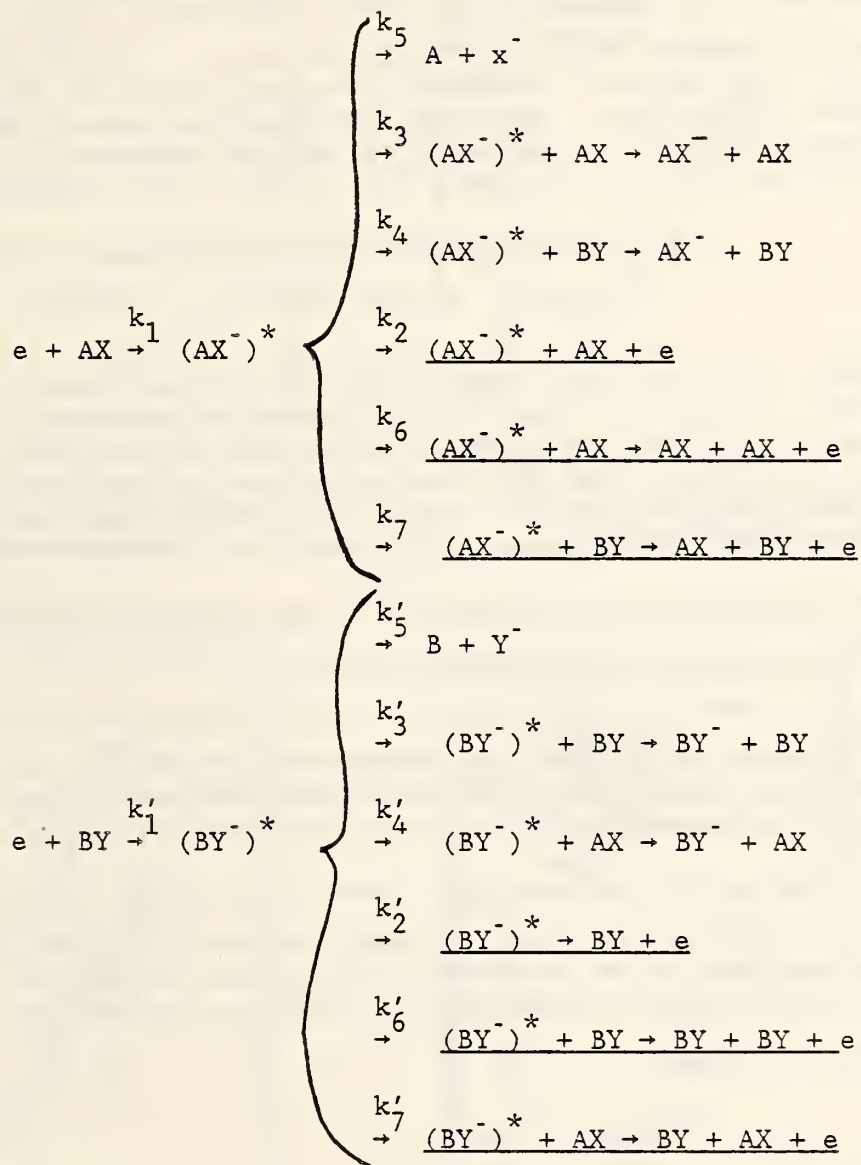
where

$$G_1 = \frac{g(F)(k_2+k_7(1-F)N+k_5+k_3FN)(k_5+FNk_3+(1-F)Nk_4)}{(k_5+FNk_3)[(k_4+k_7)(1-F)N+(k_3+k_6)NF+k_2+k_5]}, \quad (48)$$

and

$$G_2 = \frac{(1-g(F))(k'_2+k'_3(1-F)N+k'_5+k'_7FN)(k'_5+(1-F)Nk'_4+FNk'_4)}{(k'_5+(1-F)Nk'_3)[(k'_3+k'_6)(1-F)N+(k'_4+k'_7)NF+k'_2+k'_5]} \quad (49)$$

Table 2. Possible negative ion formation and destruction processes in binary, molecular gas mixture



It is of significance to note that if electron detachment processes are unimportant, so that one can set all the rate constants for the detachment processes equal to zero, then one simply obtains $G_1 = g(F)$ and $G_2 = 1 - g(F)$, i.e. eq (47) reverts back to the form of eq (38). It can be concluded, therefore, that pressure dependent synergistic behavior occurs only if detachment is important. When pressure dependent synergisms do occur, they are a consequence of the influence of one gas component on enhancing, or reducing, the electron detachment rate of the other component.

4.4 Corona-Induced Decomposition Rates of SF₆ in SF₆/N₂, SF₆/Ne, and SF₆/O₂ Mixtures

Some of the results of this work have been published in a recent archival paper [15], presented at the 1985 Gas Discharge Conference in Oxford, England [37], and at the 1985 38th Annual Gaseous Electronics Conference in Monterey, California, and have been submitted for presentation at the forthcoming 1986 IEEE International Symposium on Electrical Insulation. Only selected significant features of this work are reviewed here.

The charge rates of production for the gaseous oxygenated species SOF₂, SO₂F₂, SOF₄, and SO₂ were measured in mixtures of SF₆ with N₂, with O₂, and with Ne as a function of SF₆ content for a continuous, 40-μA, dc, negative, corona discharge at a total gas pressure of 200 kPa (~2 atm). Examples of data from which production rates were determined are shown in figures 13 and 14. The experimental method has been described previously [15].

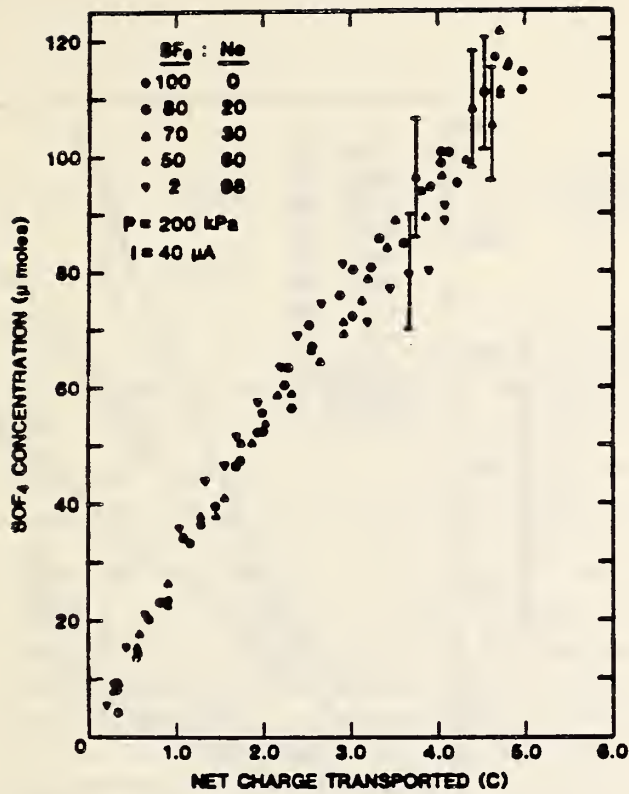
The maximum SF₆ decomposition rates in a corona discharge for the mixtures of interest were computed and compared with total observed rates given by the sums of the measured rates for all oxygenated products. The maximum charge-rates-of-production r_q which are related to the time rates of production, dc/dt , by

$$r_q = i^{-1}(dc/dt), \quad (50)$$

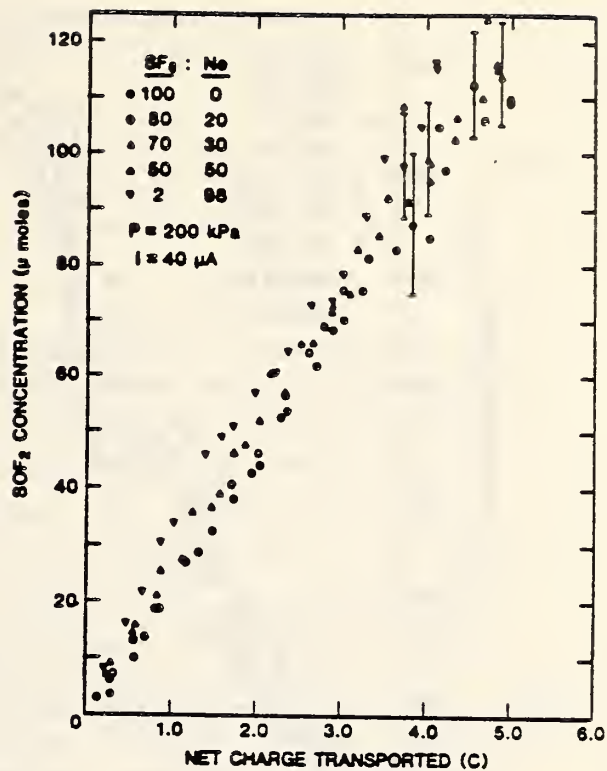
where i is the discharge current, were computed using the expression [15]

$$r_q = \frac{k_{ex} P \ell}{evkT} \left(\frac{1}{N_A} \right), \quad (51)$$

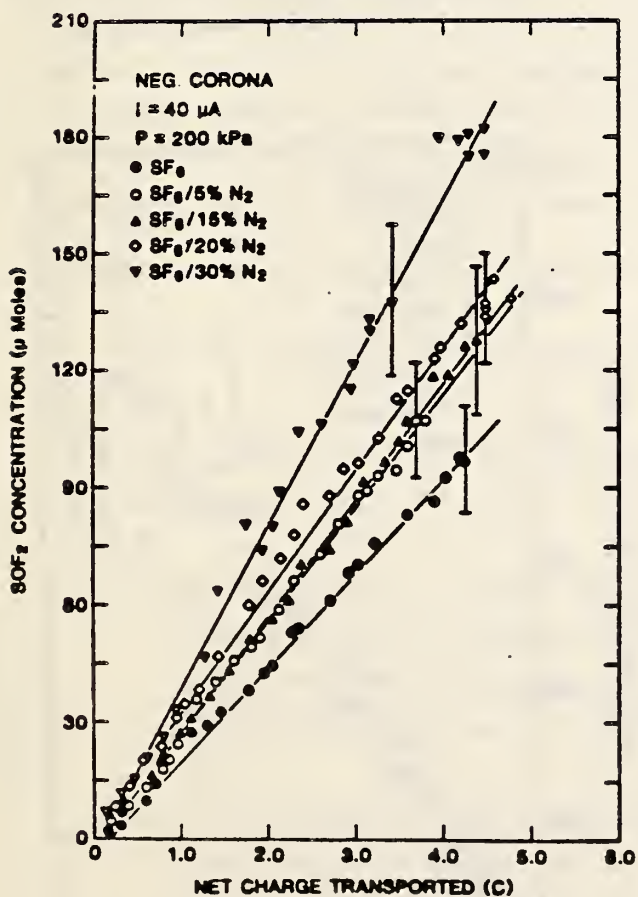
where k_{ex} , P , ℓ , e , v , k , T , N_A are the SF₆ dissociation rate constant, partial pressure of SF₆, the mean path traveled by an electron in the gas (approximately the radius of the active discharge volume), electronic charge, electron drift velocity, Boltzmann's constant, gas temperature, and Avagadro's constant respectively. The SF₆ dissociation rate is given by



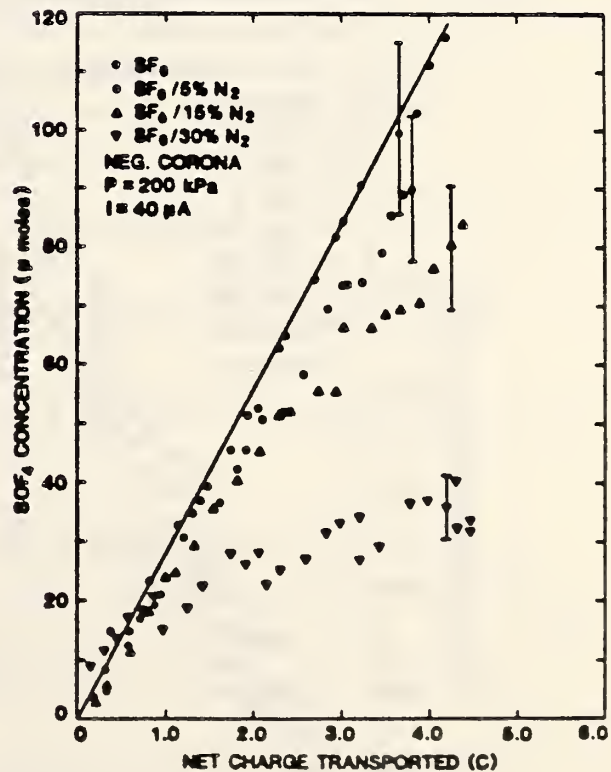
a)



b)

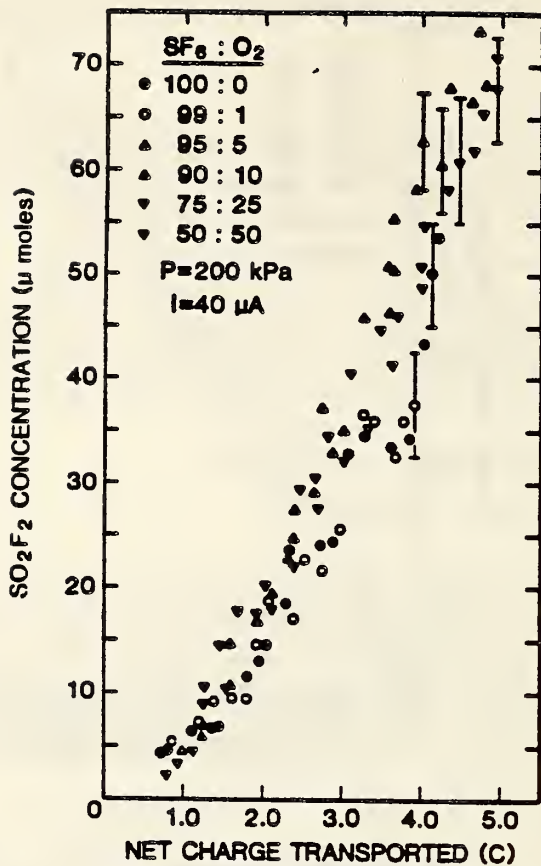


c)

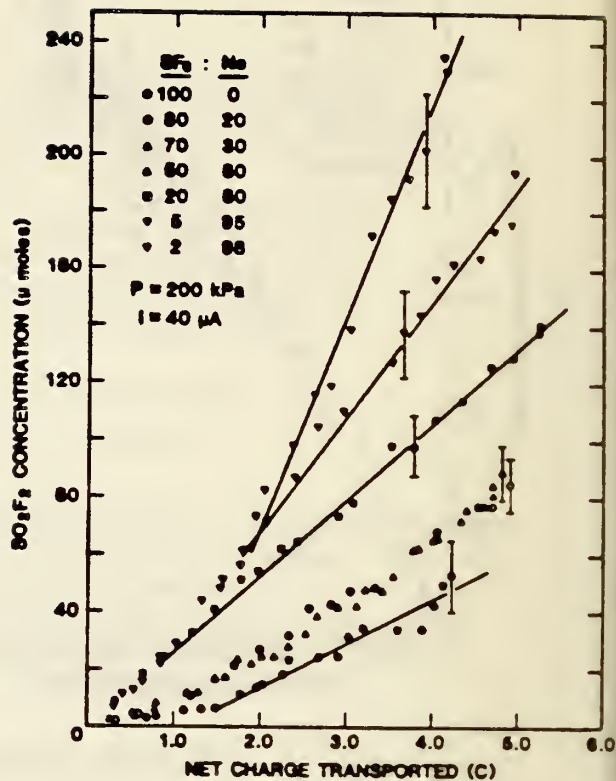


d)

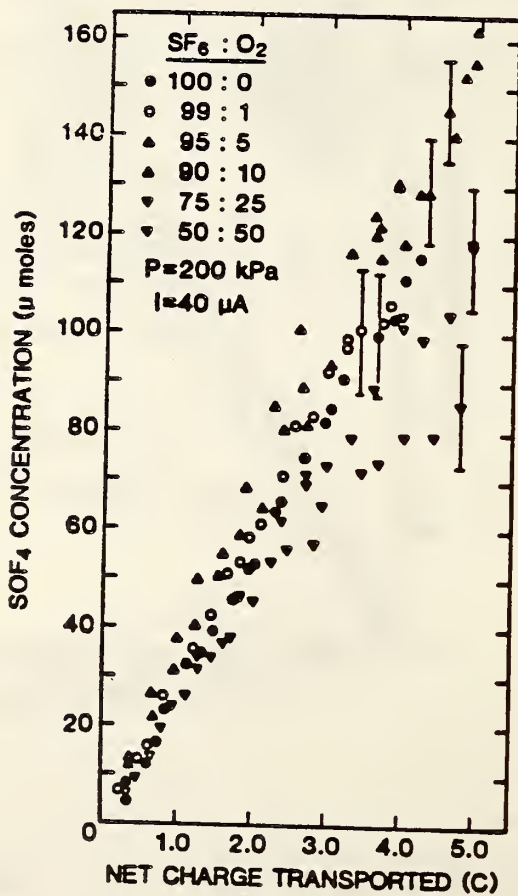
Figure 13. Examples of data on measured oxyfluoride concentrations versus net charge transported in the corona discharge for different indicated SF₆/Ne and SF₆/N₂ mixtures from which production rates were determined.



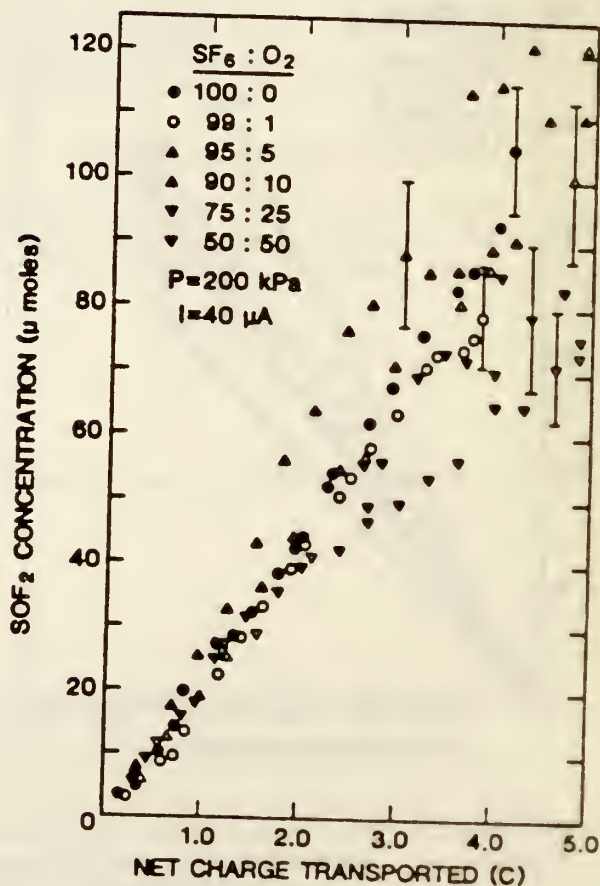
a)



b)



c)



d)

Figure 14. Examples of data on measured oxyfluoride concentrations versus net charge transported in the corona discharge for different indicated SF_6/Ne and SF_6/O_2 mixtures from which production rates were determined.

$$k_{ex} = \sum_i \int_0^\infty \epsilon^{1/2} f(\epsilon) Q_{xi}(\epsilon) d\epsilon \quad (52)$$

at $E/N = (E/N)_c$ ($\alpha = \eta$).

In eq (52), $f(\epsilon)$ is the electron energy distribution which was computed for each mixture using numerical solutions of the Boltzmann transport equation by the method previously described [38]. The quantities $Q_{xi}(\epsilon)$ are the cross sections for electronic excitation of SF_6 by electron impact which were assumed to coincide with dissociation processes. The complete set of SF_6 electron collision cross sections used in the calculations of k_{ex} are shown in figure 15. Consistent with recent arguments [39], it is assumed that the chemically active region of the corona discharge has a uniform E/N close to the critical value. The size l of the active volume was estimated photographically by measuring the width of the small uniformly luminous region of the discharge near the point electrode surface. Figure 7 shows examples of the measured SF_6 -normalized ($r_q/[SF_6]$) production rates for the individual products observed in the different mixtures as well as comparisons of the measured total SF_6 -normalized decomposition rates with the theoretical maximum values. Indicated also are maximum decomposition rates determined by including possible maximum contributions to SF_6 dissociation from metastable excitation transfer in N_2 and Ne. This contribution is unlikely to be important for SF_6/N_2 because there is experimental evidence that the predominant $A^3\Sigma_u^+$ metastable state of N_2 is not quenched by SF_6 [40].

Several important conclusions have been derived from this work. These include:

- 1) In "pure" SF_6 , the discharge dissociation products predominantly recombine back into SF_6 .
- 2) The decomposition rates for SF_6 increase and approach the maximum values as the SF_6 content decreases. This behavior indicates that the primary effect of diluting the SF_6 gas with N_2 , Ne, or O_2 is a reduction in the rate of recombination of SF_6 dissociation fragments.
- 3) The appearance of SO_2 in SF_6/N_2 and SF_6/Ne at low SF_6 concentrations indicates that inhibition of SF_6 recombination by dilution enhances multistep electron-impact dissociation processes since SO_2 can only be formed from the smaller fragments S or SF which are only efficiently produced by multiple electron collisions.

ELECTRON - SF₆ CROSS SECTIONS

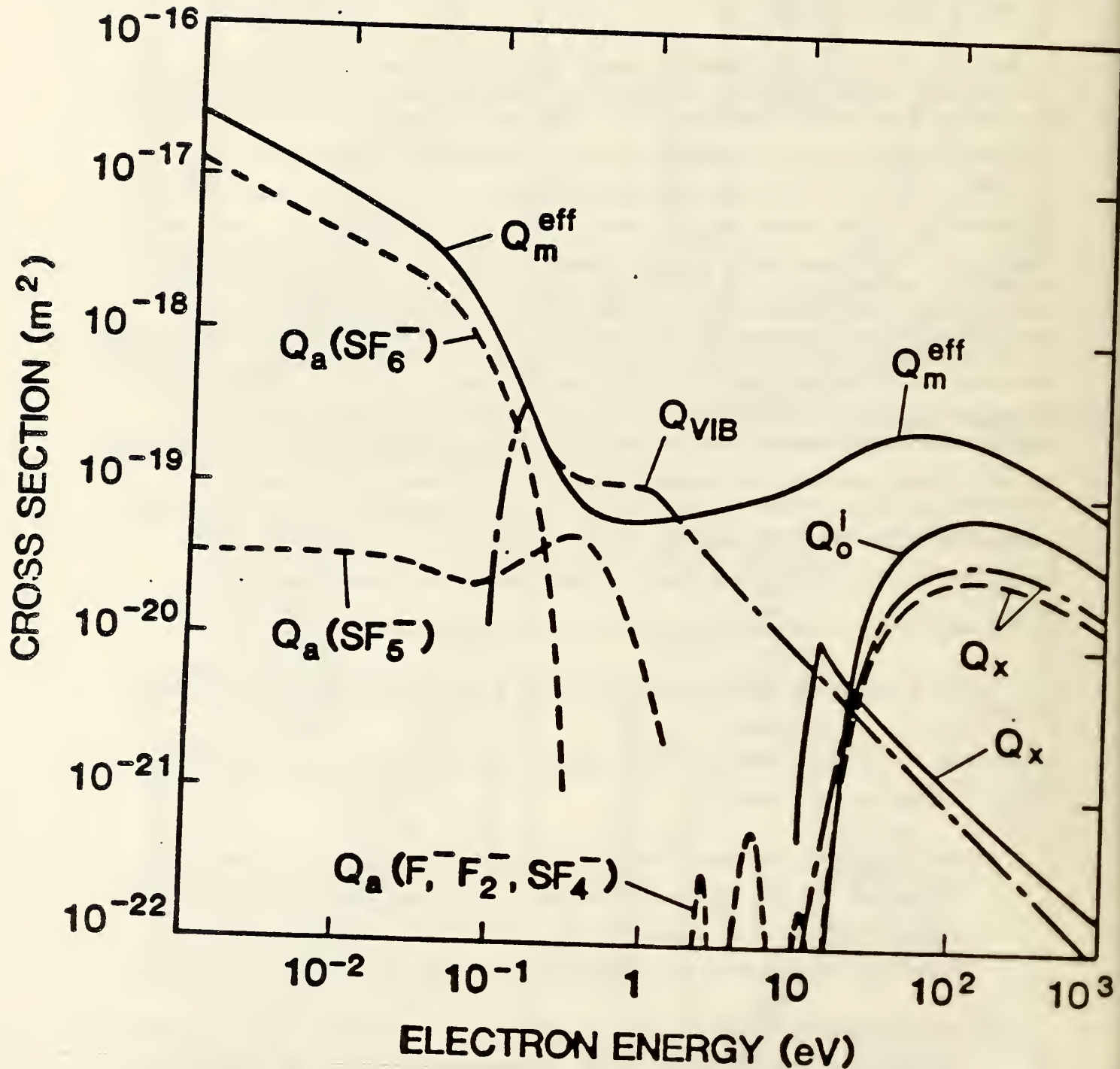
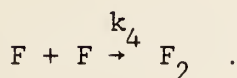
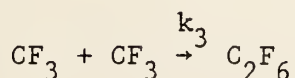
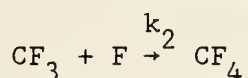
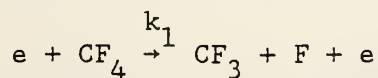


Figure 15. The complete set of electron collision cross sections for SF₆ used to calculate electron-induced dissociation rates of SF₆ in the mixtures SF₆/N₂, SF₆/O₂, SF₆/H₂O, and SF₆/Ne from numerical solutions of the electron transport equation. The attachment, ionization, momentum transfer, vibrational excitation, and electronic excitation cross sections are respectively denoted by Q_a, Q_oⁱ, Q_m^{eff}, Q_{VIB}, and Q_x.

- 4) The lack of SO_2 and the appearance of S^- deposition on the anode in SF_6/O_2 mixtures suggest formation of S^- by a rapid charge transfer process, possibly involving O_2^- , which prevents SO_2 formation by removing S atoms from the discharge region.
- 5) In all SF_6/N_2 mixtures, nitrogen oxide yield was small compared to oxyfluoride yield. This indicates that the gas decomposition is predominantly associated with SF_6 even in very dilute mixtures.
- 6) There was no evidence of nitrogen fluoride formation in SF_6/N_2 mixtures in 40- μA discharges. Evidence of trace amounts of NF_3 was found in $\text{SF}_6/98\% \text{N}_2$ mixtures subjected to discharges with currents greater than 100 μA for long periods (more than 20 h).
- 7) For SF_6/O_2 mixtures, CO_2 formation was observed and the behavior of its production with time and with O_2 content suggests that it is formed from reactions of O_2 with carbon on the point electrode surface.

4.5. Models for Decomposition of Gases in Corona Discharges

This work is preliminary and has not yet been discussed at a technical conference. The proposed chemical kinetics models have general applicability to decomposition of high pressure gases in cool glow or corona type discharges and provide insight into certain observed features of decomposition such as dependences on discharge current and gas composition. A few examples of how the model can be applied are considered here. A relatively simple example which has recently been considered is the decomposition of CF_4 in a corona discharge. I. Sauers [41] reported that the primary product of corona chemistry in CF_4 is C_2F_6 , and the time-rate-of-production is proportional to the discharge current, i.e. the charge-rate-of-production is constant. A simplified reaction scheme which applies in this case is:



The following assumptions are now made: 1) C_2F_6 is always at trace levels, i.e. $[CF_4] \gg [C_2F_6]$; 2) steady state conditions exist, i.e. $d[CF_3]/dt = d[F]/dt = 0$; 3) recombination predominates, i.e. $k_2 \gg k_3, k_4$. The relevant rate equations are:

$$\frac{d[CF_3]}{dt} = k_1 n_e [CF_4] - k_2 [CF_3][F] - k_3 [CF_3]^2 \quad (53)$$

$$\frac{d[F]}{dt} = k_1 n_e [CF_4] - k_4 [F]^2 - k_2 [CF_3][F] \quad (54)$$

$$\frac{d[C_2F_6]}{dt} = k_3 [CF_3]^2, \quad (55)$$

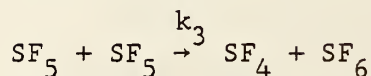
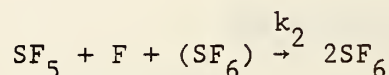
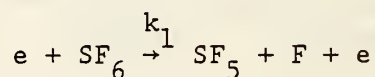
where n_e is the electron density, assumed to be proportional to the current. Because recombination predominates, one can take $[F] \sim [CF_3]$, which when used in eqs (53-55) with the above assumptions gives

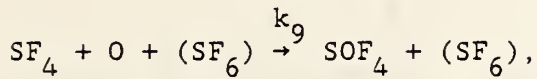
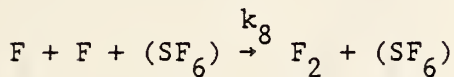
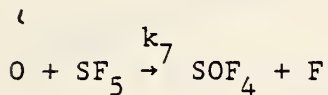
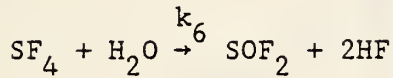
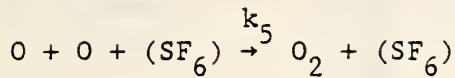
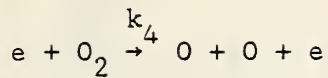
$$\frac{d[C_2F_6]}{dt} \approx \frac{k_3 k_1}{k_2} n_e [CF_4], \quad (56)$$

thus indicating that the C_2F_6 production rate is indeed proportional to current.

The model has been applied to corona-induced decomposition of SF_6 containing small quantities of H_2O and O_2 . Although in this case the reaction scheme is much more complicated, one can, using assumptions like those used for CF_4 , obtain reasonable qualitative descriptions of the dependences of oxyfluoride (SOF_2 , SO_2F_2 , and SOF_4) production on the concentrations $[H_2O]$ and $[O_2]$, and the discharge current which are consistent with experimental observations [15].

For production of SOF_2 and SOF_4 , which is in general competitive, one can consider a restricted set of reactions:





where the possible three body nature of some reactions has been indicated. The localized nature of the corona discharge must be considered in this case where hydrolysis of SF_4 (of rate k_6) is assumed to take place throughout the entire gas cell, whereas the other reactions involving SF_4 take place in the highly restricted volume of the discharge. Therefore, it is necessary to introduce the rate $k_s[SF_4]$ at which SF_4 escapes the discharge volume. The value of the effective rate constant, k_s , can be determined from solutions of the diffusion equation for SF_4 which apply under steady-state conditions.

It will be assumed that steady state conditions apply and that recombination of O , SF_5 and F back into O_2 and SF_6 predominate. The predominance of recombination in relatively pure SF_6 is indicated by the data shown in figure 16 which, from comparison with the computed maximum decomposition rates, shows that less than 3% of the dissociated SF_6 converts to oxygenated by-products. The results of solving the appropriate set of rate equations are:

$$\frac{d[SOF_2]}{dt} = \frac{k_s k_3 K n_e}{k_s + k_9 \left(\frac{k_4}{k_5} [O_2] [SF_6] \right)^{1/2} n_e^{1/2}} \quad (57)$$

and

$$\frac{d[\text{SOF}_4]}{dt} = \left(\frac{K k_4 [\text{O}_2]}{k_5 [\text{SF}_6]} \right)^{1/2} \left\{ k_7 n_e + \frac{K^{1/2} [\text{SF}_6] n_e^{3/2}}{k_S + k_9 \left(\frac{k_4}{k_5} [\text{O}_2] [\text{SF}_6] \right)^{1/2} n_e^{1/2}} \right\}, \quad (58)$$

with

$$K = \frac{k_1}{k_2 + k_8}. \quad (59)$$

The current dependences of the charge-rates-of-production for these species, as implied by eqs (58) and (59), are:

$$r_q(\text{SOF}_2) = a_1 / (a_2 + a_3 i^{1/2}), \quad (60)$$

and

$$r_q(\text{SOF}_4) = b_1 + \frac{b_2 i^{1/2}}{(b_3 + b_4 i^{1/2})}, \quad (61)$$

where a_i , b_i , $i = 1, 2, 3, 4$ are constants. This model then indicates that SOF_2 and SOF_4 production rates will respectively decrease and increase with increasing current, consistent with observations [15]. Neither rate depends on $[\text{H}_2\text{O}]$, which is again consistent with observations, and both have a weak dependence on $[\text{O}_2]$, with SOF_4 increasing and SOF_2 decreasing with increasing $[\text{O}_2]$. Although this latter behavior appears to be qualitatively consistent with previous results for SF_6/O_2 [15,37], and the data shown in (fig. 16), it obviously does not apply at high oxygen concentrations (above 30%) and the failure of SOF_4 production to change significantly with O_2 suggests that the oxygen for its formation can come from another source. This question deserves further consideration.

The production rate of SO_2F_2 , which is postulated to require molecular oxygen for its formation via reactions involving the lower valence fragments SF_2 and SF_3 , can also be predicted with this model. In this case, one obtains

$$r_q(\text{SO}_2\text{F}_2) = C_1 [\text{O}_2] / (C_2 [\text{O}_2] + C_3 i^{1/2}), \quad (62)$$

where C_i , $i = 1, 2, 3$ are constants. Again one finds a weak dependence on both $[\text{O}_2]$ and i consistent with observations. It should be noted that, in the present model, formation of SO_2F_2 does not compete with either SOF_2 or SOF_4 formation.

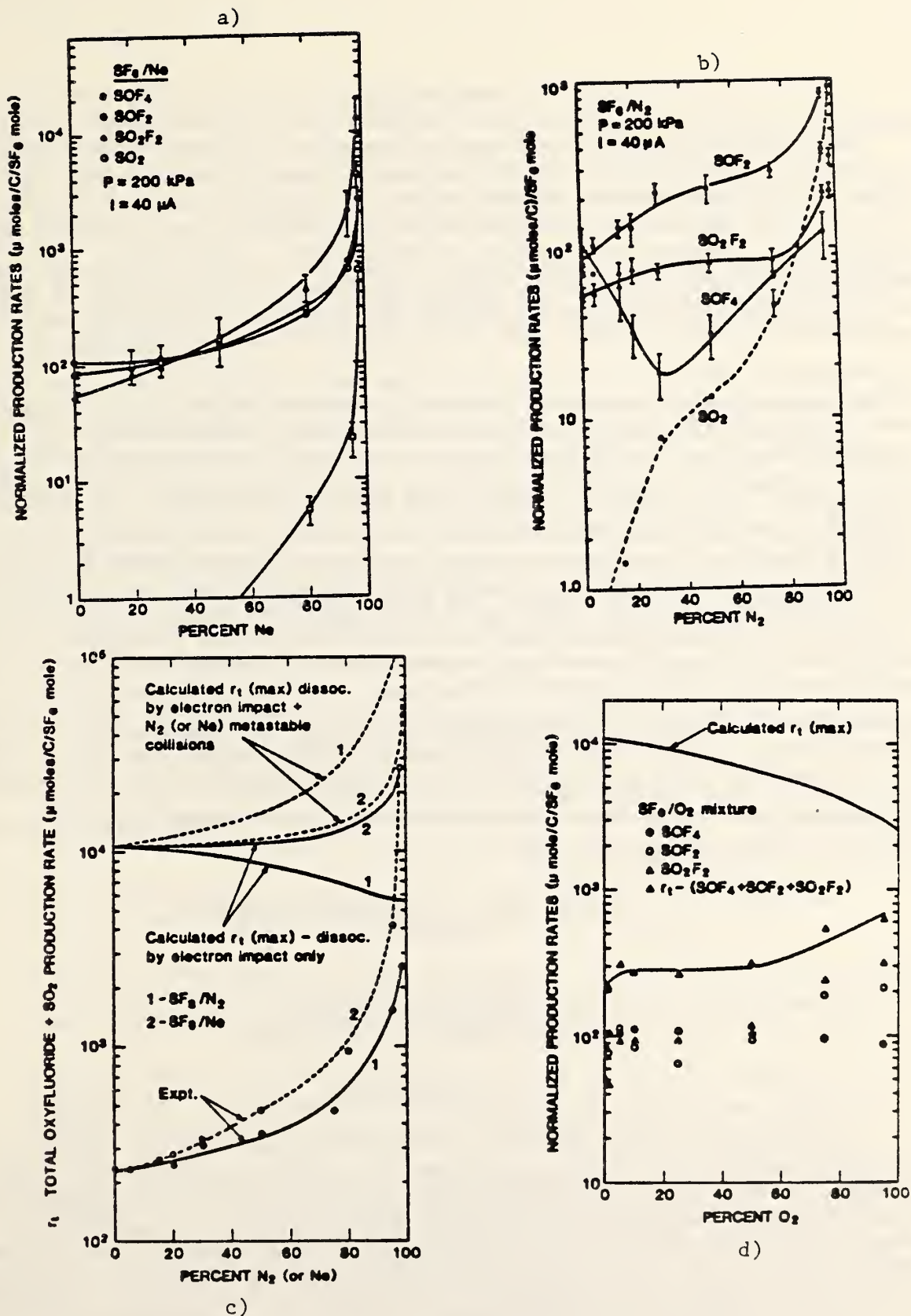


Figure 16. Measured charge rates-of-production for the oxyfluorides and SO₂ normalized to the SF₆ concentration versus percent concentration of N₂, O₂, and Ne in the mixtures SF₆/N₂, SF₆/O₂, and SF₆/Ne. Also shown are total oxyfluoride plus SO₂ rates (r_t) in comparison with the predicted upper limits for the total rates for SF₆ decomposition.

4.6 Summary

This report highlights the results from four significant technical activities associated with the NBS project on gaseous dielectrics. The influence of trace amounts of water vapor on electron avalanche initiation probability in SF_6 near a positive point electrode has been experimentally verified and theoretically explained in terms of likely electron detachment mechanisms for negative ions in the electrode gap. A new method of fitting data on electrical breakdown for binary electronegative gas mixtures has been proposed and applied to the cases of SF_6/N_2 and CCl_2F_2/N_2 mixtures for which discrepancies exist in previously measured and calculated data. The method allows one to evaluate data and provides physical insight into various effects such as synergistic behavior. The corona discharge-induced chemical decomposition rates of SF_6 have been measured for the gas mixtures SF_6/N_2 , SF_6/O_2 , and SF_6/Ne , and the results have been compared with calculations of the maximum possible decomposition rates which were made by using computed electron impact dissociation rates for SF_6 in a model for the discharge. From this comparison, and from data on the production rates for oxygenated by-products like SOF_2 , SO_2F_2 , SOF_4 , and SO_2 , it was possible to gain a better understanding of the fundamental processes that determine the chemical stability of SF_6 in an electrical discharge. A theoretical model for chemical decomposition of gases in a high-pressure corona, or glow discharge has been proposed and applied to the interpretation of experimental results obtained for CF_4 and SF_6 . Using this model, it was possible to explain the observed dependences of oxyfluoride production from SF_6 on discharge current and water vapor and oxygen concentrations.

5. INTERFACIAL PHENOMENA IN LIQUIDS

Task 04

Edward F. Kelley
Electrosystems Division
National Bureau of Standards

5.1 Introduction

The objective of this research is to develop techniques to measure the electrical behavior of liquid-solid composite insulation for use in high-voltage systems. Model systems of practical interest are investigated, such as the interface between transformer oil and pressboard. The effects of contamination and temperature up to $150^\circ C$ is being documented in these model systems in two ways: 1) breakdown measurements using high-speed photography, and 2) electro-optical measurements of the electric field in the vicinity of the interface. Such field measurements provide understanding of the role of space charge and surface charge in high-voltage apparatus.

Electrical failure in high voltage apparatus often occurs in the vicinity of or on an interface which serves as an insulator between two conducting regions of differing potential. However, in well-characterized systems, the

interface will not necessarily cause the failure [42,43]. Additionally, preliminary measurements of the electric field in the vicinity of a pressboard interface, either parallel or perpendicular to the field, have been made previously and reported in the literature [44,45]. Those measurements demonstrated that an interface parallel to the field showed no significant surface charging, i.e. charging which would give rise to large field enhancements. An interface perpendicular to the field, however, demonstrated surface charging as would be expected. Thus, the cause of interfacial failure in practical apparatus does not seem to originate from macroscopic field irregularities arising from the presence of the interface parallel with the field in clean systems.

However, the field measurements reported above were only accurate to within $\pm 5\%$, and extensive studies were only performed on clean systems. Subtle effects due to slight field enhancements would not be observed due to the imprecision of the old apparatus. Additionally, little attempt has been made to determine the role played by contaminants or additives. Preliminary studies have suggested that additives in the oil influence the space-charge generation in the oil, particularly at high temperatures. Also, particulate contamination, and most importantly contamination by conducting particles, influences the breakdown characteristics of systems. Because the overall picture of apparatus failure is complex, it has become necessary to improve our measurement capabilities and widen our scope of investigation.

This report emphasizes four areas in which progress has been made in the understanding of interfacial and liquid breakdown processes:

- 1) The electro-optical field-measurement apparatus has been improved so that field measurement inaccuracies are within 1% and the relative imprecision of any single field measurement can be as low as 0.2% .
- 2) Measurements have been performed on the influence of electrode material on the space-charge generation in transformer oil.
- 3) Studies in breakdown of liquids have been extended by an investigation of streamer propagation characteristics under high pressures. The study was accomplished using a high-speed image-converter camera.
- 4) A preliminary study was made of the nature of partial discharge activity in transformer oil. Photographs of the partial discharge phenomena using a high-speed image-converter camera were taken.

The first item, improved accuracy of field measurements, provides us with a better diagnostic tool to determine differences in the field due to changes in the liquid, either by chemical or particulate contamination, and then to distinguish the liquid's behavior from that arising from the interface. It is important to understand the characteristics of the liquid itself so that no phenomena are incorrectly attributed to the presence of an interface. The electrode material study attempts to determine the role of the electrode material in space-charge production in the liquid. Such knowledge is particularly important for studying interfaces which will cover the electrode surface like a paper wrapping around the coils of a transformer. The liquid breakdown study contributes to our fundamental understanding of the breakdown process in liquids and will guide any modeling efforts. In particular, the

initiation process needs attention, since once a streamer initiates, it requires less voltage to continue to grow. Inhibiting initiation of streamers is, therefore, vital to inhibiting failure. The partial discharge study is not an attempt to characterize partial discharge behavior in liquids, but to provide high-speed photographic evidence for the phenomena which give rise to the partial discharges. If particulate contaminants or voids are responsible, then this fact will provide guidance in the study of interfacial failure in practical apparatus.

5.2 High Precision Field Measurements: Room Temperature AC & DC

Measurements of the electric field have been made with an imprecision of about 0.2% which render field enhancements of 1% quite measurable. Absolute measurements of the field with an uncertainty of 1% is possible. In previous interfacial studies, long plate lengths were required to get useable Kerr-effect measurements. Long interfaces were, therefore, also required. When using paper or pressboard as the interfacial material, numerous small "hairs" of the cellulose material cover the interfacial surfaces. When examined under crossed polarizers to observe the Kerr effect, these "hairs" scatter and depolarize the light seriously reducing the image quality. With the present improvements in the electro-optical measurement system, it is possible to reduce the size of the electrode system and interfaces employed from about 30 cm to about 3 cm. The reduction not only increases the quality of the image, but also increases the speed with which new interfaces can be installed.

In previous studies of the electro-optical Kerr-effect in liquids, such as transformer oil, which have a small Kerr coefficient, residual and temperature-dependent birefringence in the windows used have seriously impaired accuracy and sensitivity of field measurements except at the highest withstand voltages. Special glass windows were used in the new apparatus which exhibit a birefringence of less than 1 nm per cm of glass thickness over the temperature range from room temperature to 150°C. (A birefringence of 1.4 nm would be roughly equivalent to uncrossing a pair of crossed polarizers by 1° -- such an amount of light would be 0.03% of the incident light, or of the same order as the light transmitted by the crossed polarizers with a 10^4 extinction ratio.) At least at the center of the windows where measurements were made, the windows performed within specification.

The windows used in earlier experiments had a residual birefringence at least ten to twenty times worse than exhibited by the new glass. This prevented precise intensity measurements and produced field-measurement imprecision of 5% or more. Because of the new windows, careful measurements of small amounts of space charge at room temperature could be made for the first time.

In the following experiment, parallel-plate electrodes were used having a length of about 15 cm, a width of about 2.2 cm, and a plate separation of about 0.5 cm. The transformer oil was circulated through the cell during all measurements. Compared to the turbulence during the application of the voltage, however, the relatively slow speed of the liquid due to the circulation pump could be entirely ignored. The liquid pump served to rid the gap area of postbreakdown bubbles and particulate byproducts. The laser light

source which was used in earlier investigations was replaced by an incandescent light bulb. The bulb provided a more uniform illumination which was not readily affected by the turbulence of the liquid in the cell.

5.3 Space Charge in Transformer Oil at Room Temperature -- AC & DC

With dc, the maximum enhancement of the field due to space charge was about 5% above the average field. The breakdown field was (193 ± 14) kV/cm, and the 5% enhancement was measured at an average field of 187 kV/cm -- within the expected breakdown range. The space charge was found to fill the gap rather uniformly having a density of -7 nC/cm^3 . In earlier measurements using heated oil, the same polarity of charge was found to reside nearer the anode than the cathode and was therefore identified as heteropolar charge. However, the space charge observed here appeared to fill the region between the plates uniformly as indicated by the constant slope of the electric-field profiles shown in figure 17.

Figure 17c shows the relatively long time constant associated with the development of the space-charge under dc voltage. Positive polarity was maintained on the right plate until equilibrium was reached in the distribution of space charge -- the space charge was uniformly negative. The polarity was then quickly reversed (within about 3 minutes) and the enhancement of the field remained at the same location initially, but within a minute or so, the enhancement slowly returned to the anode which was now the left electrode -- thus the space charge returned to being uniformly negative. However, immediately after the polarity was changed to negative, the enhancement was nearer the negative electrode which indicates that the charge between the electrodes was initially positive -- only the direction of the field changed, the derivative of its magnitude did not. This type of behavior suggests that the dc enhancement is due to features of the liquid-electrode interface, and not to migration times of the charges. The turbulence associated with these voltages would quickly mix any low-mobility charges throughout the gap.

If one assumes that the migration of the space-charge is slow (ignoring the turbulence for the sake of argument) and that the uniform negative space charge which was produced while the high voltage electrode was positive persisted after the voltage was turned off, then when the negative voltage was applied with the negative space charge present the slope of the enhancement would have immediately changed -- the enhancement would have immediately appeared at the anode. This is not observed. Upon polarity reversal the enhancement remains at the same physical electrode (now negative) which means that the polarity of the uniform space charge is positive. A picture which may explain these data is that during dc voltage application charge injection is impaired at one electrode and not the other. Upon polarity reversal the conditions which inhibit injection at the one electrode are not immediately changed but require time to be reduced and build up at the other electrode. This hypothesis is, of course, very tentative. More work is needed to document the response of transformer oil before serious modeling attempts can be made.

The behavior of transformer oil subjected to ac, 60 Hz, is quite different than for dc as far as space-charge characteristics are concerned.

a) ELECTRO-OPTIC DC FIELD PROFILES AT 24°C

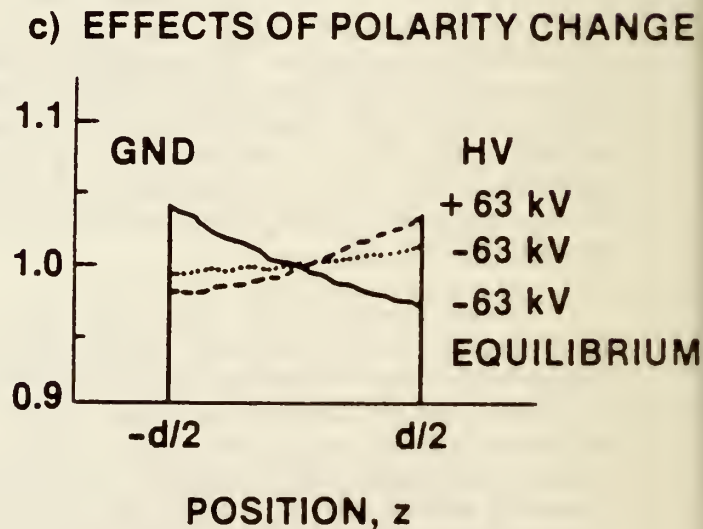
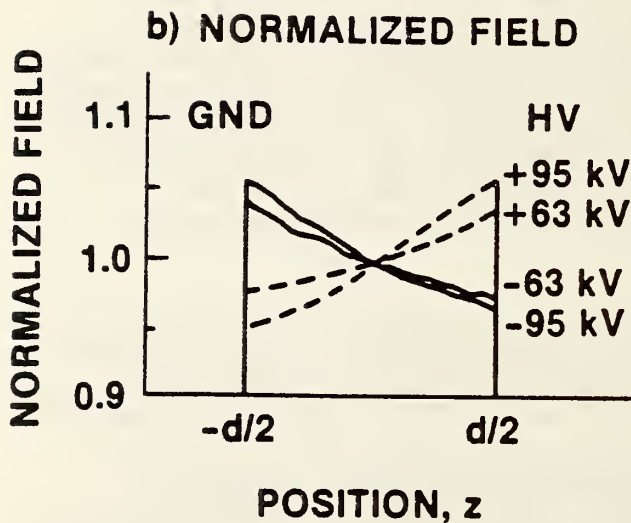
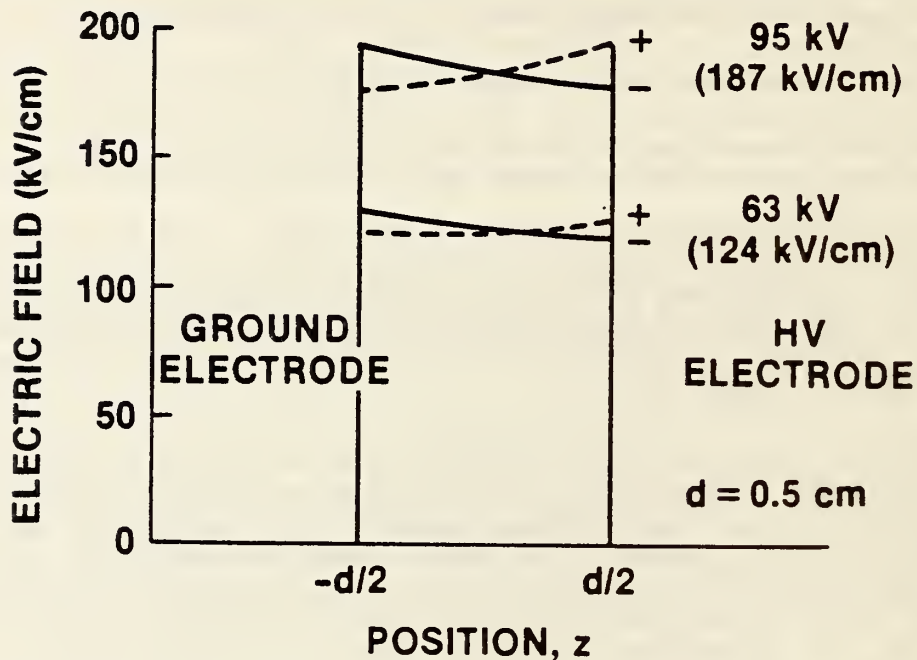


Figure 17. Electro-optical, Kerr-effect, dc field measurements in transformer oil at room temperature. Solid lines show the negative polarity, dashed lines, positive polarity. The numbers in parentheses are the average applied field. In b) the normalized field is shown to emphasize the enhancement. In c) the normalized fields are shown for the 63 kV profiles to illustrate the temporal behavior of the enhancement after changing polarity. The dotted line is the field found just after the polarity is changed from positive to negative. After a few minutes the enhancement for the negative applied voltage gradually becomes that shown by the solid line.

Figure 18 shows the field enhancement at room temperature for ac. The breakdown peak voltage for ac, around 130 kV (256 kV/cm), was too large to be measured with the present apparatus. The data were taken at 118-kV peak (232 kV/cm) which was probably within a standard deviation of the breakdown voltage. The space-charge density is about $+2 \text{ nC/cm}^3$, and is relatively uniform through the gap. Thus, the space charge at room temperature for 60 Hz ac is opposite in sign and smaller in magnitude than that observed using dc.

5.4 Space Charge in Transformer Oil at 125°C -- AC & DC

At temperatures around 125°C, more space charge is found for both ac and dc than at room temperature. With dc, the breakdown fields are reduced from 193 kV/cm at room temperature to $(146 \pm 14) \text{ kV/cm}$ at the high temperature -- a 24% decrease. Field enhancements of about 20% next to the anode are shown in figure 19. For such data to be taken it was necessary to shorten the data accumulation time because breakdown would occur within a few seconds. These fields indicate that a relatively uniform negative space charge is present of about -20 nC/cm^3 . At lower fields, the space charge was larger near the anode than the cathode.

Under the application of 60-Hz ac the breakdown fields were lower: $(228 \pm 14) \text{ kV/cm}$ which is 11% lower than the approximate value at room temperature. The field profiles are shown in figure 20. The U-shaped fields are produced by bipolar homocharge having a larger positive component at the anode, that is, a negative space charge is observed near the cathode (about -16 nC/cm^3), but a positive space charge having a larger magnitude is observed near the anode (about 24 nC/cm^3). Despite these rather large charge densities the field is enhanced less than 3% mid-gap and is decreased as much as 5% next to the anode.

Although the field is decreased at both electrodes for the high-temperature ac data, a decrease in the strength of the oil is observed. The 11% decrease in strength is a tentative result and further research is needed to confirm it. It does suggest, however, that the breakdown process in liquids may not be dependent solely upon the average field strength at the electrodes. Other processes no doubt are involved. The advantage of electro-optical measurements is that, by knowing the electric field, one can separate field effects from other factors which could influence the breakdown process like the particulate content of the liquid, electrohydrodynamic motion, chemical nature, etc.

5.5 Electrode Material Effects on the Generation of Space Charge

Through Kerr-effect studies on other liquids, it has been established that space charge can depend upon the type of metals used for electrodes. This was noted by E. C. Cassidy, et al. [46] and more recently M. Zahn has extended the results to water [47]. This project attempted similar measurements in transformer oil.

To determine space charge as a function of electrode metal, an electrode system was constructed which mounted four different metals in one cell, see figure 21. Because of the electrodes' proximity, small differences in charge

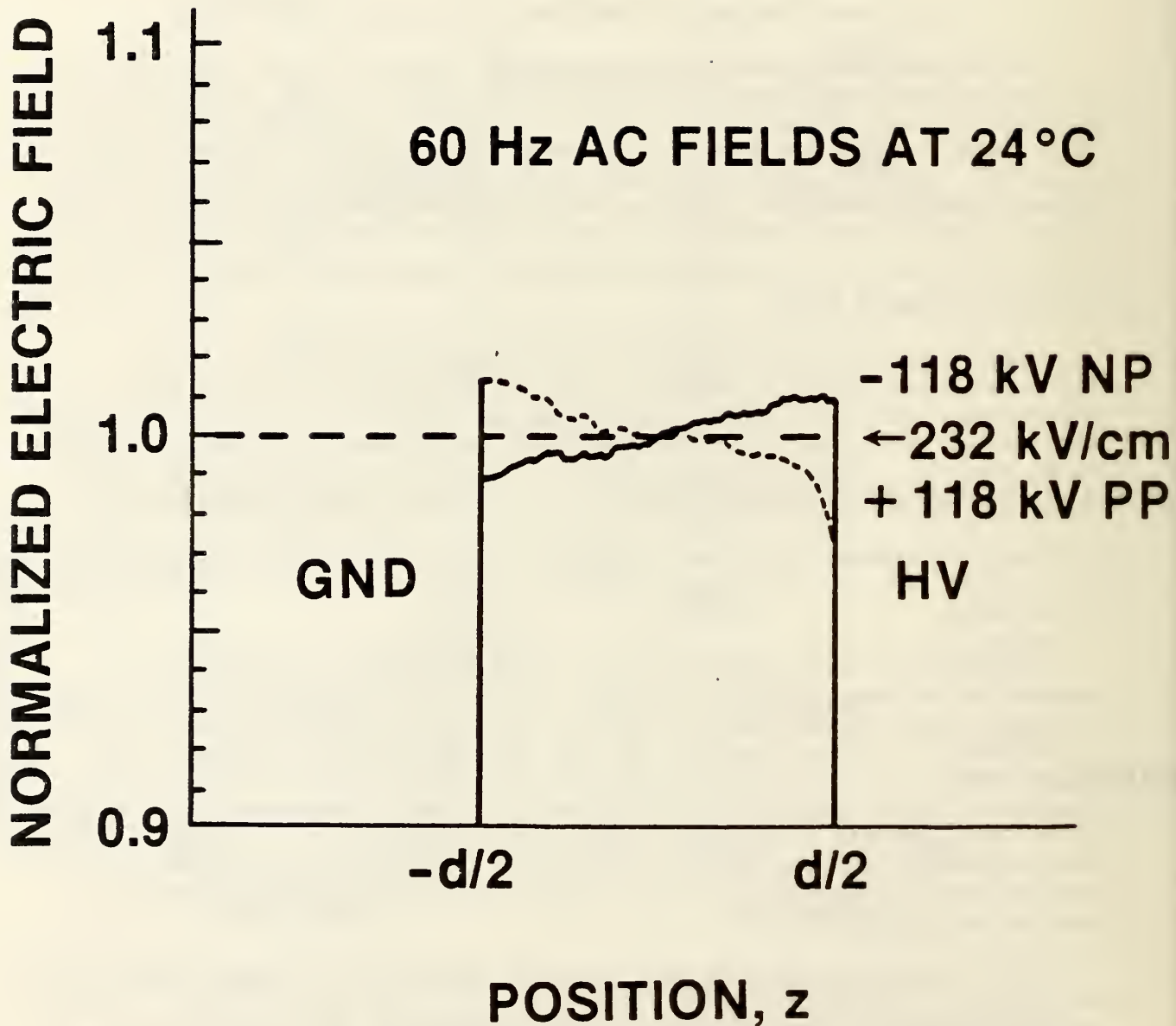


Figure 18. Normalized electric fields for 60 Hz ac at room temperature. NP and PP refer to negative peak and positive peak respectively. The sudden drop in the positive peak profile near the HV electrode is an artifact of the detector and not some unusual decrease in the field near the plate. The average peak field is 232 kV/cm.

DC FIELDS AT 125°C

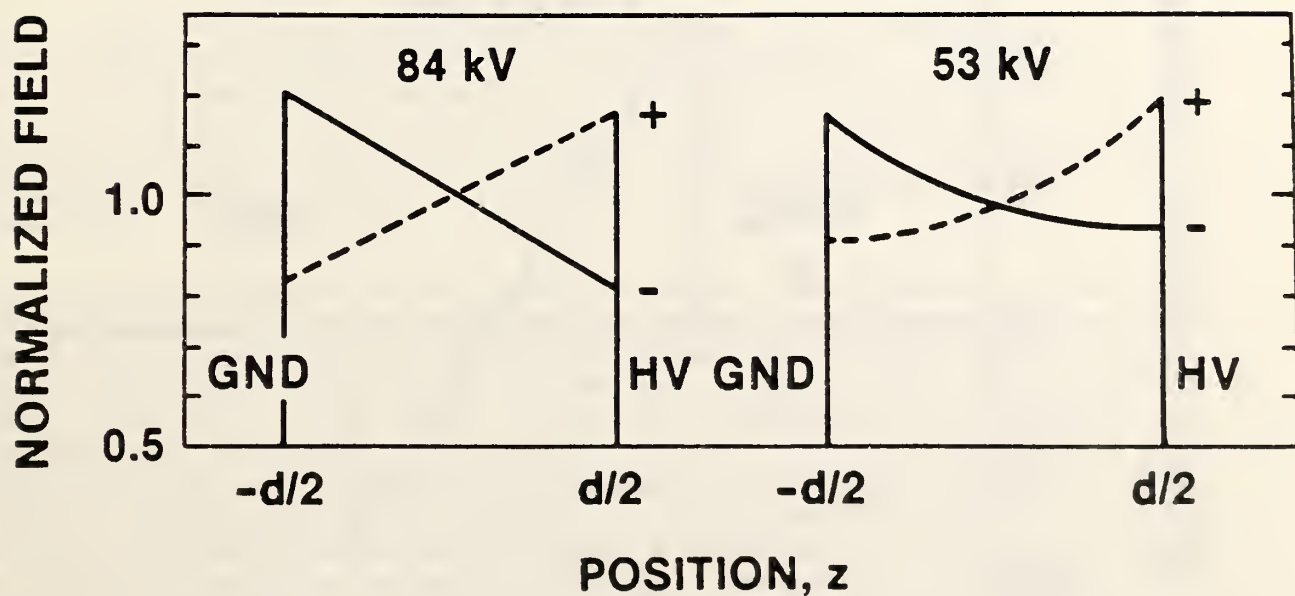
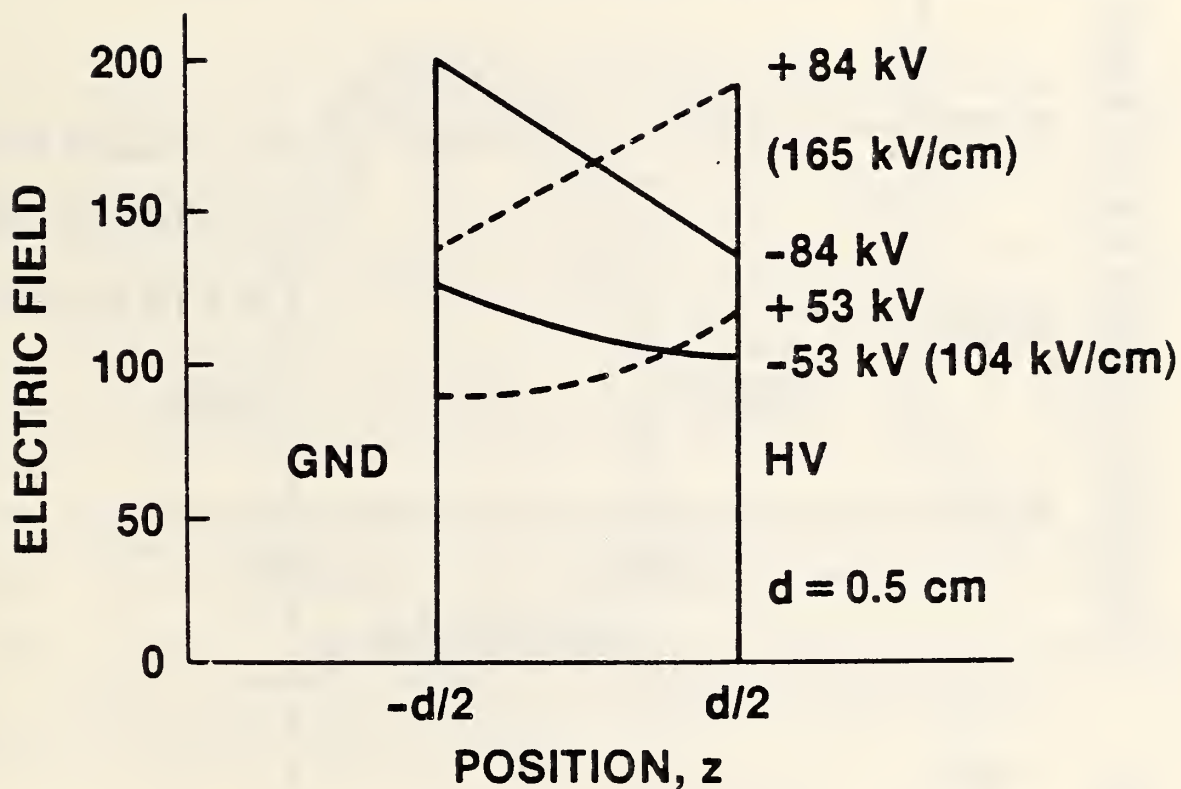
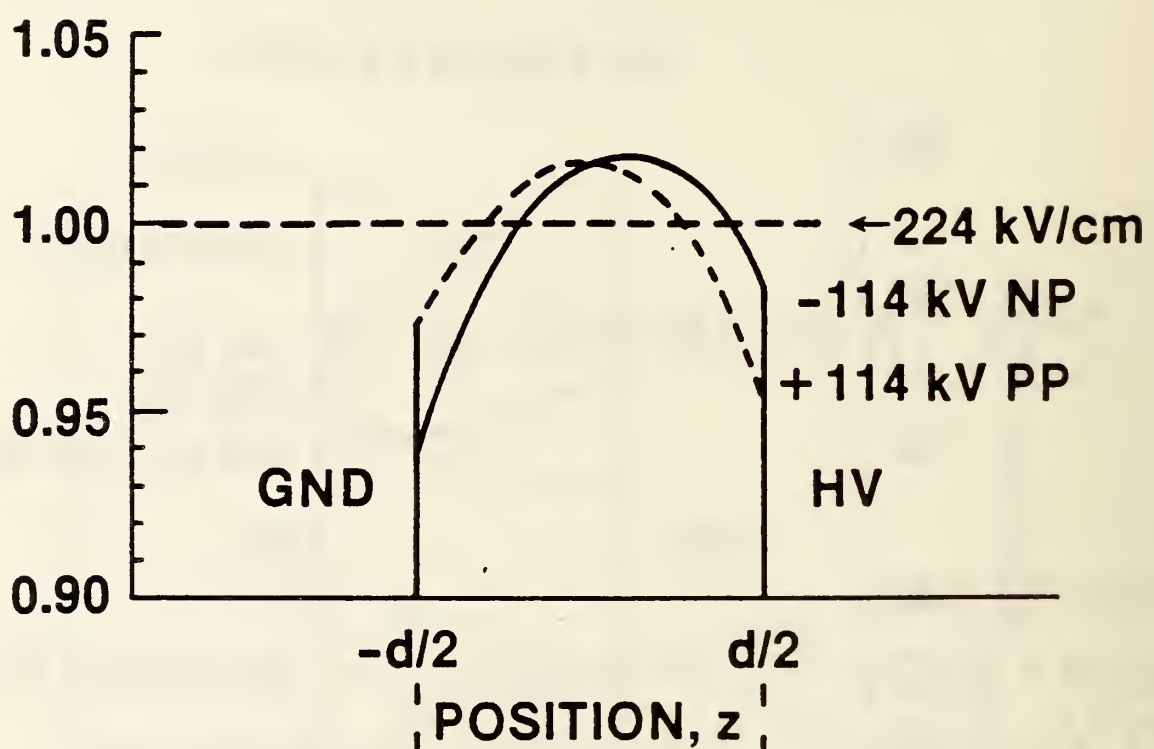


Figure 19. Electric fields for dc at 125°C. At lower fields there is less space charge near the cathode.

NORMALIZED ELECTRIC FIELD

60 Hz AC FIELDS AT 125°C



SPACE CHARGE (nC/cm³)

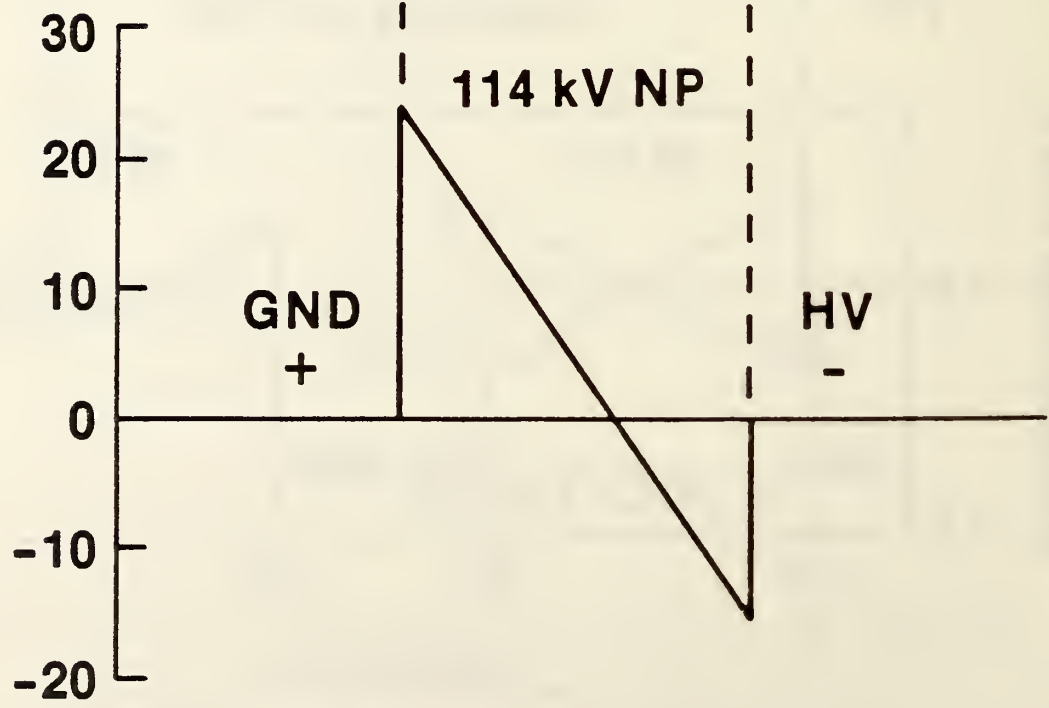


Figure 20. Electric fields for 60 Hz ac at 125°C. NP and PP refer to the negative and positive peaks of the 60 Hz waveform respectively. The average peak field is 224 kV/cm. The space charge, which is proportional to the derivative of the field, is shown for the negative peak profile.

injection may not be observable. If the charge injection process were significantly different for different electrode materials, however, such a configuration should render the differences obvious. Since transformer oil tends to change its characteristics regarding space charge production as it ages or is cycled through temperatures, the same oil sample was used for all the metals at the same time.

The results using dc voltage were surprising in view of similar studies with other liquids. No differences were observed in the space-charge production, independent of the metals used. These results were obtained near the breakdown voltage of the system. Figure 22 shows the light intensity data obtained at room temperature. This is not the electric field, but the intensity data; the electric field exhibits much less enhancement. The data are also obtained using windows which have some residual birefringence which could not be eliminated. This has the effect of giving each profile a slight slope. The important point is that each metal exhibits the same enhancement upon polarity reversal within the error of measurement which could be rather large for this preliminary experiment -- as high as 10% to 20%. No attempt has been made to scale the data to account for nonuniform incident light illumination which causes the height of each profile to be slightly different.

To reduce synergistic effects between neighboring electrodes, two of the inner electrodes were removed so that the differing metals were more widely separated. There was no change in the electro-optical behavior noted above.

Thus, in order to detect subtle differences, if they exist, the apparatus must be refined or changed. Further, a comparison with 60-Hz ac must also be made. It must be emphasized that this is a result of an exploratory experiment and further work will be done.

5.6 Liquid Breakdown Phenomena

A liquid handling system has been installed which permits the characterization of prebreakdown streamers in liquids as a function of pressure from atmospheric pressure (0.1 MPa) up to 30 MPa. Initial experiments were conducted up to 10 MPa on n-hexane. The breakdown voltage for both polarities was found to increase as the pressure increased. The increase was linear within the imprecision of the breakdown voltage measurement, typically 10%.

As the pressure increased, the thickness of the streamer branches became thinner for both the anode and cathode streamers. At higher pressures, near 1 MPa, the subsonic cathode bush, which appears routinely at atmospheric pressure would not be found. At 0.6 MPa, the subsonic bush would occasionally occur. In addition, near 1 MPa and near the threshold of the breakdown the streamer would initially be quasi-sonic, but as it extended across the gap it would slow down, stop growing and disappear just as if the voltage had been removed, suggesting a minimum voltage of propagation [48]. The increase in breakdown and the suppression of streamer development with increasing pressure are consistent with the assumption that the breakdown of a liquid at room temperature involves a change-of-phase. The increase in the hydrostatic pressure would impede the growth of the lower density region which could lead to the observed behavior.

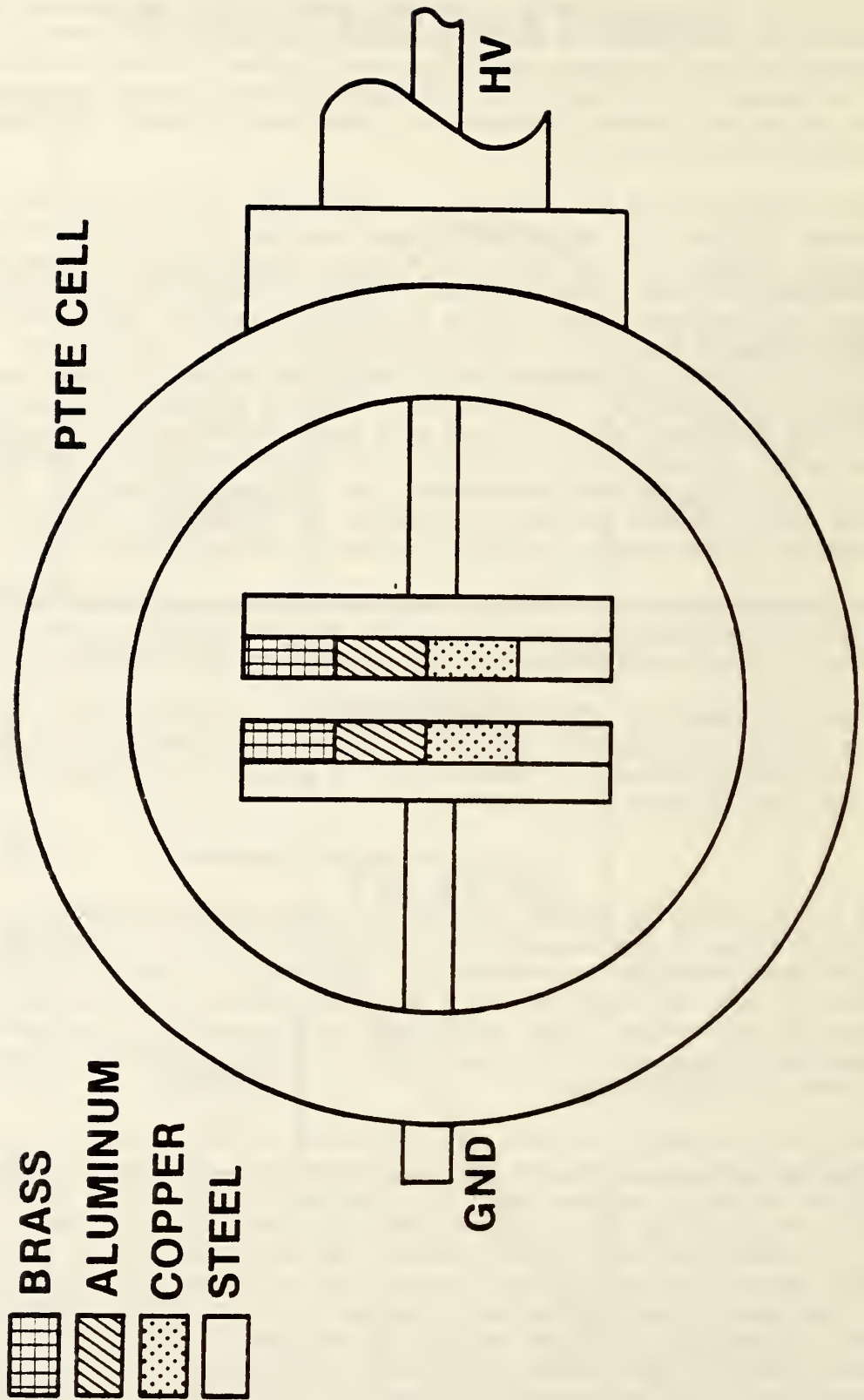


Figure 21. Multi-metal electrode configuration to reveal dramatic difference between electrode metals in production of space charge while employing the same liquid. The gap is 0.635 cm, plate width is 1.27 cm and the length of the plates is 15 cm (into the page).

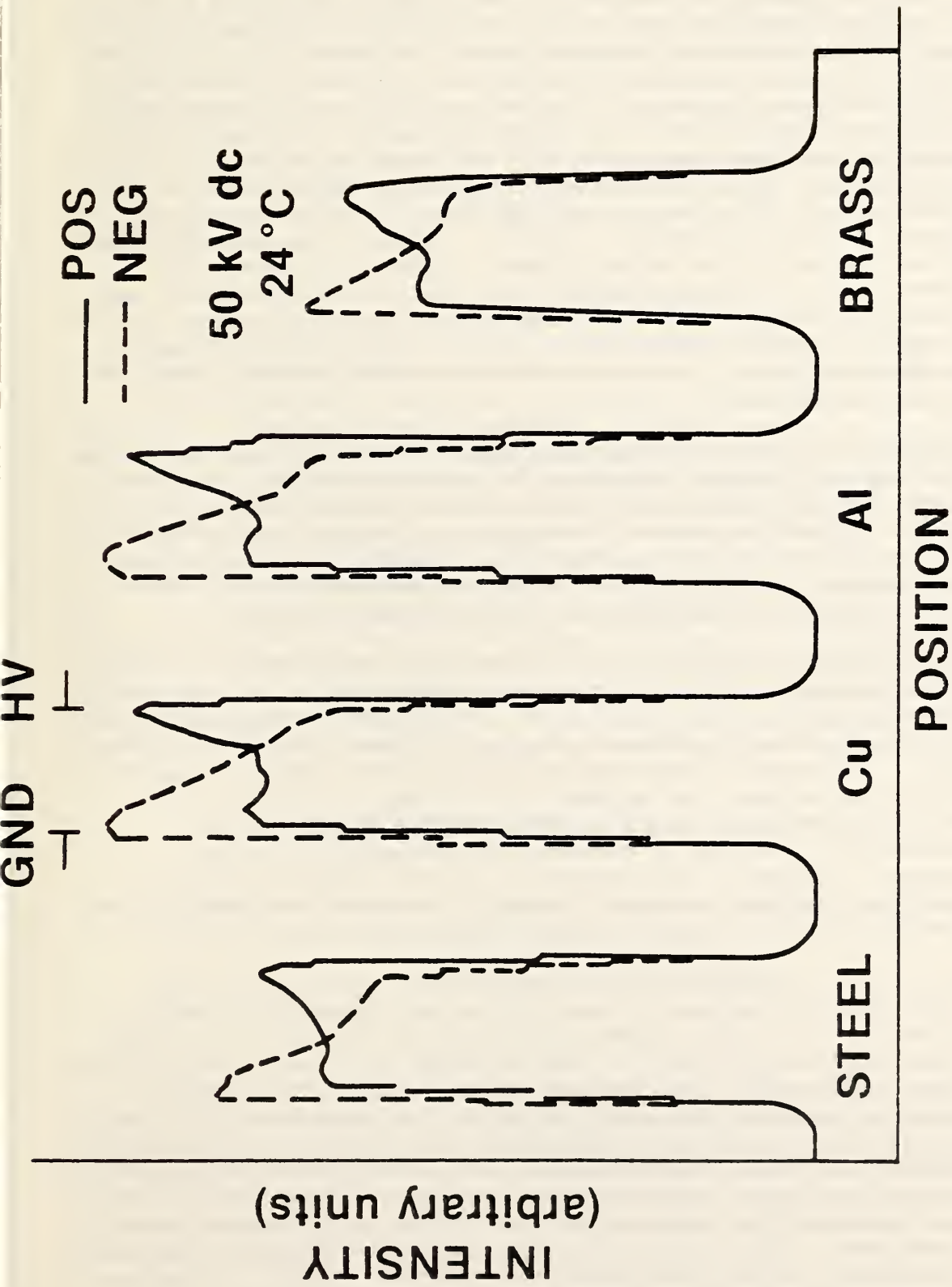


Figure 22. Intensity profiles for different electrode materials under the application of 50 kV dc, both polarities, room temperature. No attempt has been made to compensate these data for nonuniform incident light intensity. Since large diameter windows having a residual birefringence were used the intensity profiles on the average have a slight slope. The important feature is that the same space-charge behavior is noted independent of electrode material.

5.7 Partial Discharge Measurements and Their Photography

Partial discharge measurements are of interest since they tend to be an indicator of problems which can lead to apparatus failure. A detection system was assembled which could detect 1-pC discharges. The system was calibrated by discharging a 2-pF capacitor charged to 9 V using a mercury-wetted relay with the cell's electrodes connected. The cell was filled with transformer oil and the electrode spacing was 2 mm or 4 mm, depending upon the experiment. Both electrodes had spherical surfaces with a radius of curvature of 1.3 cm. The transformer oil was circulated through a 2- μ m paper filter prior to the application of voltage. It is anticipated that most of the particles are removed; however, as soon as voltage is applied, particles are drawn from the sides of the cell. Even if the entire system is carefully cleaned with various solvents and an ultrasonic cleaner, one breakdown produces many small particles presumably from the electrodes and cell walls which were not removed despite the careful cleaning. Thus, after several breakdowns, the liquid is circulated through the filter. It is believed that this treatment produces the minimum particle content.

Since breakdown voltage levels were employed, it was necessary to provide protection for the oscilloscope's amplifier so that the breakdown currents would not damage the oscilloscope while observations were being made on a millivolt scale. In addition to the electrical measurements, two optical methods were used to view the partial discharges. Either a photomultiplier detected light emitted from the gap, or high-speed photographs were taken using an image-converter camera after a partial discharge occurred.

When the transformer oil was clean and even after a few breakdowns had occurred, it was necessary to wait on the order of one minute or longer for a partial discharge having a magnitude of 1 pC or larger, to be detected by the oscilloscope. A coincident light pulse was almost always observed with the photomultiplier. The partial discharge could be observed with the unaided eye, provided several minutes were allowed for the eye to adjust to the darkened room. In general, it is anticipated that the pulse from the photomultiplier will be somewhat proportional to the partial discharge magnitude, however, because of the spherical electrode geometry used, the photomultiplier does not see the entire surface of the electrode equally, and a strict correlation of pulse magnitudes was neither expected nor observed.

To test the effect of conducting particles on the partial discharge behavior, a few cubic millimeters of iron filings were added to the cell. Upon the application of voltage, there was an increase in partial discharge activity. A dim glow could be seen on both electrode surfaces in the vicinity of the gap, and occasionally, what appeared to be a larger particle would bounce between the electrodes emitting flashes of light each time it hit an electrode. A peculiar rare event was also observed, we might term it a partial breakdown. One could see a breakdown bridge the gap but it was not complete in the sense that it did not lead to voltage collapse. The optical and acoustical emissions from these partial breakdowns were less than those from a full breakdown. High-speed photography of partial breakdowns did not reveal any difference from the full breakdowns; however, in all the high-speed photographs, particles could be seen along the post-breakdown, high-current channel. Presumably the presence of the particles influenced the post-breakdown phenomena.

To isolate the location of the partial discharge to a small area, the ground electrode was changed from a sphere-like surface to a needle with a tip radius of curvature of approximately 30 μm . The gap was 5 mm. Upon the addition of conducting particles, partial discharge activity was readily observed by the detection system. Attempts were then made to photograph the partial discharge activity. In almost all cases, some streamer initiation activity existed in the vicinity of the tip of the needle whenever a partial discharge occurred. Unfortunately it was not possible to identify the source of the initiation since all the photographs were taken after the discharge occurred. More work is clearly needed. Most of this investigation, however, will be done as a part of a new DOE-funded project at the University of Tennessee.

5.8 Summary

The objective of this task is to understand failure in high voltage apparatus. Usually failures involve interfaces, so research to understand interfacial phenomena associated with liquid-solid composite insulation is necessary. Diagnostic techniques have been developed to monitor the electrical behavior of oil, and a measurement system has been devised to provide 1% field measurements in liquids with imprecisions of 0.2%. With such accuracy, subtle changes in the liquid can be monitored with respect to additives and particulate contamination. Partial discharge activity can also be monitored and its influence on practical insulation systems can be evaluated in terms of modification of the space-charge characteristics of the oil. Coupling these measurements with high-speed photography provides a more complete picture of the time evolution of failure in a practical system with interfaces. Simultaneous measurements, electro-optical field measurements, partial discharge measurements, and high-speed photography, are quickly coming within the realm of possibility. With such a complete documentation of the breakdown process, it will be possible to isolate those parameters which significantly affect the failure in apparatus.

6. NANOSECOND BREAKDOWN IN POWER SYSTEM DIELECTRICS Task 05

Ronald H. McKnight, William E. Anderson, David L. Hillhouse,
and Charles Fenimore
Electrosystems Division
National Bureau of Standards

6.1 Introduction

The objectives of this effort are to develop measurement capabilities and provide data in support of the DOE program concerned with the effects of fast-rising electrical signals on electric power systems. Whereas the effects of microsecond rise-time pulses are reasonably well understood, the effects of nanosecond rise time pulses on power system dielectrics are not well known. Appropriate model test systems will be developed along with the necessary measurement techniques.

There are several aspects to this effort which were investigated during the year. The technical areas discussed are all related to the subtask objectives and are interdependent. These areas are the development of test

facilities, including measurement systems; mathematical methods to characterize measurement systems with primary emphasis on deconvolution techniques; electro-optic measurements of fast transients to improve measurement capability; and observations of streamer growth in dielectric fluids for fast risetime voltages to verify that nanosecond and microsecond processes differ.

6.2 Test Facilities

A coaxial test line has been modified so that it is suitable for both high voltage and low voltage operation. This allows the use of a well characterized signal on the test line, and presents an optimum method for evaluating sensors, since the low voltage waveform is more repeatable than would be expected for a spark gap pulser.

As a part of these investigations, a new flat plate sensor configuration, assembled by using an adhesive-backed polyester dielectric and a sprayable conductive coating, was evaluated. Although the new configuration was easy to install and appeared to have electrical characteristics similar to the plug divider which has been extensively examined [49], detailed analysis indicated that the dielectric constant of the material-adhesive combination varied considerably over the frequency range of interest and that other dielectrics will have to be chosen. The sensors to be used in the future will be based on the gas dielectric (plug) divider developed in earlier work. A commercial Rogowski coil has been installed in the line in the test section, which is equipped with several ports for mounting instrumentation and will allow comparisons between various types of current sensor. While the current measurement is not explicitly part of the DOE program, it is necessary for overall understanding of fast transient measurements and completes the instrumentation of the coaxial test line.

The accuracy of a transient measurement is determined by the overall measurement system which includes the sensor, the signal transmission system and the data recorder. As part of the system evaluation, calibrations of the waveform recorders were begun. The recorders used have approximately 500-MHz bandwidth with sub-nanosecond rise times. Measurements made using well known dc levels indicated anomalous system response and it was determined that the units being used were defective. Because the measurements are made for sub-microsecond pulses but the calibration is made using a 1-kHz square wave, there remains a question concerning the validity of the calibration procedure. In the near future, a step generator developed at NBS [50] will be configured for use as a calibration device.

Although designed to determine the step response of slower waveform recorders, it appears that the generator may be useful as a calibrator (within a given accuracy range) for the digitizers being used here. This calibration procedure is crucial, since comparisons of different measurement techniques can only be done by knowing the overall accuracy of each measurement. Estimates of accuracy are also necessary if critical evaluations of mathematical methods of signal processing, such as deconvolution are to be made.

6.3 Mathematical Methods

One of the impediments encountered in comparing different sensors or characterizing a single sensor is the lack of equivalent circuits to be used in modeling. A description in terms of frequency response is usually incomplete, and is not practical for devices which are required to have nanosecond response, such as those in use here which are not amenable to analysis by use of microwave techniques. An approach to describing the sensor in terms of a measured step response and the manipulation of measurements using deconvolution methods was outlined in a previous report [51]. In this method, the response of a given sensor to a step-like signal is determined using the coaxial test line. By measuring the input signal independently, step and impulse responses for a sensor can be calculated. Using this response, a given input can be calculated by deconvolution. In mathematical terms, if the system is linear, causal, and time invariant, the input signal $x(t)$ and the output signal $y(t)$ are related by using the convolution integral

$$y(t) = \int_0^t x(s) g(t-s) ds, \quad (63)$$

where g is the impulse response of the system [52]. Given 2 of the 3 quantities x , y or g , the equation can be solved for the third. Difficulties encountered in solving this integral equation were discussed in [51], and extensively in the open literature.

The methodology has been applied to a number of different sensors, examples of which are presented here. Two separate sensors, a capacitive sensor with a coaxial, air dielectric, low side and a resistive divider with adjustable stray capacitance, were mounted in the coaxial test line. Measurements were made using two different signals, each of which was sent down the line and detected by the two sensors. The first of these was a step-like signal, which was independently recorded and used in conjunction with eq (63) to determine the impulse response of each sensor. The second of these was a "test" signal, which was generated by sending the step signal from the pulse generator through an impedance which was primarily inductive. The step and test signals are shown in figure 23. The response of the capacitive divider to these two signals is indicated in figure 24. The droop associated with the limited low frequency response of the capacitive sensor is seen on the response to the step, as is the distortion of the test signal (compare with the directly recorded input in figure 23). An impulse response g was calculated for the capacitive divider using eq (63), where x is the directly recorded input (step-like signal) and y the response of the sensor, mounted in the test line, to the step-like signal. This impulse response was then used, again in eq (63), to calculate the input waveform x for the recorded test waveform output y . The comparison of the input waveform calculated using the deconvolution method and the directly measured input waveform is shown in figure 25, where the waveforms have been offset in time to facilitate comparison.

A similar procedure was followed for the resistive divider. Although not shown, the response of the divider was adjusted so that there was an overshoot on the divider response. This overshoot is obvious in figure 26, where the measured input and output signals for the test waveform are shown. As with the capacitive divider, the step signal and divider response were used to

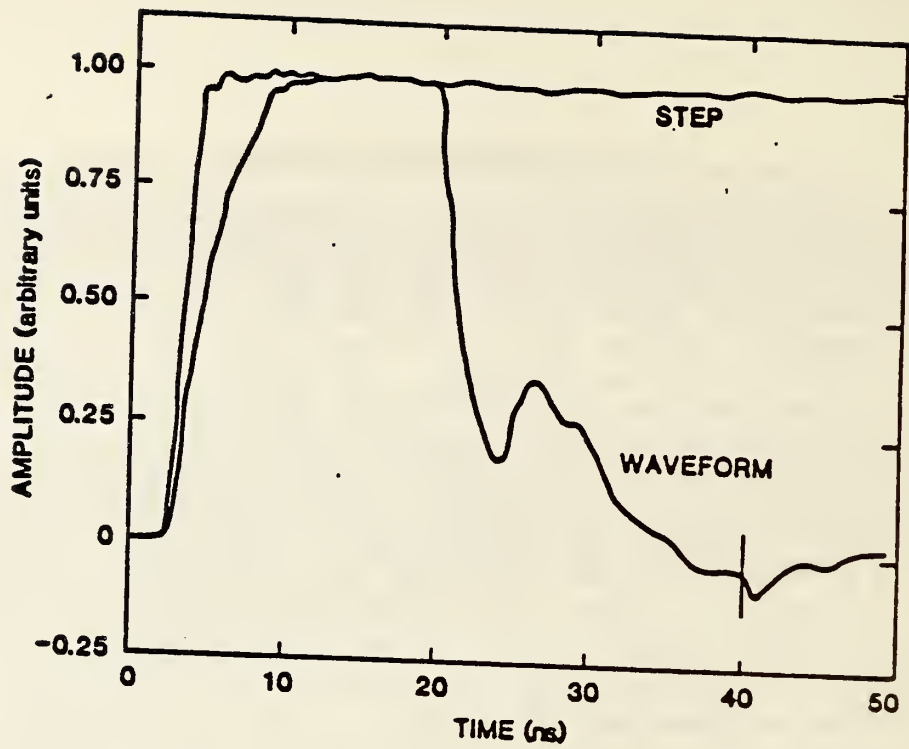


Figure 23. Waveforms used in studies measured directly from pulse generator. The test waveform does not replicate beyond 40 ns as indicated.

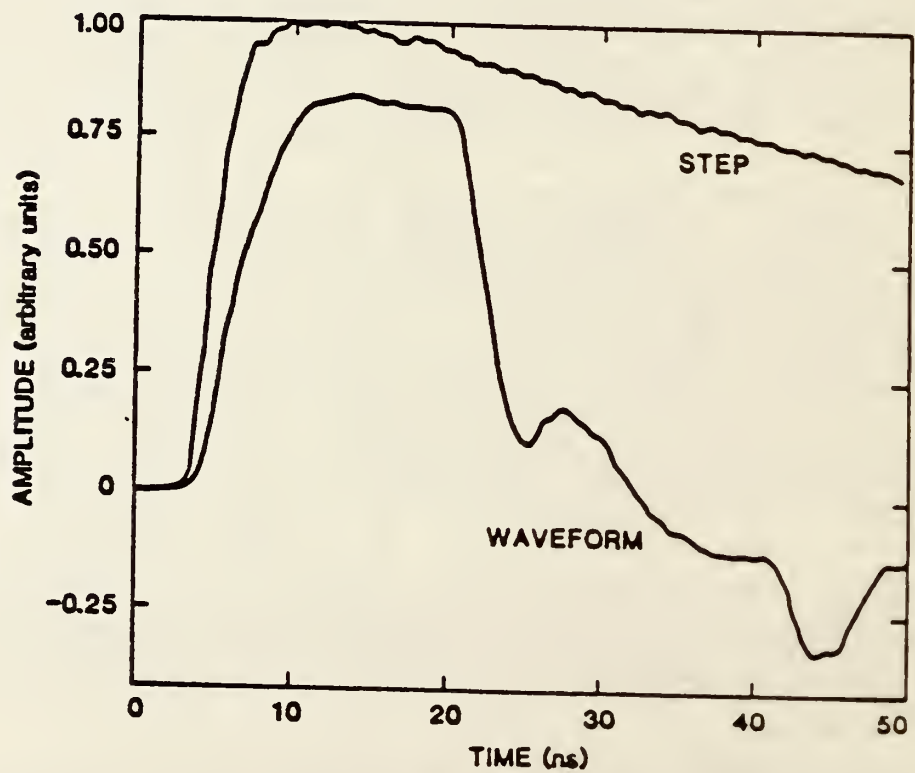


Figure 24. Output signals from a capacitive sensor for test line input signals shown in figure 1.

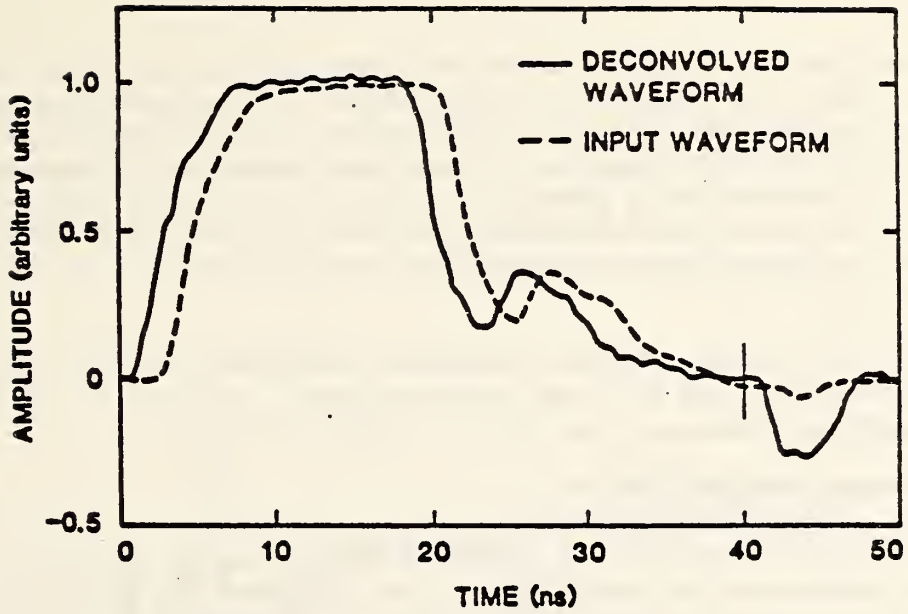


Figure 25. Comparison of deconvolved and input signals for the capacitive sensor. Signals have been offset for comparison.

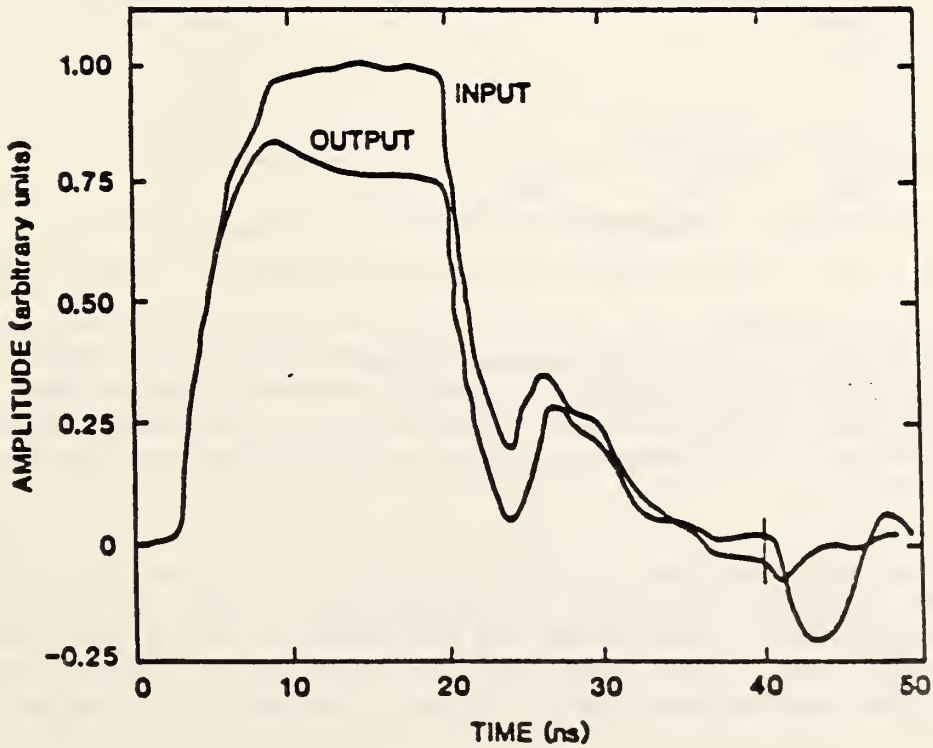


Figure 26. Comparison of the output signal from a resistor divider with the input signal.

determine an impulse response, which was then used in the deconvolution integral eq (63) to calculate the input signal. Calculated and measured signals are compared in figure 27. In each of the cases presented here, the deconvolved and directly measured signals show excellent agreement. Other waveforms and theoretically generated functions are being compared to provide a basis for estimating uncertainties generated by the deconvolution process. Some aspects of this work were described in greater detail at a recent Pulse Power Conference [53].

The use of discrete Fourier transform techniques [54-56] to deconvolve the two signals $y(t)$ and $x(t)$ was also examined. If $y(t)$ is related to $x(t)$ through eq (63), then

$$Y(\omega) = G(\omega) X(\omega), \quad (64)$$

where $Y(\omega)$, $G(\omega)$ and $X(\omega)$ are the Fourier transforms of x , g and y . In general the problem is to solve for g , (or x), given the other two quantities. This suggests that the deconvolution could be accomplished by Fourier transforming y and x , calculating the ratio, and then back transforming.

In practice, the situation is different in that all the waveforms are expressed by their value at discrete periods of time (i.e. they have been sampled). The question then is, if

$$y_s(t) = g_s(t) * x_s(t) \quad (65)$$

does

$$Y_s(\omega) = G_s(\omega) X_s(\omega), \quad (66)$$

where Y_s is defined to be the discrete Fourier transform of the sampled waveform y_s and "*" indicates the convolution operation. The answer to this question is, in general, no. The relation does hold if the convolution product is defined to be a circular convolution as opposed to the linear convolution that is of interest. (A circular convolution assumes that all waveforms repeat at cycles equal to the inverse of the sampling frequency and the convolution is calculated by taking contributions from adjacent cycles.) In other words $g_s(t)$ can be calculated but it has no physical significance.

A method was described in the literature [56] to use the circular convolution approach to perform the deconvolution. This method will work for only a special class of waveforms and was found to be too restrictive to be of value for this work. Other approaches of treating the special problems of non-repetitive sampled data (which is the situation for all measurements considered here) may be useful and are under consideration [54].

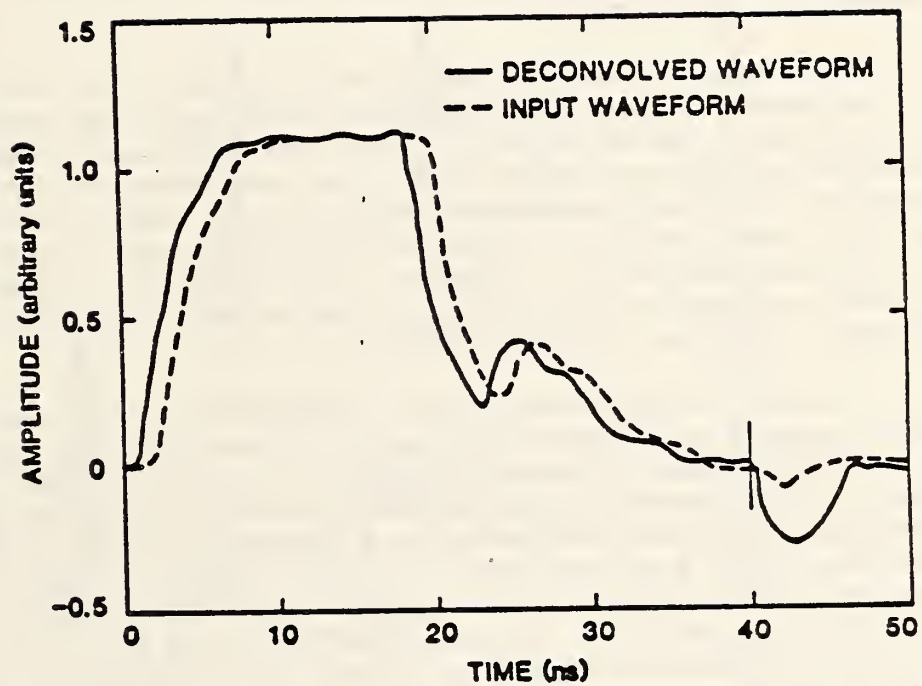


Figure 27. Deconvolved and directly measured input signals as obtained using the resistor divider. Signals have been offset for comparison.

6.4 Electro-Optic Methods

The use of electro-optic technology in measurements of physical quantities is proliferating, with applications in many areas. NBS has extensively studied and applied the Kerr effect to the measurement of electrical quantities, including voltage pulses and space charge in dielectrics, applications described in earlier publications [57-59]. More recently, exploratory efforts have begun to examine selected electro-optic techniques to measure transient electrical quantities, such as voltage and current. Although only part of this work is supported by DOE, it is worthwhile to describe briefly the work that is being done and its relevance to nanosecond measurements.

The literature describing measurements using fiber optic and electro-optic techniques is growing rapidly and review articles have appeared in both U.S. and foreign journals [60-62]. The few references presented here are representative and are not intended to be comprehensive, even though they are limited to electrical measurement applications. Papers have appeared describing power industry measurements [63], transient signal applications [64], EMP measurements [65], electric field mapping [66] and completely "photonic" systems in which signal transmission, sensors and recording devices are based on the use of light [67].

A schematic representation of a measurement system which can be used to measure voltages or currents is shown in figure 28. The important features are (i) a light beam of known polarization incident on the electro-optic medium; (ii) an optically active sensor, which is a system in which the transmission of light is affected by an external agent imposed on the sensor; and (iii) a polarization analyzer. Suitable light sources, detectors, and signal recording devices are also necessary. To illustrate the type of systems that may be used, the sensor may be a Kerr cell, a solid material exhibiting the Pockels or Faraday effects, or a single mode optical fiber. For any given measurement, not all of the components shown will be necessary, and the geometric relationship between the light beam, direction of the field, and the electro-optic medium will be determined by the application as will the polarization of the light beam.

The use of the Pockels effect is particularly attractive for a number of applications, including measurements of steady state voltages, transient voltages, and electric field mapping. An analysis of this system indicates the salient features of the measurement. Referring to figure 28, if the polarizers are crossed and oriented at $\pm 45^\circ$ to the optical axis of the crystal, it can be shown that the system acts as a phase modulator and that the normalized intensity transmitted through the second polarizer is

$$I/I_0 = \sin^2 \Gamma/2, \tag{67}$$

where I is the transmitted intensity, I_0 the incident intensity, and Γ the relative retardation (phase shift) for the two components of polarized light passing through the crystal [68]. The phase shift depends on the material used as the sensor, its shape and orientation, and ignoring natural birefringence and effects due to other external parameters (such as

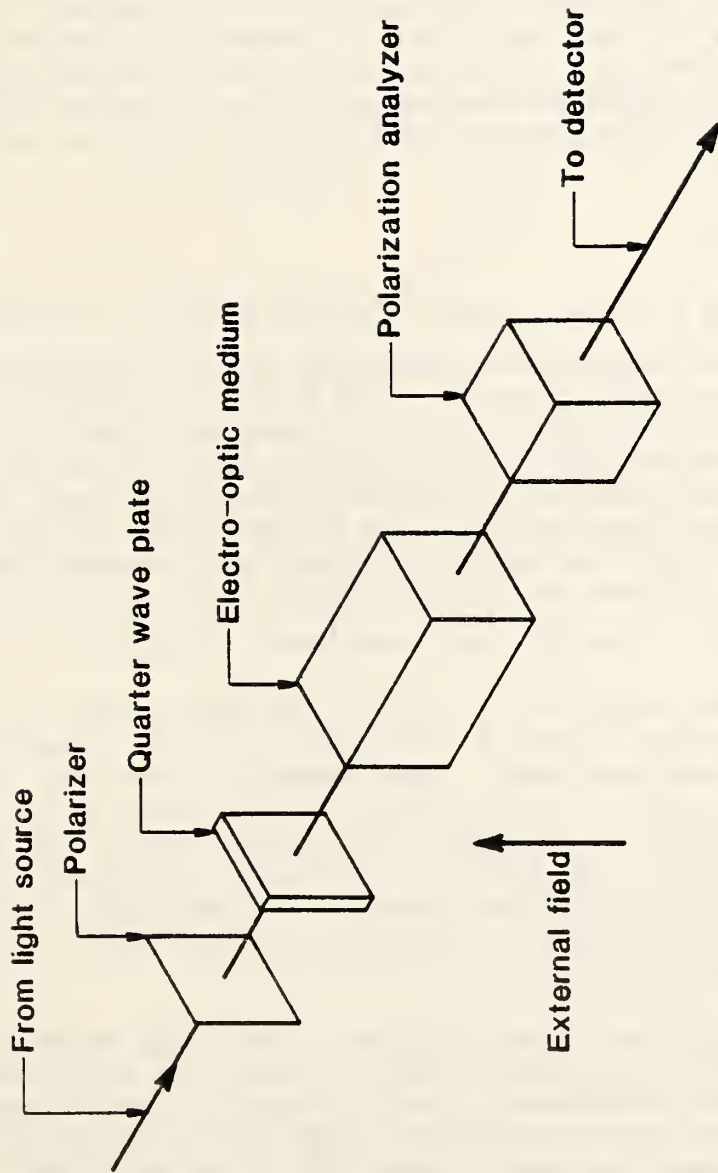


Figure 28. Schematic of system to measure electrical quantities using electro-optic sensors.

temperature), the electric field in the crystal. This is contrasted with the Kerr cell, where the phase depends on the square of the field in the medium. The intensity of the modulated light varies between one and zero, and so the amplitude range required of the signal processing is known for any signal. Clearly, what is recorded is not a direct replica of the electrical signal producing the electric field, but an intensity which must be demodulated numerically to obtain the actual waveform.

For appropriate configurations using the polarizers and quarter wave plate, the Pockels effect sensor can be used to provide a direct measurement of either steady state or transient phenomena, under the assumption that the phase shift is small. For this mode of operation, the quarter wave plate provides an "optical bias" so that the system is operating around the half-intensity point. A polarization analyzer at the output of the sensor may be used to produce independently the two components of the polarized light passing through the crystal, and a simple analysis shows that the two intensities can be written as

$$I_1/I_0 = 0.5(1 \pm \Gamma_m), \quad (68)$$

where $\Gamma_m = \pi E(t)/E_\pi$. Here E_π is the electric field required to produce 180° retardation between the two polarization components and is a function of crystal material, geometry, and orientation. If E varies sinusoidally, then signal processing may be done directly to yield a measure of the field, or if calibrated, the applied voltage [63]. The characteristics of the materials used in these Pockels effect sensors are such that measurements may be made of GHz signals [69]. Materials which appear to be of particular interest for electrical measurements include the potassium dihydrogen phosphate family, lithium niobate (LiNbO_3), lithium tantalate (LiTaO_3), bismuth germanate (BGO) and bismuth silicate (BSO), although others have been cataloged [70, 71].

A calculation was made using eq (67) and the waveform shown in figure 29 for a lithium tantalate crystal 1 mm x 1 mm x 10 mm, with the crossed polarizer configuration described above. The trapezoidal waveshape in figure 29 was maintained, but the amplitude was varied. The results for three different amplitudes are shown in figure 30, which show clearly the intensity variation predicted by eq (67). In practice, of course, the signals would be distorted by noise and would probably be a sampled, rather than a continuous record. The actual waveform would be recovered by fitting eq (67) to the data, with $E(t)$ as a parameter.

Although the approach appears promising for a wide range of measurements, there are problems to be solved. Thermal effects, long term stability, calibration, and mechanical resonances in the crystals are just representative examples. Clearly, a suitable choice of sensor material may minimize many of the effects which may corrupt the overall integrity of the measurement.

6.5 Streamer Growth in Dielectric Fluids under Fast Risetime Pulses

An existing test cell used in studies of dielectric liquids was modified and an outline of the cell is shown in figure 31 along with a small pulser used to characterize the water resistor divider which is used to measure the

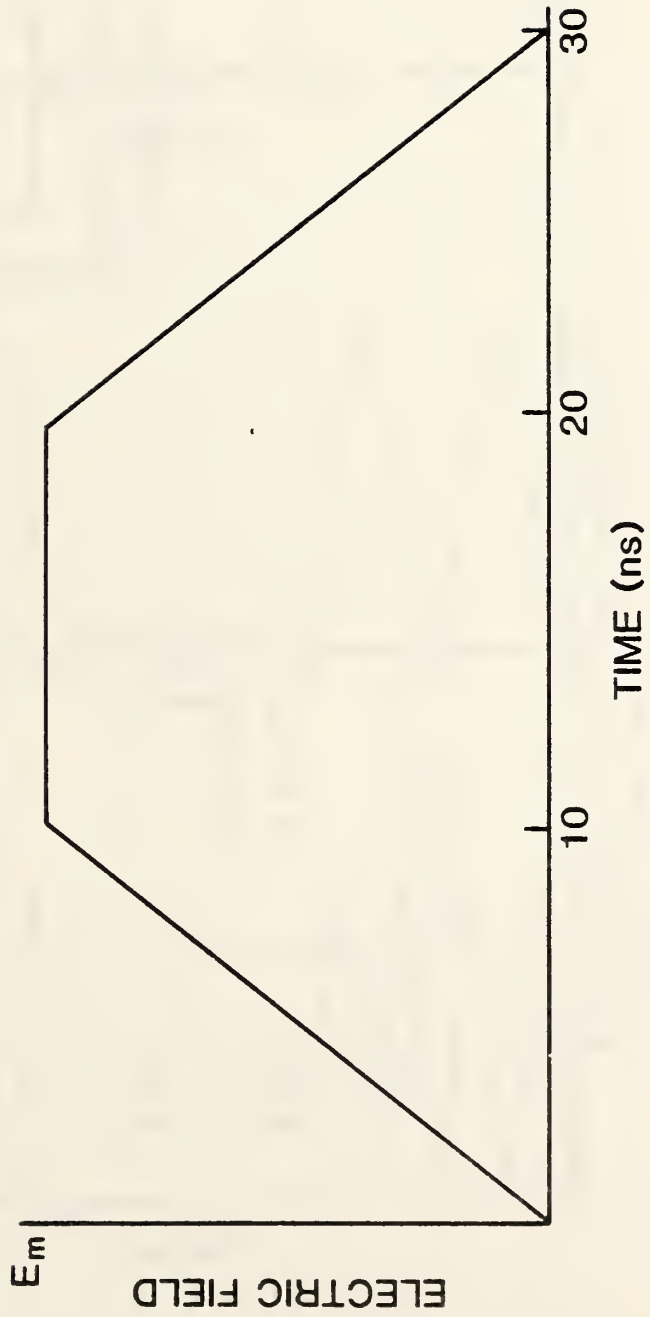
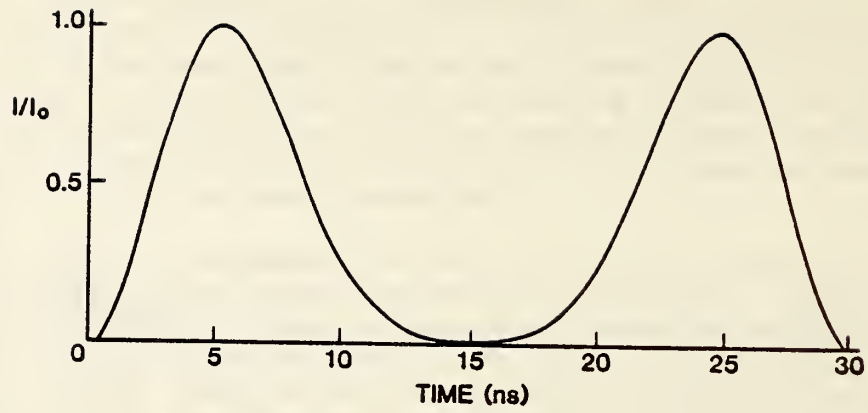
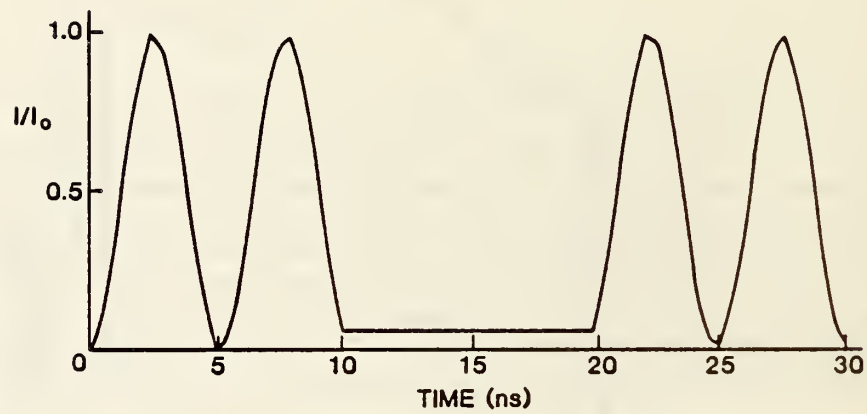


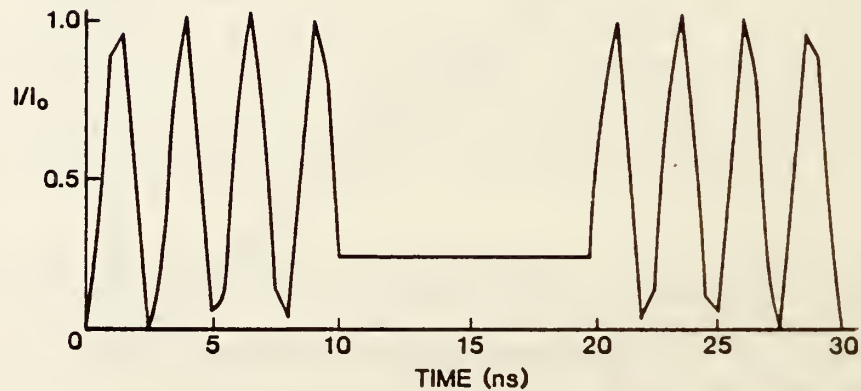
Figure 29. Trapezoidal waveform used in Pockels effect response calculation. For the calculations shown in figure 30, only the maximum electric field is changed.



a)



b)



c)

Figure 30. Normalized intensity of light for Pockels effect measurement described in text and for waveshape shown in figure 29. Raggedness in waveshape is due to coarseness of time grid used for calculations. a. $E_m = 0.5$ Mv/m. b. $E_m = 1$ Mv/m. c. $E_m = 2$ Mv/m.

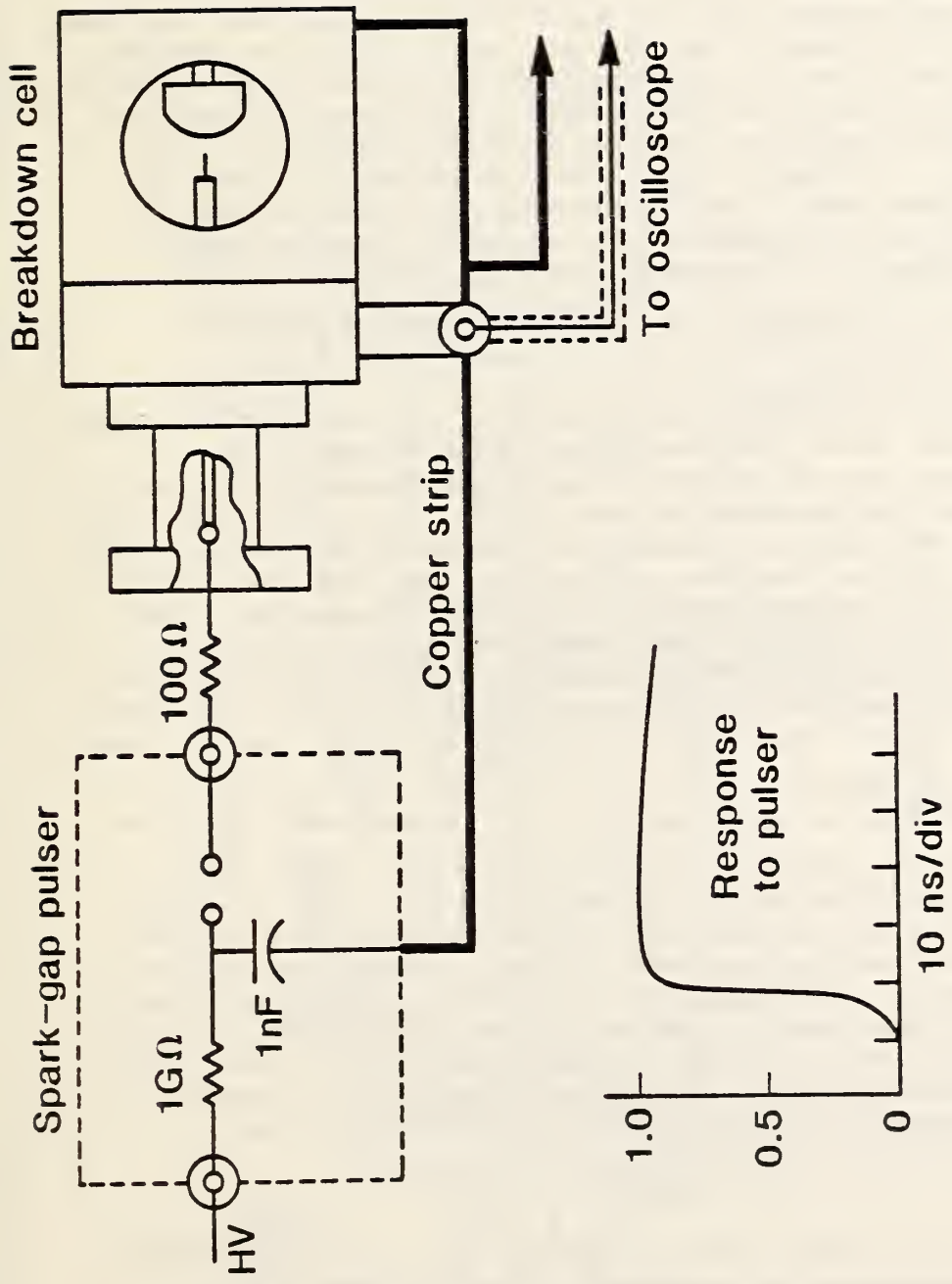


Figure 31. Configuration used to determine the response of the water resistor used to measure the voltage waveform applied to the gap. Response is shown schematically on the figure.

voltage applied to the cell. This pulser provides a step-like signal with a rise time under 10 ns. The response of the system, as configured, to the pulser output is shown on the figure, and is clearly less than 10 ns. There is some small droop in the voltage over the time scale indicated. A more detailed drawing of the entire assembly is given in Figure 32. The high voltage pulse enters on a flexible high voltage cable. A sharpening gap, gap 1, breaks down in oil and provides a fast rising voltage pulse to the test gap, gap 2. For the total assembly and the gap conditions used, the rise time of the pulse at the test cell was 50 ns. The gap, with point-plane geometry and a spacing of 2 mm, broke down in approximately 150 ns after application of the negative-going pulse. High speed photographs of the breakdown indicated an absence of the bush-like growth of ionization observed previously with microsecond pulses [72]. An example of the observed streamer is shown in figure 33. The images were taken from the photographic record and the time and exposure information is as indicated. The breakdown observed for the present waveform was mediated by a supersonic streamer with propagation speed estimated at 2×10^6 cm/s. By contrast, the bush-like structure grows at subsonic speeds.

During measurements taken with the modified cell, it became apparent that the method of charging the water capacitor using a high voltage pulse transformer was inadequate because of insufficient stored energy. Because of this, attempts to improve the operation of the modified cell were terminated, and a conventional cell was used with a commercial pulse generator capable of providing a nominal 100 μ s flat top pulse with a rise time less than 100 ns. The actual rise time was approximately 80 ns and output voltages were less than 300 kV. Examples of the framing camera exposures taken during these measurements are shown in figure 34. The geometry was a point plane geometry with a 1-cm gap, and the generator voltage was adjusted to provide different breakdown voltages. In figure 34a, breakdown occurred at 120 kV, and the speed of the streamer growth was approximately 7.1×10^4 cm/s. The time between exposures in this framing camera record was 500 ns. In contrast, the record shown in figure 34b shows a streamer with speed of 3.4×10^6 cm/s. Here the time between exposures was 50 ns and the exposure time is 10 ns. In neither case is there any evidence for the bush-like structures observed for slower rise pulses. It is clear that not only the risetime, but also the magnitude of the voltage is important. The interpretation of these results in terms of applied waveform has not been completed, but there are significant differences between these measurements and those made earlier using slower pulses. This suggests that the development of physical processes involved in breakdown may be different in nanosecond breakdown from that at slower time scales.

6.6 Summary

The development of the coaxial testline and the comparison of different sensors suitable for measurements of nanosecond pulses provides both a facility for evaluating measurement techniques and intercomparing different sensors, and a system for future studies of fast breakdown in gaseous dielectrics. Continued operation at low voltage measurements have indicated problems associated with certain capacitive sensors, and different designs will be used. Deconvolution methods offer both a method for characterizing individual sensors in a quantitative way and the opportunity for achieving

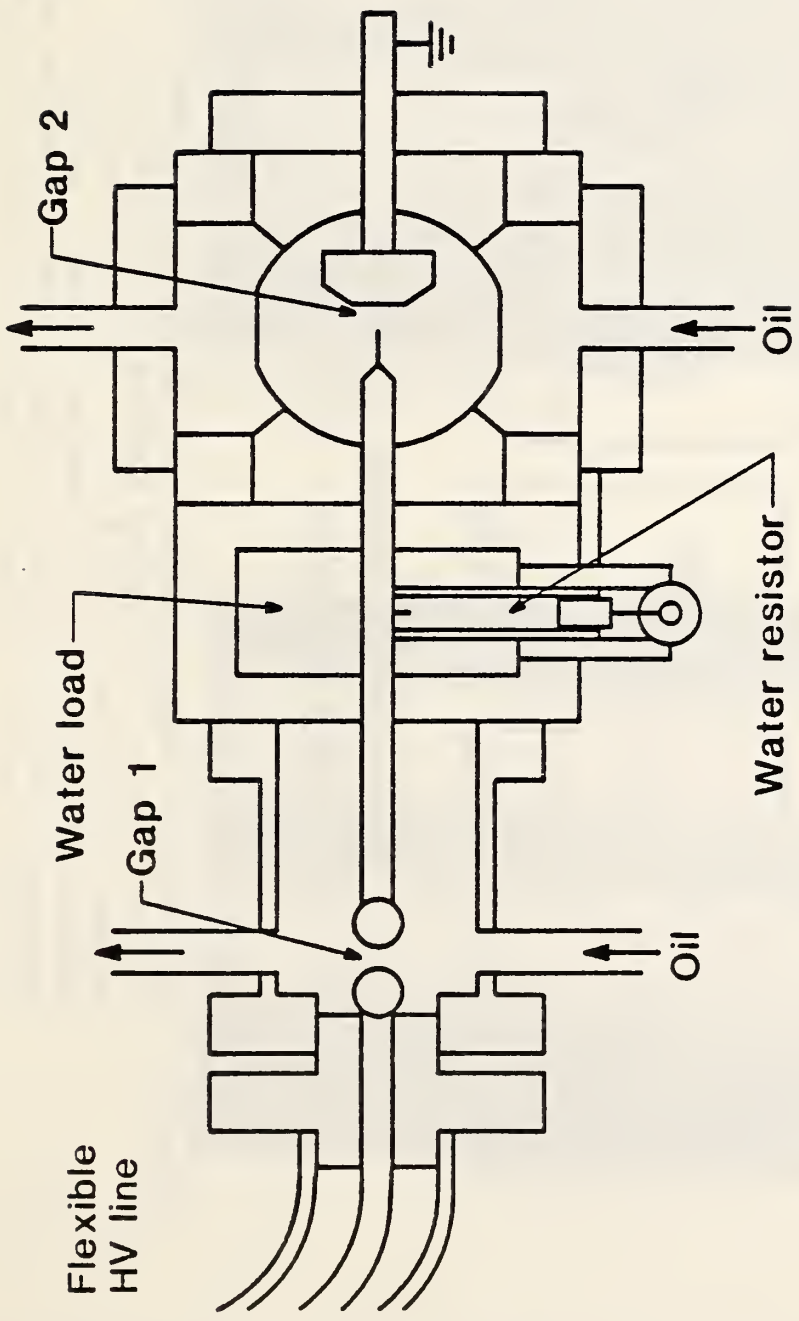
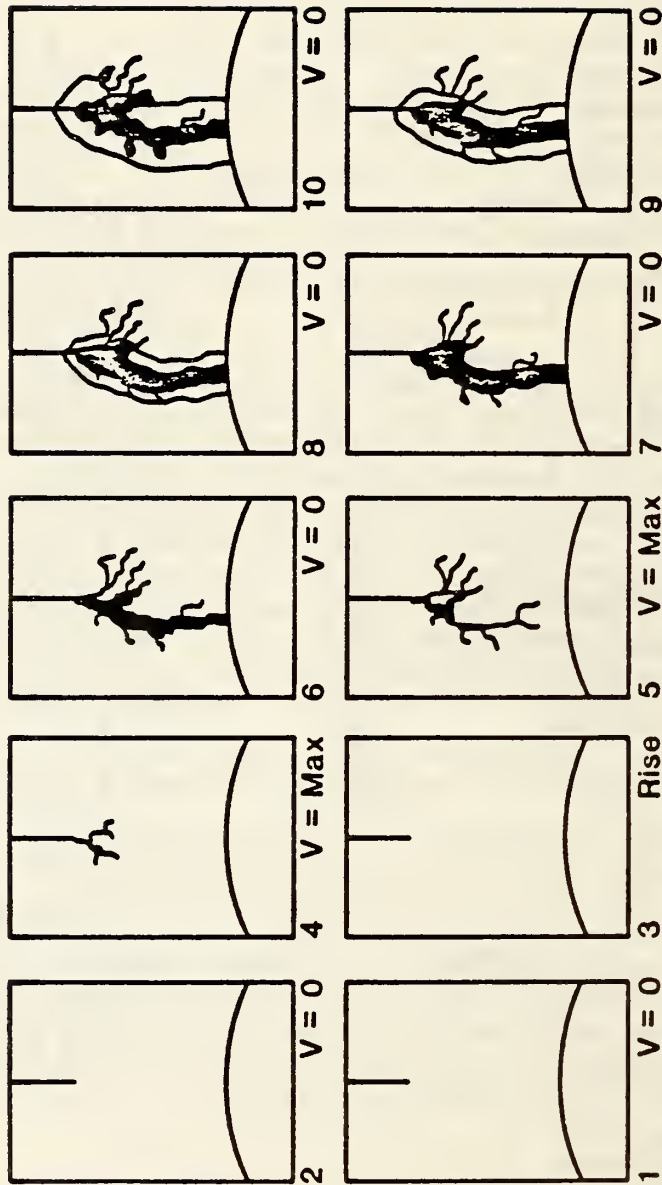


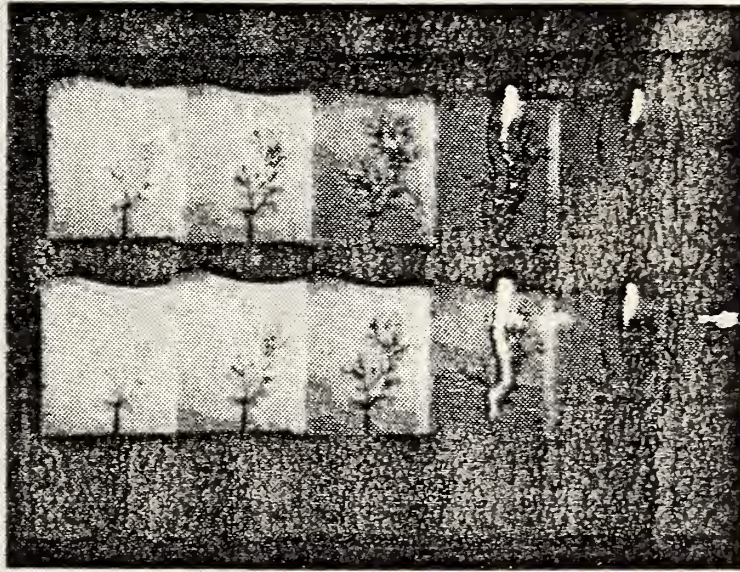
Figure 32. Cross sectional view of system used to study liquid dielectric breakdown processes under nanosecond pulse conditions. Construction details, such as types of materials, have been omitted for clarity. The flow of oil through the sharpening gap and the test region is indicated, as is the water capacitor used for pulse shaping.

Image Converter Photograph

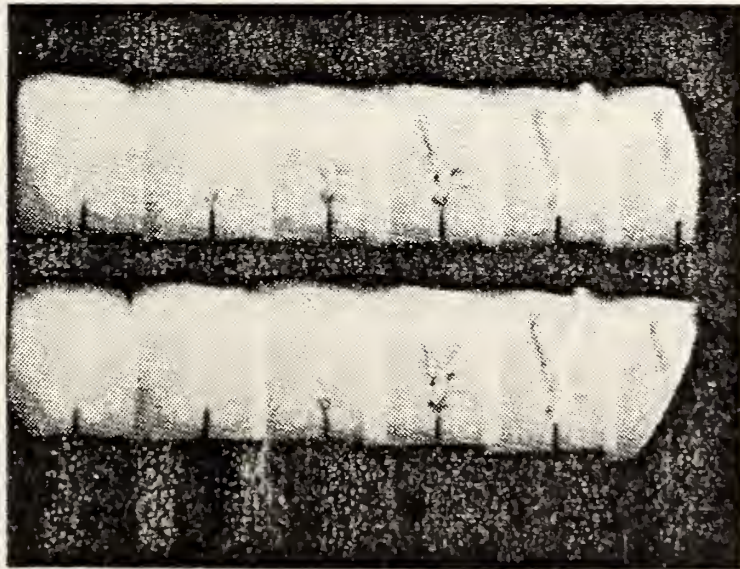


Time between frames: 50 ns
 Frame exposure: 10 ns

Figure 33. Representative images obtained from high speed photography of the breakdown process. The voltage waveform changes from zero to the maximum value between frames 2 and 4. The initiation of the supersonic streamer growth is observed in frame 4, and the breakdown process is complete in frame 6. There is no slow bush-like growth like that observed in studies using slower waveforms.



a)



b)

Figure 34. Comparisons of framing camera pictures of streamer growth in N-Hexane showing two different streamer speeds. a. Breakdown voltage of 120 kV, with time between exposures of 500 ns. Order of exposure is that shown in (fig. 33). b. Breakdown voltage of 240 kV, with 50 ns time between exposures. 7.05, 6.28 (± 0.4)

optimum measurement accuracy from a given sensor. The use of electro-optic measurement techniques for fast transients is being used extensively, and offers many advantages, including improved accuracy and electrical isolation. Initial measurements made using fast rise time pulses show differences in streamer growth in dielectric liquids.

7. REFERENCES

- [1] NBS Report NBSIR 83-2761, Development of Power System Measurements-- Quarterly Report, January 1 - March 31, 1983.
- [2] NBS Report NBSIR 84-2898, Development of Power System Measurements-- Quarterly Report, January 1 - March 31, 1984.
- [3] NBS Report NBSIR 85-3112, Development of Power System Measurements-- Quarterly Report, April 1 - June 30, 1984.
- [4] M. Misakian, Generation and measurement of dc electric fields with space charge, J. Appl. Phys., Vol. 52, pp. 3135-3143, 1981.
- [5] T.C. Fry, Two Problems In Potential Theory, Am. Math. Monthly, Vol. 39, pp. 199-209, 1932. The solution in this reference does not consider the influence of a connecting tube (ion counter) shown in figure 3. The presence of the tube can be expected to reduce the amount of field perturbation above the aperture.
- [6] It is interesting to note that the perturbation along the z-axis of an initially uniform electric field by a conducting spheroidal boss on the ground plane [see P. Moon and D.E. Spencer, Field Theory for Engineers (D. Van Nostrand, 1961), p. 287ff] is also twice that for the electric potential at large z. In the case of a conducting hemisphere, the relative perturbation is exactly two for all points along the z-axis greater than the radius.
- [7] G.W. Penny and R.E. Matick, Potentials in DC Corona Fields, Trans. AIEE, Comm. and Electr., Vol. 79, pp. 91-99, 1960.
- [8] R.E. Matick, Potentials in DC Corona Fields, Doctoral Dissertation, Carnegie-Mellon University, 1958.
- [9] During the space potential measurements it was necessary to increase J from $0.1 \times 10^{-6} \text{ A/m}^2$ to $0.25 \times 10^{-6} \text{ A/m}^2$ to obtain a more uniform current density profile. Therefore, the changes in ρ noted here differ from the results shown in figure 2.
- [10] A variable step-variable integration algorithm, PLOD, developed at NBS by D. Kahaner was used for the trajectory calculations. See also Guide To Available Mathematics Software, Report No. PB84-171305 (1984), available from NTIS, Springfield, VA 22151.
- [11] W.F.G. Swann, On Certain Matters Relating To The Theory of Atmospheric-Electric Measurements, Terr. Magnet. Atmos. Elect., Vol. 19, pp. 205-218, 1914.
- [12] Hara et al. have recently shown that the ion current to a cylindrical object in a dc electric field with ions and air stream is nearly independent of air speed. While fewer ion trajectories terminate on the cylinder at greater air speeds, the ion current to the cylinder remains nearly the same because of increased ion velocity. See M. Hara,

- M. Yashima, T. Tsutsumi, and M. Akazaki, Electrification current and voltage on a cylindrical object in the presence of an ion flow field in an air stream., IEE Proc., Vol. 132, Pt. A, pp. 59-66, 1985.
- [13] R. J. Van Brunt, "Water Vapor-Enhanced Electron Avalanche Growth in SF₆" (to be published J. Appl. Phys., 1986).
- [14] R. J. Van Brunt and D. A. Leep, "Characterization of Point-Plane Corona Pulses in SF₆," J. Appl. Phys., Vol. 52, pp. 6588-6600 (1981).
- [15] R. J. Van Brunt, "Production Rates for Oxyfluorides SOF₂, SO₂F₂, and SOF₄ in SF₆ Corona Discharges," J. Res. NBS, Vol. 90, pp. 229-253 (1985).
- [16] R. J. Van Brunt, "Effects of H₂O on the Behavior of SF₆ Corona," Proc. 7th Intl. Conf. on Gas Discharges and Their Applications, Peter Peregrinus, London, pp. 255-258 (1982).
- [17] R. J. Van Brunt and M. Misakian, "Mechanisms for Inception of DC and 60-Hz AC Corona in SF₆," IEEE Trans. Elec. Insul., Vol. EI-17, pp. 106-120 (1982).
- [18] R. J. Van Brunt, M. Misakian, D. A. Leep, E. C. Beaty, J. W. Gallagher, C. M. Cooke, K. Wyatt, and R. G. Gels, "1981 Annual Report: Technical Assistance for Future Insulation Systems Research," NBS Interagency Report 82-2555 (1982).
- [19] P. J. Chantry and R. E. Wootton, "A Critique of Methods for Calculating the Dielectric Strength of Gas Mixtures," J. Appl. Phys., Vol. 52, pp. 2731-2739 (1981).
- [20] R. L. Champion and L. D. Doverspike, "Electron Detachment Processes," in Electron-Molecule Interactions and Their Applications, Vol. 1, Ed. by L. G. Christophorou, Academic Press, pp. 619-681 (1984).
- [21] N. Wiegart, "A Model for Production of Initial Electrons by Detachment of SF₆⁻-Ions," IEEE Trans. Elec. Insul., Vol. EI-20, pp. 587-594 (1985).
- [22] O. J. Orient and A. Chutjain, "Comparison of Calculated and Experiment Thermal Attachment Rate Constants for SF₆ in the Temperature Range 200-600 K," (submitted to Phys. Rev. A, 1985).
- [23] W. Legler, "Statistics of Electron Avalanches," Zeit. fur Phys., Vol. 140, pp. 221-240 (1955); "The Statistics of Electron Avalanches in Electronegative Gases at High Field Strengths and for Large Gas-Amplification," Zeit. fur Naturforsh., Vol. 16A, pp. 253-261 (1961).
- [24] M. C. Siddagangappa, C. S. Lakshminarasimha, and M. S. Naidu, "Electron Attachment in Binary Mixtures of Electronegative and Buffer Gases," J.

- Phys. D, Vol, 15, pp. L83-86 (1982); "Electron Mean Energy, Secondary Ionization Coefficients and $(E/p)_{crit}$ in Binary Mixtures of SF_6-N_2 and $CCl_2F_2-N_2$," J. Phys. D, Vol. 16, pp. 1595-1601 (1983).
- [25] T. Aschwanden, "Discharge Parameters in Binary SF_6 Mixtures," Proc. 6th Intl. Conf. Gas Discharges and Their Applications, IEE Publ. No. 189, part 2, pp. 24-27 (1980); "Swarm Parameters in SF_6 and SF_6/N_2 -Mixtures Determined from a Time Resolved Discharge Study," Proc. 4th Intl. Symp. Gaseous Dielectrics, Gaseous Dielectris IV, Ed. by L. G. Christophorou, Pergamon Press, pp. 24-33 (1984).
- [26] M. S. Dincer and G. R. Govinda Raju, "Ionization and Attachment Coefficients in $SF_6 + N_2$ Mixtures," IEEE Trans. Elec. Insul., Vol. EI-19, pp. 40-44 (1984); "Measurement of Ionization and Attachment Coefficients in SF_6 and $SF_6 + N_2$," J. Appl. Phys., Vol. 53, pp. 8562-8567 (1982).
- [27] H. F. A. Verhaart, Thesis, Technische Hogeschool, Eindhoven, Netherlands (1982).
- [28] H. Itoh, M. Shimosuma, H. Tagashira, and S. Sakamoto, "Measurement of the Effective Ionization Coefficient and Static Breakdown Voltage in SF_6 and Nitrogen Mixtures," J. Phys. D, Vol. 12, pp. 2167-2172 (1979).
- [29] A. V. Phelps, NBS and Joint Institute for Laboratory Astrophysics, Boulder, Colorado (private communication).
- [30] L. E. Kline, D. K. Davies, C. L. Chen, and P. J. Chantry, "Dielectric Properties for SF_6 and SF_6 Mixtures Predicted from Basic Data," J. Appl. Phys., Vol. 50, pp. 6789-6796 (1979).
- [31] J. P. Novak and M. F. Frechette, "Transport Coefficients of SF_6-N_2 Mixtures from Revised Data," J. Appl. Phys., Vol. 55, pp. 107-119 (1984).
- [32] H. Itoh, M. Shimosuma, and H. Tagashira, "Boltzmann Equation Analysis of the Electron Swarm Development in SF_6 and Nitrogen Mixtures," J. Phys. D, Vol. B, pp. 1201-1209 (1980).
- [33] M. S. Dincer and G. R. Grovinda Raju, "Monte Carlo Simulation of the Motion of Electrons in SF_6 in Uniform Electric Fields," J. Appl. Phys., Vol. 54, pp. 6311-6316 (1983).
- [34] N. H. Malik and A. H. Qureshi, "Breakdown Gradients in SF_6-N_2 , SF_6 -Air, and SF_6-CO_2 Mixtures," IEEE Trans. Elec. Insul., Vol. EI-15, pp. 413-418 (1980).

- [35] J. P. Novak and M. F. Frechette, "Collisional Cross Sections of CCl_2F_2 and Transport Coefficients of CCl_2F_2 and $\text{N}_2\text{-CCl}_2\text{F}_2$ Mixtures," J. Appl. Phys., Vol. 57, pp. 4368-4376 (1985), and references contained there in.
- [36] S. R. Hunter and L. G. Christophorou, "Pressure-Dependent Electron Attachment and Breakdown Strengths of Unary Gases and Synergism of Binary Gas Mixtures: A Relationship," J. Appl. Phys. 57, pp. 4377-4385 (1985).
- [37] M. C. Siddagangappa and R. J. Van Brunt, "Decomposition Products from Corona in SF_6/N_2 and SF_6/O_2 Mixtures," Proc. 8th Intl. Conf. Gas Discharges and Their Applications, Leeds University Press, London, pp. 247-250 (1985).
- [38] A. V. Phelps and L. C. Pitchford, "Anisotropic Scattering of Electrons by N_2 and its Effect on Electron Transport," Phys. Rev. A, Vol. 31, pp. 2932-2949 (1985), and references contained there in.
- [39] L. Niemeyer, "A Model of SF_6 Leader Channel Development," Proc. 8th Intl. Conf. Gas Discharges and Their Applications, Leeds University Press, London, pp. 223-226 (1985).
- [40] R. F. Heidner, D. G. Sutton, and S. N. Suchard, "Kinetic Study of $\text{N}_2(\text{B}^3\Pi_g, v)$ Quenching by Laser-Induced Fluorescence," Chem. Phys. Lett., Vol. 37, pp. 243-248 (1976).
- [41] I. Sauers, Proc. 1985 IEEE Pulse Power Conference, Washington, DC (in press).
- [42] E. F. Kelley and R. E. Hebner, "Electrical Breakdown in Composite Insulating Systems: Liquid-Solid Interface Parallel to the Field," IEEE Trans. Elec. Insul., Vol. EI-16, No. 4, August 1981, pp. 297-303.
- [43] E. F. Kelley and R. E. Hebner, "On the Ineffectuality of an Oil-Paper Interface," to be published. This paper verifies the above work and extends its results to higher temperatures. The conclusions all remain the same: A clean paper interface parallel to the field and touching both electrodes does not necessarily cause interfacial breakdown or even lower the breakdown voltage.
- [44] E. F. Kelley and R. E. Hebner, "Measurement of the Electric Field in the Vicinity of an Oil-Pressboard Interface Parallel to the Field," IEEE Trans. Elec. Insul., Vol. EI-19, No. 6, Dec. 1984, pp. 519-523.
- [45] E. F. Kelley and R. E. Hebner, "Electro-Optic Electric-Field Measurements Near Oil-Pressboard Interfaces," Conference Record of 1984 IEEE International Symposium on Electrical Insulation, Montreal, June 11-13, 1984, pp. 311-314.

- [46] E. C. Cassidy, R. E. Hebner, Jr., M. Zahn, and R. J. Sojka, "Kerr-Effect Studies of an Insulating Liquid Under Varied High-Voltage Conditions," IEEE Trans on Elect. Insul., Vol. EI-9, No. 2, pp. 43-56, June 1974.
- [47] M. Zahn, et al., "Effects of Electrode Material on Charge Injection, Transport, Energy Storage and Dissipation in Highly Purified Water," Conference Record of 1984 IEEE International Symposium on Electrical Insulation, Montreal, Canada, pp. 304-310, June 11-13, 1984.
- [48] S. J. Rzad, J. C. Devins and R. J. Schwabe, "The Influence of a dc Bias on Streamers Produced by Step Voltages in Transformer Oil and Over Solid-Liquid Interfaces," IEEE Trans. Elec. Insul. Vol EI-18, No. 1, pp. 1-10, Feb. 1983.
- [49] R. H. McKnight and H. K. Schoenwetter, "Evaluation of Transient Measurement Methods in Gas-Insulated Transmission Lines," NBSIR 83-2753, 75 pages (August 1983).
- [50] T. M. Souders, D. R. Flach, H. K. Schoenwetter, "Transient Response Characterization of Waveform Recorders," Proceedings of the 5th IEEE Pulsed Power Conference, June 10-12, 1985, (in press).
- [51] R. E. Hebner, "Development of Power System Measurements"--Quarterly Report, January 1, 1984 to March 31, 1984, Nat. Bur. Stand. (U.S.), NBSIR 84-2898, 28 pages (July 1984).
- [52] A. V. Oppenheim and A. S. Willsky, Signals and Systems. Prentice-Hall, 1983.
- [53] R. H. McKnight, C. Fenimore, and J. Lagnese, "The Use of Deconvolution Methods in Characterizing Electrical Sensors," Proc. of IEEE Pulsed Power Conf., June 10-18, 1985 (in press).
- [54] N. S. Nahman and M. E. Guillaume, "Deconvolution of Time Domain Waveforms in the Presence of Noise," NBS Technical Note 1047, October 1981.
- [55] See Ref. 52, p345ff.
- [56] H. F. Silverman and A. E. Pearson, "On Deconvolution Using the Discrete Fourier Transform," IEEE Trans. on Audio and Electroacoustics, vol. AU-21, no. 2, April 1973.
- [57] R. E. Hebner, E. C. Cassidy, and J. E. Jones, "Improved Techniques for the Measurement of High-Voltage Impulses Using the Electrooptic Kerr Effect," IEEE Trans. Instrum. Meas. IM-24, No. 4, pp. 361-366 (Dec. 1975).
- [58] E. F. Kelley and R. E. Hebner, "The Electric Field Distribution Associated with Prebreakdown Phenomena in Nitrobenzene," J. Appl. Phys. 52, No. 1, pp. 191-195 (Jan. 1981).

- [59] E. F. Kelley and R. E. Hebner, "Electro-Optic Measurement of the Electric Field Distribution in Transformer Oil," IEEE Trans. Power Appar. Syst. PAS-102, No. 7, pp. 2092-2097 (July 1983).
- [60] T. G. Giallorenzi, J. A. Bucaro, A. Dandridge, G. H. Sigel, Jr., J. H. Cole, S. C. Rashleigh and R. G. Priest, "Optical Fiber Sensor Technology", IEEE J. Quantum Electron., QE-18, pp. 626-665, (1982).
- [61] V. I. Busirin, A. S. Semenov, and N. P. Udalov, "Optic and Fiber Optic Sensors (Review)", Sov. J. Quantum Electronics, 15, pp. 595-621, (1985).
- [62] B. E. Jones, "Optical Fibre Sensors and Systems for Industry", J. Phys. E.: Sci. Instr. 18, pp. 770-782, (1985).
- [63] M. Kanoi, G. Takahashi, T. Sato, M. Higakai, E. Mori, and K. Okumura, "Optical Voltage and Current Measuring System for Electric Power Systems", presented at the 1985 summer meeting of the IEEE Power Engineering Society, Vancouver, B.C. (1985).
- [64] H. M. Hertz, "Capacitively Coupled KD*P Pockels Cell for High Voltage Pulse Measurements", J. Phys. E: Sci. Instrum., 18, pp. 522-525, (1985).
- [65] H. Trinks, G. Matz and H. Schilling, "Electro-Optical System for EMP Measurement", IEEE Trans. Electromagn. Compat., EMC-22, pp. 75-77, (1980).
- [66] M. Hanazaki and Y. Yosojimi, "Measurement of Surface Charges on the Barrier and their Effect on the Oil Gap Breakdown", 1985 Annual Report, Conference on Electrical Insulation and Dielectric Phenomena, pp. 50-57, (1985).
- [67] J. Chang, W. F. Filter, G. J. Lockwood, and B. T. Neyer, "Photonic Methods of High-Speed Data Recording", Rev. Sci. Instrum., 56, pp. 1861-1866, (1985).
- [68] R. E. Hebner, "Electro-Optical Measurement Techniques", Proc. NATO Advanced Study Institute: Fast Electrical and Optical Diagnostic Principles and Techniques, Castelvechio, Italy, in press.
- [69] J. Chang, C. N. Vittitoe, B. T. Neyer and W. P. Ballard, "An Electro-Optical Technique for Intense Microwave Measurements", J. Appl. Phys., 57, pp. 4843-4848, (1985).
- [70] I. P. Kaminow and E. H. Turner, "Linear Electrooptical Materials", in "Handbook of Lasers" (R. J. Pressley, ed.), pp. 447-459, Chemical Rubber Co., Cleveland, Ohio, (1971).
- [71] J. T. Milek and M. Neuberger, "Linear Electrooptic Modular(sic) Materials", Handbook of Electronic Materials, Vol. 8, IFI/Plenum, New York, (1972).
- [72] R. E. Hebner, E. F. Kelley, E. O. Forster, and G. J. FitzPatrick, "Observations of Prebreakdown and Breakdown Phenomena in Liquid Hydrocarbons II. Point-Place Geometry, 1981 Annual Report," Conference on Electrical Insulation and Dielectric Phenomena, pp. 377-389 (Oct. 1981).

U.S. DEPT. OF COMM. BIBLIOGRAPHIC DATA SHEET (See instructions)		1. PUBLICATION OR REPORT NO. NBSIR 86-3316	2. Performing Organ. Report No. 722.01	3. Publication Date March 1986
4. TITLE AND SUBTITLE Research for Electric Energy Systems -- An Annual Report				
5. AUTHOR(S) R. E. Hebner				
6. PERFORMING ORGANIZATION (If joint or other than NBS, see instructions) NATIONAL BUREAU OF STANDARDS DEPARTMENT OF COMMERCE WASHINGTON, D.C. 20234			7. Contract/Grant No.	8. Type of Report & Period Covered Annual January 1, 1985 to December 31, 1985
9. SPONSORING ORGANIZATION NAME AND COMPLETE ADDRESS (Street, City, State, ZIP) Department of Energy Division of Electric Energy Systems 1000 Independence Avenue, S. W. Washington, D.C. 20585				
10. SUPPLEMENTARY NOTES <input type="checkbox"/> Document describes a computer program; SF-185, FIPS Software Summary, is attached.				
11. ABSTRACT (A 200-word or less factual summary of most significant information. If document includes a significant bibliography or literature survey, mention it here) This report documents the technical progress in the five investigations which make up the project "Support of Research Projects for Electrical Energy Systems," Department of Energy Task Order Number 137, funded by the U.S. Department of Energy's Office of Energy Systems Research and performed in the Electrosystems Division of the U.S. National Bureau of Standards.				
12. KEY WORDS (Six to twelve entries; alphabetical order; capitalize only proper names; and separate key words by semicolons) breakdown; corona; deconvolution; electric field; electro-optics; magnetic fields; SF ₆ ; space charge; transformer oil				
13. AVAILABILITY <input checked="" type="checkbox"/> Unlimited <input type="checkbox"/> For Official Distribution. Do Not Release to NTIS <input type="checkbox"/> Order From Superintendent of Documents, U.S. Government Printing Office, Washington, D.C. 20402. <input checked="" type="checkbox"/> Order From National Technical Information Service (NTIS), Springfield, VA. 22161			14. NO. OF PRINTED PAGES 87	
			15. Price \$11.95	

